UNIVERSITY OF CALIFORNIA, SAN DIEGO

Climate effects of black carbon
and the emission reduction for mitigating climate change

A dissertation submitted in partial satisfaction of the requirements for
the degree Doctor of Philosophy

in

Earth Sciences

by

Yangyang Xu

Committee in charge:

Veerabhadran Ramanathan, Chair
Lynn Russell
Lynne Talley
David Victor
Warren Washington
Guang Zhang

2014

The dissertation of Yangyang Xu is approved, and it is acceptable in quality and form for publication on micro-film and electronically:

_____

_____

_____

_____

_____

_____

Chair

University of California, San Diego

2014

DEDICATION

To

My family

TABLE OF CONTENTS

LIST OF ABBREVIATIONS

AAE	Absorption Angstrom Exponent
AAOD	Absorption Aerosol Optical Depth
AERONET	Aerosol Robotic Network
AOD	Aerosol Optical Depth
AR5	The 5th Assessment Report
ARM	Atmospheric Radiation Measurement
Atm	Atmospheric
BAU	Business As Usual
BC	Black Carbon
CAM	Community Atmospheric Model
CESM	Community Earth System Model
CH4	Methane
CLM	Community Land Model
CMIP5	Coupled Model Intercomparison Project Phase 5
CO	Carbon monoxide
CO_2	Carbon dioxide
DOE	Department of Energy
EC	Element Carbon
ECHAM5	The 5th generation of the ECHAM general circulation model

EPA	Environmental Protection Agency
GCM	Global Climate Model
GDP	Gross Domestic Product
GFDL	Geophysical Fluid Dynamics Laboratory
GHG	Greenhouse gases
GISS	Goddard Institute for Space Studies
GOCART	Goddard Chemistry Aerosol Radiation and Transport model
GPCP	Global Precipitation Climatology Project
GWP	Global Warming Potential
HFC	Hydrofluorocarbons
HIPPO	HIAPER Pole-to-Pole Observations
IGP	Indo-Gangetic Plains
INDOEX	The Indian Ocean Experiment
IPCC	Intergovernmental Panel on Climate Change
K	Kelvin
LPG	Liquefied Petroleum Gas
LW	Longwave
MACR	Monte Carlo Aerosol Cloud Radiation model
MAM	Modual aerosol Model
MISR	Multi-angle Imaging SpectroRadiometer
MODIS	Moderate Resolution Imaging Spectroradiometer
MPI	Max Planck Institutes

NASA	National Aeronautics and Space Administration
NCAR	National Center for Atmospheric Research
NGO	Non-governmental organizations
NH	Northern Hemisphere
OC	Organic carbons
OHC	Ocean heat content
OPAC	Optical Properties of Aerosols and Clouds
PM2.5	Particulate Matter up to 2.5 micrometers in size
PNNL	Pacific Northwest National Laboratory
RCP	Representative Concentration Pathway
RIVM	National Institute for Public Health and the Environment (Netherland)
RRTMG	Rapid Radiative Transfer Model for Gases
Sfc	Surface
SH	Southern Hemisphere
SIO	Scripps Institution of Oceanography
SLCP	Short-lived climate pollutants
SLR	Sea level rise
SNICAR	SNow, ICe, and Aerosol Radiative model
SOA	Secondary Organic Aerosol
SO_2	Sulfur dioxide
SO_4	Sulfate

SSA	Single scattering albedo
SST	Sea surface temperature
SW	Shortwave
TOA	Top of Atmosphere
TS	Temperature at the Surface
UCSB	University of California, Santa Barbara
UNEP	United Nations Environment Programme
UQ	Uncertainty quantifications
US	United States
USD	US Dollar
WRF	Weather Research and Forecasting Model
W/m^2	Watts per square meters

LIST OF FIGURES

LIST OF TABLES

ACKNOWLEDGEMENTS

First and foremost, I would like to thank my academic advisor Professor Ramanathan, who in the five years guided my research with great patience and continuously motivated me to be more creative and independent in research. I've always been enjoying working with Ram. I learnt so much as a student by taking his advice and observing how he does research. I am more determined to pursue a scientific career after working with Ram.

I would like to acknowledge Dr Warren Washington for hosting me at National Center for Atmospheric Research during the last year of my graduate school. Most part of this dissertation is done by collaboration with Dr Washington, who provided me great advice on climate modeling and thesis writing. I especially thank him for his warm encouragements on my research.

I also acknowledge my doctoral committee members. I started my first quarter of graduate study by working at Prof. Russell's group, and I received much training back then, and more later in several classes she taught related to aerosols and atmospheric chemistry. I benefited greatly with discussions and personal interactions with Dr Guang J. Zhang. I took various classes taught by Prof Lynne Tally and Prof David Victor, and I thank them for their valuable advice and support on various stages of my Ph.D. study.

Great thanks to my colleagues in Scripps C4 group for their wonderful support: Muvva Ramana, Hung Nguyen, Eddy Chung, Martin Olivera, Dohyeong Kim, Yan Feng, Ranjit Bahadur, PS Praveen, Kristina Pistone, Liliana Nunez, Jen Burney.

I also want to thank staffs in SIO department for their help and support: Joshua Reeves, Kharyn Loteyro, Becky Burrola, Gilbert Bretado, Wilson Rivera, Sylvia Robbins, Gayle Aruta.

I am grateful to many external collaborators on various other projects not included in this dissertation: Drs. Ruby Leung and Chun Zhao (Pacific Northwest National Lab), Durwood Zaelke (UCSB) and Guus Velders (Netherland/RIVM). During my visit at National Center for Atmospheric Research, I enjoyed very much being part of the Climate Change Predication group. I want to thank the group members: Jerry Meehl, Aixue Hu, Claudia Tebaldi, Haiyan Teng, Ben Sanderson, Alex Jonko, Garry Strand, Susan Bates; and also many other NCAR scientists who helped my research: J-F Lamarque, Bryan Eaton, and Jeff Kiehl.

I would like to acknowledge my fellow students and friends in the SIO department: Dian Putrasahan, Anais Orsi, Shang Liu, Gabe Cooperman, Linghan Li, Xiaopeng Tong, Xiaowei Chen and many. I am deeply grateful to my family for all their support, my parents for their love. Lastly and most importantly, I thank my wife Xiaoshan Gao with all my heart. I could have done none of this without her.

I acknowledge National Science Foundation for their funding support for my research. The text of Chapter 3, in full except Section 3.1.1 and Figure 3.1, is a reprint of a published paper entitled “Latitudinally asymmetric response of global surface temperature: Implications for regional climate change” in July 2012 issue of Geophysical Research Letters. The dissertation author was the primary researcher and author of this paper. Co-author on this paper is V. Ramanathan.

VITA

2008 B. S. in Atmospheric Sciences, Peking University, Beijing

2011 M. S. in Oceanography, Scripps Institution of Oceanography, University of California, San Diego

2014 Ph. D. in Earth Sciences, Scripps Institution of Oceanography, University of California, San Diego

PUBLICATIONS

Xu, Y., R. Bahadur, C. Zhao, and L. Ruby Leung (2013), Estimating the radiative forcing of carbonaceous aerosols over California based on satellite and ground observations, Journal of Geophysical Research: Atmospheres, 2013JD020654.

Hu, A., Y. Xu, C. Tebaldi, W. M. Washington, and V. Ramanathan (2013), Mitigation of short-lived climate pollutants slows sea-level rise, Nature Climate Change, 3(5), 15, doi:10.1038/nclimate1869.

Xu, Y., D. Zaelke, G. J. M. Velders, and V. Ramanathan (2013), The role of HFCs in mitigating 21st century climate change, Atmospheric Chemistry and Physics, 13(12), 60836089, doi:10.5194/acp-13-6083-2013.

Bahadur, R., P. S. Praveen, Y. Xu, and V. Ramanathan (2012), Solar absorption by elemental and brown carbon determined from spectral observations, Proceedings of the National Academy of Sciences of the United States of America, 109(43), 1736671, doi:10.1073/pnas.1205910109.

Xu, Y., and V. Ramanathan (2012), Latitudinally asymmetric response of global surface temperature: Implications for regional climate change, Geophysical Research Letters, 39, L13706, doi:10.1029/2012GL052116.

Ramanathan, V., and Y. Xu (2010), The Copenhagen Accord for limiting global warming: criteria, constraints, and available avenues, Proceedings of the National Academy of Sciences of the United States of America, 107(18), 805562, doi:10.1073/pnas.1002293107.

Xu, Y., S. Liu, F. Hu, N. Ma, Y. Wang, Y. Shi, and H. Jia (2009), Influence of Beijing urbanization on the characteristics of atmospheric boundary layer, Chinese Journal of Atmospheric Sciences, 33(4), 859867.

FIELDS OF STUDY

Major Field: Climate sciences

ABSTRACT OF THE DISSERTATION

Climate effects of black carbon

and the emission reduction for mitigating climate change

by

Yangyang Xu

Doctor of Philosophy in Earth Sciences

University of California, San Diego, 2014

Professor Veerabhadran Ramanathan, Chair

Black carbon (BC) aerosols are significant contributors to anthropogenic climate change and are considered as the second largest warming agent only after CO_2. To better quantify the present-day Asian BC aerosol forcing, in Chapter 2 we utilize both a top-down approach using ground-based and satellite observations, as well as a bottom-up

approach using a latest global climate model. By comparing the observations with the model simulations, we show that the emission inventory over Asia used in the model needs to be adjusted by a factor of two to four. The global mean BC forcing since pre-industrial in the model is 0.5 to 0.8 W/m^2, larger than the unconstrained model forcing of 0.2 W/m^2.

In understanding the climate system response to external forcing such as BC, we first show in Chapter 3 that the north-south contrast of land and ocean distribution determines the latitudinal asymmetry of climate change, which is an intrinsic characteristic of the climate system. The main thrust of this dissertation is that in Chapter 4, we demonstrate with the improved CESM that that BC aerosols play a vital role in causing the observed surface warming, snow cover and snow depth reduction over Tibet and Himalaya region. Due to BC aerosols, the simulated snow cover fraction over Tibet is reduced by more than 2% and snow depth is reduced by 5%. The model simulated warming enhancement at high altitude surface (more than 1 K at 5000 m) due to the direct atmospheric heating of BC and the BC deposition on the snow surface are similar to observations. The relative contributions from greenhouse gases and cooling aerosols are also assessed with the model.

In Chapter 5, we evaluate the climate mitigation benefits associated with a rapid reduction of BC aerosols. We show that aggressive BC reduction leads to warming mitigation and snow recovery over Tibet. We further discussed the major sources of BC emissions from China and the potential practical measures to cut BC emissions. The costs and benefits on public health due to cook-stove improvement are also discussed.

Chapter 1

Introduction

1.1 Black carbon aerosols

Black carbon aerosols are directly emitted from the incomplete combustion of fossil fuels and biomass burning. Fossil fuels (diesel and solid coal burning) contribute about 38% of global BC emissions (8.0 Tg per year); cooking and heating with biofuels (firewood, dung, crop residues) contributes about 20% and the remaining 42% is attributed to open biomass burning. All of these numbers are uncertain by at least a factor of two (Bond et al., 2004).

The particular focus in this study is on carbonaceous aerosols (BC and organic carbon) from India and China, since they emit more than 50% of the global anthropogenic black carbon (BC) and organic carbon (OC). The estimated energy-related emissions of BC over East Asia have increased six fold since the 1950s (Bond et al., 2007), and are likely responsible for many observed climate change phenomena during this period. In addition, BC has emerged as a major contributor to regional climate changes in India and China.

Black carbon (BC) and other light absorbing aerosols such as organic carbon and dust can absorb the incoming solar radiation, therefore heating the planet and perturbing the atmospheric temperature structure. Recent studies suggest that the radiative forcing of BC (0.5 to 1 W/m^2) is significant possibly only less than CO_2 (1.8 W/m^2) when compared with all other climate warming agents (Ramanathan and Carmichael, 2008; Jacobson,

2010).

The climate warming effects of BC from fossil fuels (e.g. diesel combustions) are reasonably well understood and hence reduction of BC from diesel has been recommended (e.g. Jacobson, 2009) to mitigate climate change. However, the climate warming effects of BC from residential cooking and heating using biomass fuels (India) and solid coal (China) contain significant uncertainties. In both China and India, residential cooking and heating are the primary source of BC emissions (Figure 1.2). For example, in India biomass-fuel burning accounts for up to two thirds of BC (Venkatraman et al., 2005). Roughly three billion rural inhabitants are forced to burn bio-fuels for cooking, lighting, home heating, and small industry due to economic conditions. Thus, drastic reductions in BC biofuel emissions have the potential of significantly slowing down regional climate changes.

However, BC is concentrated in regions close to its sources and its non-uniform forcing pattern will lead to a more complicated response pattern, which is not well understood. Untangling the coupled ocean-atmosphere impacts of BC from those of greenhouse gases is a major challenge in making decadal projections for regional climates. The first step requires a better quantification of BC's radiative forcing.

1.2 BC's radiative forcing

1.2.1 Previous studies

Radiative forcing is a measure of how the energy balance of the Earth-Atmosphere system is changed when factors that affect climate are altered. It is defined as the net irradiance change at the tropopause resulting from an applied perturbation, after

allowing stratospheric temperatures to readjust to radiative equilibrium while holding all other atmospheric variables fixed. Since aerosols can scatter and absorb solar and terrestrial radiation, they directly modulate the way radiation is transmitted through the atmosphere, which leads to radiative forcing.

BC has a strong absorption of light and therefore heats the atmosphere. In addition to the direct heating caused by the absorption of BC, the heating induced by the absorbing aerosols changes the relative humidity and stability of the troposphere and in turn modifies the cloud amount, thickness, and lifetime (Ackerman et al., 2000; Johnson et al., 2004). Moreover, the deposition of dark aerosols such as BC on snow/ice greatly darkens the surface and aggravates the retreat of glaciers and the melting of sea ice by changing the surface albedo (e.g. Hansen and Nazarenko, 2004; Flanner et al., 2007).

BC absorbs strongly at all wavelengths of the solar spectrum and therefore exerts positive radiative forcing. The mean direct radiative forcing of the fossil fuel and biofuel related BC is 0.4 [0.05 to 0.8] W/m^2 according to the IPCC AR5, mostly based on chemistry and climate modeling. Major modeling efforts have been initiated to accurately estimate the radiative effects of atmospheric aerosols. Observational efforts have also been mounted to aid modeling studies. In addition, by constraining models with observations, the aerosol indirect forcing and semi-direct forcing (Ramanathan et al., 2001a) have been derived.

BC is also co-emitted with other species, including organic carbons (OC). Generated from fossil fuels, biofuels and biomass combustion are usually a complex mixture of chemical compounds containing organic or elemental carbon species. Characteristic organic functional group includes fuel combustion, vegetation, and ocean

bubble bursting sources, and some of which is secondary organic aerosols (SOA) from gas precursors (Russell et al., 2011).

Organic carbons have relatively different optical properties. OC aerosols are predominantly scattering; however, some OC from fossil fuel combustion absorbs weakly in the ultraviolet and shorter wavelength ranges of the visible spectrum (Bond et al., 2001), and OC generated from less efficient combustion processes such as biomass burning has even greater absorption properties (Kirchstetter et al., 2004).

Chung et al. (2005) merged the models and observed fields of aerosol parameters using assimilation methods, and estimated the direct forcing by anthropogenic aerosols using AERONET (AErosol RObotic NETwork), satellite and model analysis. Their results show that the global annual mean direct radiative forcing by anthropogenic aerosols (including black carbon and other cooling aerosols) is -0.35 W/m^2 at the TOA and -3.4 W/m^2 at the surface, with an overall uncertainty range of -0.1 to -0.6 W/m^2.

Due to its highly inhomogeneous distribution and complicated mixing state with other aerosols, the radiative forcing of BC remains quite uncertain. Figure 1.3 compares the direct radiative forcing simulated by a global climate model (National Center for Atmospheric Research Community Earth System Model 1.0) with that obtained based on the empirical approaches in Ramanathan and Carmichael (2008). Both the pattern and magnitude differ between the model and observations. Improving the estimate of BC's forcing magnitude and narrowing down its uncertainty is the first step in understanding its role in climate change.

The in-situ measurement from the Surya program (http://www.projectsurya.org/) for the rural area in the IGP region reveals two major deficiencies of state-of-the art

climate models (e.g. GISS and GFDL models). Firstly, they do not reveal the strong diurnal variations in BC that have been identified from diurnal cycles in cooking practices (Rehman et al., 2011). Furthermore, the absolute concentrations are smaller by a factor of 5 to 10 (also see Menon et al. and Ganguly et al., 2011 for similar results).

1.2.3 An observation-based method to estimate BC forcing: California case study

In light of the model biases, a top-bottom approach that utilized observational constraints to estimate BC forcing has been conducted (Chung et al., 2012). Recently, an international assessment report (Bond et al., 2013) also adopted a similar approach by using ground measurements to correct the model estimate and calculate an empirically verified BC forcing. We recently also carried out a similar approach over California (Bahadur et al., 2012; Xu et al., 2013). The approach is summarized as the following:

We first obtained the total aerosol optical depth (AOD) over California using the Multi-angle Imaging Spectro Radiometer (MISR), on board NASA/Terra from 1998 to 2010. The satellite retrieved AODs that are validated and adjusted by comparisons with Aerosol Robotic Network (AERONET) station observations to obtain the seasonal climatology of AODs. Similarly, based on GOCART model results for different chemical species (sulfate, sea salt, dust, organics and BC) and AERONET observed results, we integrated the climatology of Single Scattering Albedo, which is an indication of the aerosol's absorption ability.

By analyzing the absorption ability at multiple wavelengths (440 nm, 670 nm, 870 nm), we developed a method to calculate the relative contribution of each species (dust,

organics, BC) to the total absorption (Bahadur et al., 2012), and thus separate the carbonaceous aerosol (BC and organics) absorption from the natural background of dust absorption. The role of biomass burning (with a higher organic-to-BC ratio) versus industrial and transportation emissions (with a higher BC-to-organic ratio) of carbonaceous aerosol can also be explored.

By using this method over California, we can demonstrate that AAOD due to carbonaceous aerosols (EC and OC) at 440 nm was 50%–200% larger than natural dust, with EC contributing the bulk (70%–90%). The observationally constrained EC absorption agrees reasonably well with estimates from global and regional chemical transport models, but the models underestimate the OC AAOD by at least 50%. We estimated that the top of the atmosphere (TOA) forcing from carbonaceous aerosols was 0.7 W/m^2 and the TOA forcing due to OC was close to zero. The atmospheric heating of carbonaceous aerosols was 2.2–2.9 W/m^2, of which EC contributed about 80–90%.

1.3 BC's climatic impact

1.3.1 BC influences climate through multiple mechanisms

On a regional scale, particularly for Asian regions, BC aerosols also have a large impact on the climate system, including monsoon variability (Lau et al., 2010), tropical cyclone activities (Evan et al., 2011) and Himalayan glacier retreat (UNEP assessment reports 2011). By changing the Earth's radiative balance, BC can modify latitudinal gradients in sea surface temperature, leading to large-scale circulation changes and perturbations in the regional climate (Ramanathan et al., 2005). BC also has a significant impact on large circulation by changing the horizontal temperature gradient, which will

in turn affect BC's transportation and lifetime through monsoon feedback and precipitation feedback. Specifically, the mechanisms by which BC can influence the climate include:

(a) By reflecting incoming solar radiation back to space, BC and other aerosols directly reduce the solar radiation reaching the surface, which leads to so-called "surface dimming." The surface dimming is a cooling effect that reduces surface evaporation and possibly slows down the hydrological cycle (Ramanathan et al., 2001).

(b) BC can trap sunlight and warm the air. As mentioned above, the absorption of sunlight contributes to both atmospheric heating and surface dimming. The overall effect of BC is a heating effect, denoting positive forcing at the top of the atmosphere.

(c) The excess heating caused by BC can enhance the evaporation of clouds, and such a cloud burning effect is known as the aerosol "semi-direct effect". Recent studies suggest that the impact of BC heating on clouds is not as simple as "burning the cloud" (Koch, 2010); BC heating can either increase or decrease cloud cover, depending on the cloud-aerosol vertical location and the local thermodynamic background. BC, by absorbing solar radiation and enhancing atmospheric heating, may alter the vertical thermal structure of the atmosphere and thus cause a cloud response (Koch, 2010). BC has a further impact on the hydrological cycle by reducing the amount of radiation reaching the surface, thus reducing the water supply to the atmosphere due to evaporation reduction (Ramanathan et al., 2001).

(d) Like all other aerosols, BC can serve as cloud condensation nuclei. Therefore, indirectly, BC aerosols can strongly modify cloud albedo (the first indirect effect) and lifetime (the second indirect effect).

(e) The deposition of BC on snow/ice significantly darkens the surface, altering the surface albedo and accelerating the melting of snow.

1.3.2 Previous studies on the impact of Asian aerosols

With its rapid economical development, China has become the world's largest emitter of BC (Bond et al., 2007). However, study into BC's impact in East Asia is not extensive. The complexity of the East Asia monsoon system makes attribution to BC difficult. Many observational studies on Asian aerosols have suggested that the redistribution of solar energy by aerosols could change atmospheric circulation and the hydrological cycle (Bollasina et al., 2008; Manoj et al., 2010). Previous modeling studies demonstrate how the absorbing aerosols have a significant impact on monsoon rainfall over the Indian sub-continent (Collier et al., 2009; Wang et al., 2009), however the mechanisms and magnitudes of the impact are model dependent.

The effects of aerosols on monsoon rainfall in a coupled model from NCAR (Ramanathan et al., 2005) were found to be different from those in uncoupled models (NASA) with prescribed SSTs (Lau et al., 2006). Meehl et al. (2008) employed CCSM3 (NCAR GCM) and performed model experiments by varying BC aerosols. Their results showed that the radiative effects of BC are significant during the pre-monsoon months (March-April-May) when the dimming effect of BC decreases the surface temperature over India, the Bay of Bengal, and the Arabian Sea.

The work of Menon et al. (2002) highlighted the potential BC climate effect on East Asia, using model results to suggest that the observed "south-wetter, north-drier" pattern in the last few decades in China can be attributed to heavy loading of aerosols. Similar simulations from other models (Liu et al., 2009) did not reproduce this

precipitation trend well. The discrepancy from these model simulations indicates the immature current understanding of BC's climate impact on a regional scale. The complexity of the East Asian monsoon system could also contribute to the difficulty in determining BC's climate impact. Further research that integrates observation and modeling is required to better understand the role of BC in regional climate variability and change.

The model also shows that BC-induced shortwave heating warms the lower troposphere, and the warmer air is advected northwards and manifested by warming over the elevated heat source of the Tibetan Plateau, thus producing an anomalously strengthened meridional temperature gradient throughout the troposphere and enhanced rainfall over most of India. The impact of aerosols on the monsoon and hydrological cycle in South Asia has received increased level of attention due to its significant impact on society. Local governments and the scientific community have started a national assessment initiative on BC climate impact (Indian National Carbonaceous Aerosols Program, 2011).

1.4 Short-lived climate pollutants and climate change mitigation

1.4.1 BC as a short-lived climate pollutant

BC has a significant impact on global radiative forcing. Based on recent assessment reports (IPCC-AR5 and Bond et al., 2013), the current net radiative forcing of BC (0.5 to 1 W/m^2) is estimated to be about half of CO_2 forcing (1.8 W/m^2). Studies have indicated that without immediate action to control BC and other short-lived climate

pollutants (SLCPs, including methane, ozone and halocarbons), CO_2 mitigation alone will not prevent the global mean temperature reaching the 2 degree warming threshold (Ramanathan and Xu, 2010; UNEP assessment report, 2011). Due to their relatively short lifetimes, measures targeting BC and other SLCPs will produce effects quickly, preventing the Earth's temperature from reaching the tipping point by several decades so that large-scale CO_2 mitigation measures can be implemented.

Reductions in BC, tropospheric ozone, HFCs and methane are therefore suggested as the low hanging fruits for slowing down global warming, since the technologies needed to reduce them are available (Ramanathan and Feng, 2008; Ramanathan and Xu, 2010; Molina et al., 2009; Shindell et al., 2012). It has been shown that reducing these pollutants with available technologies would reduce warming during the coming decades by about 0.6 $^{\circ}$C, or 50% (Figure 1.4). Furthermore, given their shorter life times, their climate heating effects will be mitigated on time scales ranging from weeks (for BC) to a few decades (for methane). Accordingly, the US, in partnership with Sweden, Canada, Mexico, Bangladesh, Ghana and the UNEP, has formed the Climate and Clean Air Coalition to Reduce Short-Lived Climate Pollutants (CCAC).

Scientific communities are gradually recognizing that tackling BC and other SLCPs can be a temporary relief for global warming. Due to their shorter lifetime compared with CO_2, measures to control emissions will take effect much more quickly and thus provide more time for the implementation of more complicated measures to control CO_2 emissions. Ramanathan and Xu (2010) assessed the role of including all SLCPs in climate mitigation measures. Their results (Figure 1.4) indicate that the global mean temperature is likely to stabilize below the 2 degree threshold before 2100 only if

BC and SLCPs are taken into account (Figure 1.4, black curve). Even if the world implements aggressive CO_2 emission reduction, failing to take immediate action in controlling these SLCPs will cause the temperature to exceed 2 degrees before 2050 (Figure 1.4, blue curve). This analysis is based on a simple energy balance model and has been confirmed by studies using a more complicated global model from NASA/GISS (Shindell et al., 2013). Since BC and other SLCPs also have negative effects on public health and agriculture, the co-benefits of emission control can be significant.

1.4.2 SLCPs' implications on sea level rise

Under the present growth rates of greenhouse gas and black carbon aerosol emissions, global mean temperatures could warm by as much as 2°C from pre-industrial temperatures by about 2050. Mitigation of the four short-lived climate pollutants (SLCPs), methane, tropospheric ozone, hydrofluorocarbons and black carbon, has been shown to reduce the warming trend by about 50% (Ramanathan and Xu, 2010) by 2050. Hu et al. (2013) focused on the potential impact of this SLCP mitigation on global sea level rise (SLR). The temperature projections under various SLCP scenarios simulated by an energy-balance climate model are integrated with a semi-empirical SLR model derived from past trends in temperatures and SLR to simulate future SLR trends. A coupled ocean–atmosphere climate model is also used to estimate SLR trends due only to the ocean thermal expansion. Our results show that SLCP mitigation can have a significant effect on SLR; it can decrease the SLR rate by 24–50% and reduce the cumulative SLR by 22–42% by 2100. If SLCP mitigation is delayed by 25 years, the warming from pre-industrial temperature exceeds 2°C by 2050 and the impact of

mitigation actions on SLR is reduced by about a third.

1.4.3 Other important SLCPs

Recent studies have estimated that by mitigating emissions of CH_4, BC, and O_3 using available technologies, about 0.5 to 0.6°C warming can be avoided by the mid-21st century. Xu et al. (2013) have showed that avoiding production and the use of high-GWP (global warming potential) HFCs by using technologically feasible low-GWP substitutes to meet the increasing global demand can avoid as much as another 0.5°C warming by the end of the century. This combined mitigation of SLCPs would cut the cumulative warming since 2005 by 50% in 2050 and by 60% in 2100 from the CO_2 -only mitigation scenarios, significantly reducing the rate of warming and lowering the probability of exceeding the 2°C warming threshold during this century.

1.5 The scope of this dissertation

This dissertation has six chapters. After providing the background information and motivation for the thesis in Chapter 1, we will present the main body of research results.

In Chapter 2, we estimate the regional radiative forcing of black carbon. A method for deriving BC's direct forcing from satellite and ground observations has been developed and was applied to East Asia. These observationally derived forcing results will be compared with other state-of-the-art chemical transport models to evaluate the models' performance in simulating the temporal and spatial distribution of BC radiative forcing. The evaluated and improved model is used in Chapter 4 for a better understanding of BC's climate impact.

In Chapter 3, we looked at historical observations and global climate model simulation outputs to understand the internal feature of climate change governed by land-ocean asymmetry. In Chapter 4, we aim to better understand the regional climate impact. To understand how regionally concentrated forcing affects regional climate, we run coupled ocean-atmosphere simulations to estimate BC's impact on the decadal trends of the East Asian climate, with a particular focus on snow response. A better understanding of the magnitude and mechanisms of BC's impact on the observed climate change will build confidence in the climate change mitigation analysis in Chapter 5.

In Chapter 5, we assess the role of BC in climate change mitigation. By evaluating the current BC emission control policy in China, we analyzed BC reduction strategies consistent with their technological feasibility. We used the climate model described in Chapter 4 to examine the impact of such mitigation measures on East Asia's climate. In the last chapter, we provide summaries for each chapter and discuss future research directions.

Figures

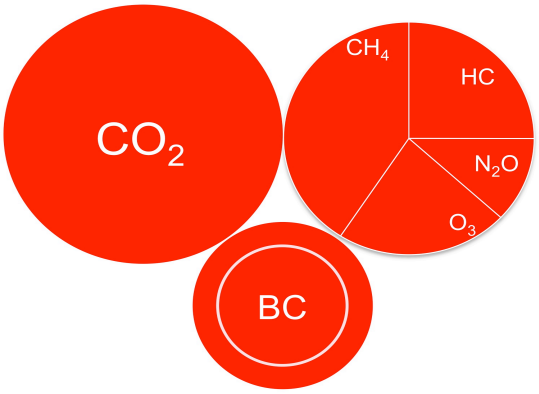

Figure 1.1 Relative contributions of various gases and BC to radiative forcing. The area of each red-shaded circle is proportional to the radiative forcing in 2005. The inner and outer circles for BC show the uncertainty of radiative forcing estimates (0.5 to 0.9 W/m^2). Adapted from Ramanathan and Xu, 2010.

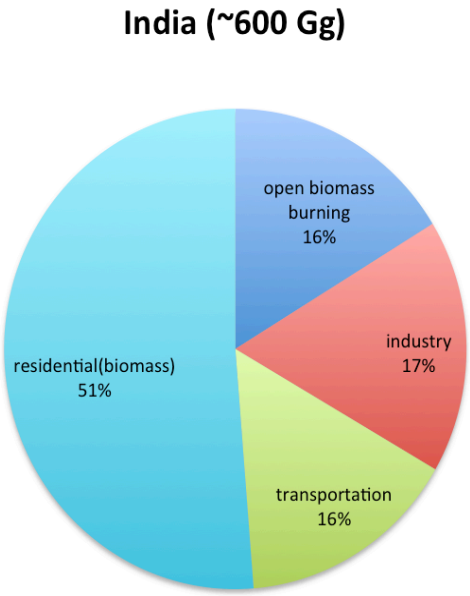

Figure 1.2 Emission sources for black carbon in India (Data from Bond et al., 2004).

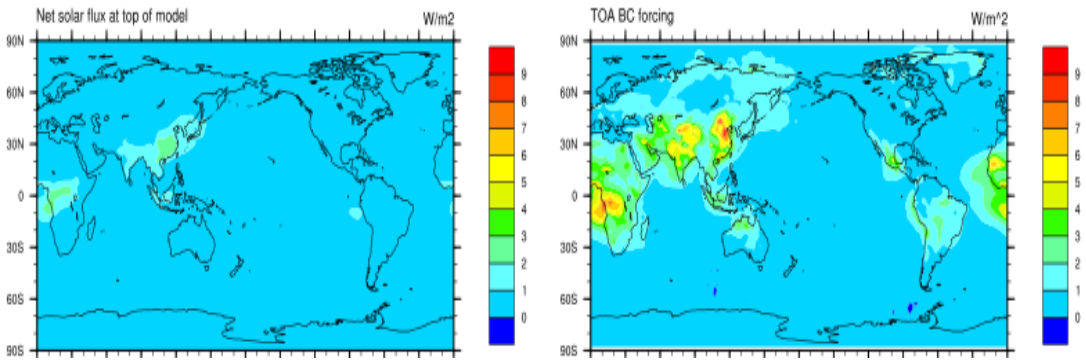

Figure 1.3 Top of atmosphere radiative forcing of BC. (a) Model results from Community Atmospheric Model version 5 (CAM5). (b) Observational estimates from Ramanathan and Carmichael (2008).

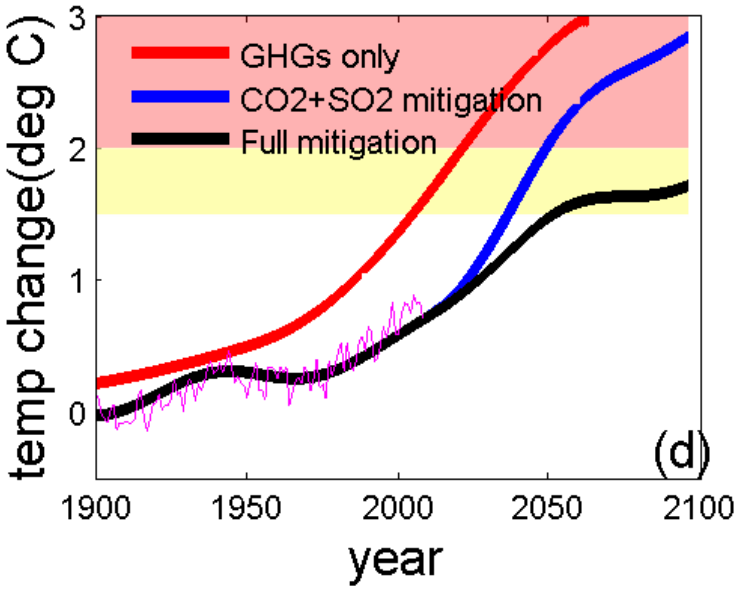

Figure 1.4 Simulation of past and future warming trends under a variety of GHG and SLCP mitigation scenarios. The red line includes only GHGs. The blue and black lines account for GHGs, aerosols and solar and land use change forcing. Beyond 2005, the blue line (CO_2 + SO_2 mitigation) assumes mitigation of CO_2, and includes a reduction in the aerosol cooling effect (due to SO_2 mitigation) from 2015 onward. The black line (full mitigation) is the same as the blue line, except that it further includes the mitigation of SLCPs (methane, BC, HFCs, etc.). The pink and yellow backgrounds show zones beyond 2 °C and 1.5 °C.

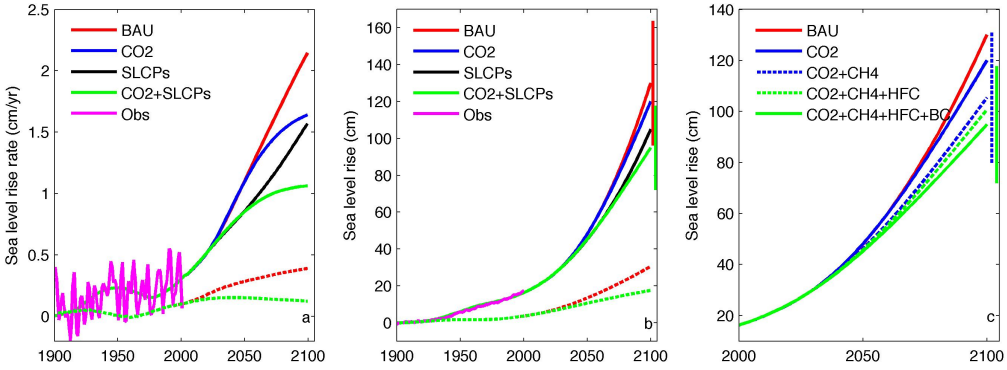

Figure 1.5 SLR changes in different scenarios. (a) The annual rate of SLR. (b) SLR since 1900. Observations are shown from 1900 to 2001. The uncertainty of model-projected SLR at the end of the twenty-first century is shown for the BAU and CO_2 + SLCP cases. The dashed lines indicate model simulations that only consider SLR due to thermal expansion. (c) Contributions of individual SLCPs to SLR since 1900. The uncertainty of model-projected SLR at the end of the twenty-first century, due to the semi-empirical SLR model, is shown for the CO_2 + CH_4 and CO_2 + CH_4 + HFC + BC cases. Note that the contribution of CH_4 also includes the indirect contribution of CH_4 and CO to ozone forcing. CH_4 is methane; BC is black carbon.

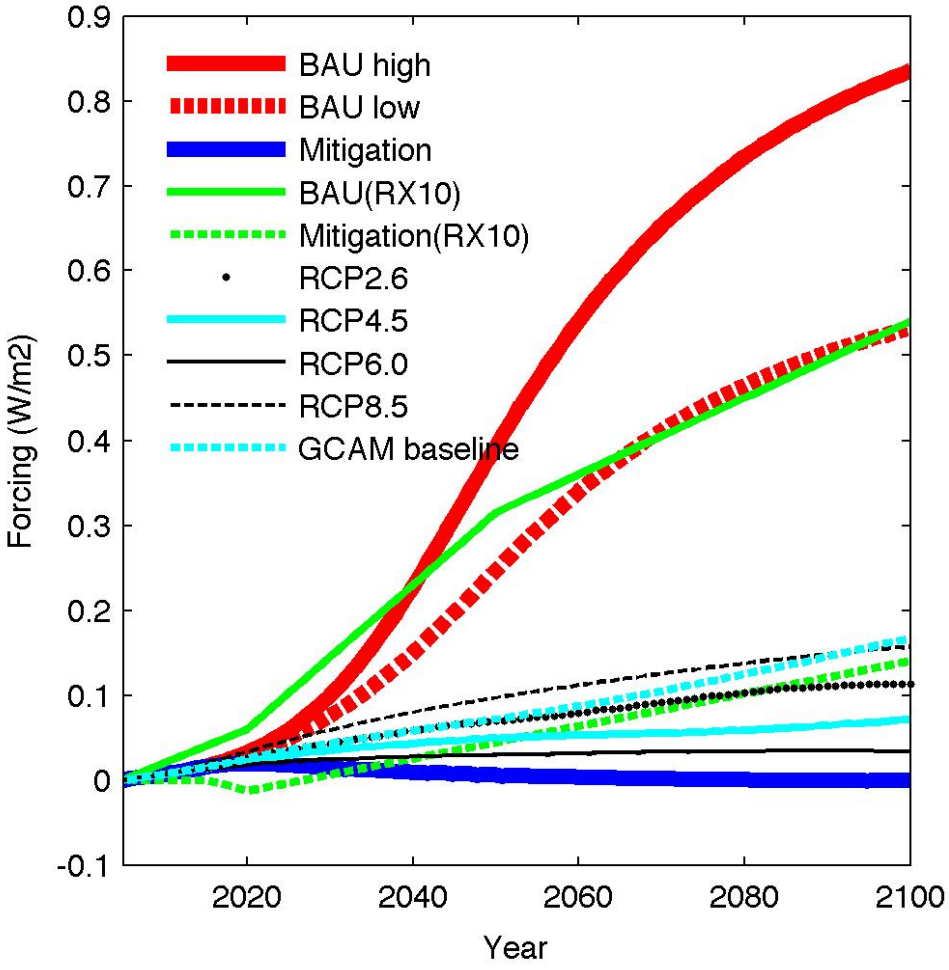

Figure 1.6 HFC radiative forcing change (W/m^2) since the year of 2005. Note we include both the upper (red solid line) and lower limits (red dash line) of HFC growth under BAU scenarios. The scenarios previously adopted in RX10 and from various other sources are shown for reference. Adapted from Xu et al., (2013).

References

Allen, R. J., and S. C. Sherwood (2010), Aerosol-cloud semi-direct effect and land-sea temperature contrast in a GCM, Geophys. Res. Lett., 37, L07702, doi:10.1029/2010GL042759.

Bahadur, R., P. S. Praveen, Y. Xu, and V. Ramanathan (2012), Solar absorption by elemental and brown carbon determined from spectral observations., Proc. Natl. Acad. Sci. U. S. A., 109(43), 17366–71, doi:10.1073/pnas.1205910109. [online] Available from: http://www.pubmedcentral.nih.gov/articlerender.fcgi?artid=3491478&tool=pmcentrez&rendertype=abstract (Accessed 2 December 2013)

Bollasina, M., and S. Nigam (2009), Absorbing aerosols and pre-summer monsoon hydroclimate variability over the Indian subcontinent: The challenge in investigating links, Atmos. Res., 94, 338–344.

Bollasina, M., S. Nigam, and K.-M. Lau (2008), Absorbing aerosols and summer monsoon evolution over South Asia: An observational portrayal, J. Clim., 21, 3221–3239

Bond, T.C. et al. (2007) Historical emissions of black and organic carbon aerosol from energy-related combustion, 1850–2000. Global Biogeochemical Cycles 21, 1-16

Collier, J. C., and G. J. Zhang (2009), Aerosol direct forcing of the summer Indian monsoon as simulated by the NCAR CAM3, Clim. Dyn., 32, 313–332, doi:10.1007/s00382-008-0464-9.

Gautam, R., N. C. Hsu, K.-M. Lau, S.-C. Tsay, and M. Kafatos (2009), Enhanced pre-monsoon warming over the Himalayan-Gangetic region from 1979 to 2007, Geophys. Res. Lett., 36, L07704, doi:10.1029/ 2009GL037641.

Nigam, S., and M. Bollasina (2010), "Elevated heat pump" hypothesis for the aerosol-monsoon hydroclimate link: "Grounded" in observations?, J. Geophys. Res., 115, D16201, doi:10.1029/2009JD013800.

Hu, A., Y. Xu, C. Tebaldi, W. M. Washington, and V. Ramanathan (2013), Mitigation of short-lived climate pollutants slows sea-level rise, Nat. Clim. Chang., 3(5), 1–5, doi:10.1038/nclimate1869. [online] Available from: http://www.nature.com/doifinder/10.1038/nclimate1869 (Accessed 14 April 2013)

Lau, W. K.M., M. K., Kim, K. M. Kim, and W.S. Lee, 2010: Enhanced surface warming and accelerated snowmelt in the Himalayas and Tibetan Plateau induced by absorbing aerosols. Environ. Res. Lett., 5, doi: 10.1088/1748-9326/5/2/025204.

Lau, W. K. M., and K.-M. Kim, 2010: Fingerprinting the impacts of aerosols on long-term trends of the Indian summer monsoon regional rainfall, Geophys. Res. Lett., 37, L16705, doi:10.1029/2010GL043255.

Chen, W.T., Y.H. Lee, P.J. Adams, A. Nenes, and J.H. Seinfeld, Will BC mitigation dampen aerosol indirect forcing?, Geophys. Res. Lett., 37 (L09801), doi:10.1029/2010GL042886, 2010.

Jacobson, M.Z.: Short-term effects of controlling fossil-fuel soot, biofuel soot and gases, and methane on climate, Arctic ice, and air pollution health, J. Geophys. Res.,115, D14209, doi:10.1029/2009JD013795, 2010.

Koch, D., and A. Del Genio (2010), BC semi-direct effects on cloud cover: review and synthesis, Atmos. Chem. Phys., 10, 7685-7696.

Kloster S, Dentener F, Feichter J, Raes F, Lohmann U, Roeckner E, et al. 2009. A GCM study of future climate response to aerosol pollution reductions. Clim Dyn 10.1007/s00382-009-0573-0.

Koch D, Menon S, Del Genio A, Ruedy R, Aleinov I, Schmidt GA. 2009. Distinguishing aerosol impacts on climate over the past century. J Climate 22: 2659-2677.

Lau, K. M., et al., 2010: Enhanced surface warming and accelerated snow melt in the Himalayas and Tibetan Plateau induced by absorbing aerosols, Environ. Res. Lett., 5, 025204.

Levy H, Schwarzkopf MD, Horowitz L, Ramaswamy V, Findell KL. 2008. Strong sensitivity of late 21st century climate to projected changes in short-lived air pollutants. J Geophys Res 113, D06102: doi:10.1029/2007JD009176.

Liu Y, Sun JR, Yang B (2009a). The effects of BC and sulphate aerosols in China regions on East Asia monsoons. TELLUS SERIES B-CHEMICAL AND PHYSICAL METEOROLOGY Volume: 61, Issue: 4 Pages: 642-656

Manoj, M.G., Devera, P.C.S., Safai, P.D. (2010) Absorbing aerosols facilitate transition of Indian monsoon breaks to active spells. Climate Dynamics. DOI 10.1007/s00382-010-0971-3

Ramanathan, V., and Y. Xu (2010), The Copenhagen Accord for limiting global warming: criteria, constraints, and available avenues., Proc. Natl. Acad. Sci. U. S. A., 107(18), 8055–8062, doi:10.1073/pnas.1002293107. [online] Available from: http://www.pubmedcentral.nih.gov/articlerender.fcgi?artid=2889575&tool=pmcentrez&rendertype=abstract (Accessed 18 September 2013)

Randles, C. A., and V. Ramaswamy (2008), Absorbing aerosols over Asia: A Geophysical Fluid Dynamics Laboratory general circulation model sensitivity study of model response to aerosol optical depth and aerosol absorption, J. Geophys. Res.,

Russell, L. M., R. Bahadur, and P. J. Ziemann (2011), Identifying organic aerosol sources by comparing functional group composition in chamber and atmospheric particles., Proc. Natl. Acad. Sci. U. S. A., 108(9), 3516–21, doi:10.1073/pnas.1006461108. [online] Available from: http://www.pubmedcentral.nih.gov/articlerender.fcgi?artid=3048156&tool=pmcentrez&rendertype=abstract (Accessed 19 December 2013)

Shindell, D., and G. Faluvegi, 2009: Climate response to regional radiative forcing during the twentieth century. Nature Geosci., 2, 294-300, doi:10.1038/ngeo473.

United Nation Environment Program. (2011). Integrated Assessment of BC and Tropospheric Ozone. http://www.unep.org/dewa/Portals/67/pdf/Black_Carbon.pdf

Wang, B., Q. Bao, B. Hoskins, G. Wu, and Y. Liu (2008), Tibetan Plateau warming and precipitation changes in East Asia, Geophysical research letters, 35 (14), L14,702.

Wang C, Kim D, Ekman AML, Barth MC, Rasch PJ. 2009. Impact of anthropogenic aerosols on Indian summer monsoon. Geophys Res Lett 36, L21704: doi:10.1029/2009GL040114.

Xu, Y., R. Bahadur, C. Zhao, and L. Ruby Leung (2013), Estimating the radiative forcing of carbonaceous aerosols over California based on satellite and ground observations, J. Geophys. Res. Atmos., 2013JD020654, doi:10.1002/jgrd.50835.

Xu, Y., D. Zaelke, G. J. M. Velders, and V. Ramanathan (2013), The role of HFCs in mitigating 21st century climate change, Atmos. Chem. Phys., 13(12), 6083–6089, doi:10.5194/acp-13-6083-2013. [online] Available from: http://www.atmos-chem-phys.net/13/6083/2013/ (Accessed 3 July 2013)

Chapter 2

Constraining radiative forcing of carbonaceous aerosols over Asia with observations and CESM1/CAM5

Abstract

Carbonaceous aerosols, including black carbon (BC) and organic carbon (OC), are significant contributors to anthropogenic climate change. BC is considered as the second only largest warming agent after CO_2. However, the direct radiative forcing of carbonaceous aerosols is still quite uncertain, in particular over the Asia region. To better quantify the present-day Asian carbonaceous aerosol forcing, we utilize both a top-down approach that is constrained by ground-based and satellite observations over the first decade of the 21st century, as well as a bottom-up approach that is based on a latest global climate model coupled with an interactive chemistry and aerosol module (CESM1/CAM5/MAM3).

The main findings of this study are: (1) By making the comparisons of top-down observational estimates with bottom-up model simulations, we found that the model underestimates atmospheric heating of BC by factors ranging from 2 to 3. The major source of discrepancy between observations and models is speculated to be the published emission inventory, which is developed using limited economic activity data provided by developing countries. A series of sensitivity tests of model simulations are conducted, in

which BC anthropogenic emissions are increased by different factors. These tests suggested that BC emission sources are underestimated by a factor of 2 to 3 over Asia.

(2) By applying a new partitioning scheme to the observed aerosol optical properties, we show that the brown carbon in OC can contribute up to 20% of atmospheric heating by BC. Thus, the overall TOA cooling of OC has been overestimated by earlier studies due to the neglect of brown carbon. The biases of OC forcing in the model simulations are mainly because that the refractive index of OC used in the model are estimated from laboratory measurements rather than from ambient environment observations. In particular, the model currently does not account for brown carbon absorption, leading to a factor-of-two underestimation of its atmospheric heating and consequently an overestimation of TOA cooling. The adjustment of the OC refractive index to match the empirically derived single scattering albedo improved the observation-model agreement.

In summary, model generated BC and OC atmospheric forcing values have to be increased significantly before using the model for examining the climate impacts of carbonaceous aerosols. Our study generates scaling factors for the NCAR climate models, which pave the way for climate impact study.

2.1 Introduction

Recent studies (Ramanathan and Carmichael, 2008; Jacobson, 2010; Chung et al., 2012; Bond et al., 2013; IPCC-AR5, 2013) suggested that the heating effect of black carbon (BC) is significant, possibly only second to CO_2 among all other climate warming agents. The warming induced by BC and other absorbing aerosols is likely to be

responsible for half of the Arctic warming observed over the last few decades (Shindell et al., 2009). Studies have indicated that without immediate action to control BC and other short-lived climate pollutants (SLCPs, including methane, ozone, and halocarbons), CO_2 mitigation alone will not avoid the global mean temperature reaching the 2-degree warming threshold (Ramanathan and Feng, 2008; Ramanathan and Xu, 2010; UNEP, 2011). Due to the relatively short lifetimes of these pollutants, it has been suggested that measures targeting BC and other SLCPs will produce effects quickly, delaying the Earth's temperature reaching the tipping point by several decades for large-scale CO_2 mitigation measures to be implemented (Wallack and Ramanathan, 2009; Ramanathan and Xu, 2010; Shindell et al., 2012).

BC is a major absorber of visible solar radiation in the atmosphere. Heating of the elevated regions by BC, and deposition of BC on snow, are estimated to contribute as much as 50% to the retreat of the Himalayan glaciers (Ramanathan et al., 2007; Flanner et al., 2007; Menon et al., 2010). By changing the Earth's radiative balance on a regional scale, BC and other absorbing aerosols can modify latitudinal gradients in sea surface temperature, leading to large-scale circulation changes and perturbing the regional climate. In addition, the dimming at the surface by BC and other aerosols is linked to the observed weakening of the monsoon in South Asia (Ramanathan et al., 2005). Spatially, BC is concentrated in regions close to its sources, and its non-uniform forcing pattern may lead to a more complicated response pattern. Untangling the coupled ocean-atmosphere impacts of BC from those of greenhouse gases is a major challenge in making decadal projections for regional climate. The consequences of Asia's carbonaceous aerosol on local climate, and the teleconnections with the climate of other

remote regions, is an active field of research (Teng et al., 2012).

Because of the potential consequences of carbonaceous aerosol on climate, careful examination of radiative forcing is warranted. Unfortunately, because of its inhomogeneous distribution and complicated mixing with other aerosols, the radiative forcing of BC is uncertain. This study uses a balanced approach through both available observations and one of the most updated global climate models (Community Earth System Model 1, CESM1), coupled with an aerosol module (Modal Aerosol Model, MAM3) developed by Pacific Northwest National Lab (PNNL). We aimed to constrain the carbonaceous aerosol forcing by conducting modifications to some basic model parameters and by examining whether the model can better represent the aerosol forcing as observed.

2.2 Methods

This research constrains the radiative forcing of carbonaceous aerosols over Asia with observational and modeling approaches. The approaches are illustrated in the schematics of Figure 2.1. The radiative forcing, obtained from observations, serve as a benchmark to evaluate the chemistry transport model's performance in simulating BC's radiative forcing. The modeling approach used aerosol emission inventories to simulate 3-D atmospheric concentrations of aerosols, given the information of the background meteorological field. The models then use the radiative transfer code to calculate the energy flux change due to the existence of aerosols, namely aerosol direct radiative forcing.

2.2.1 "Top-down" observation methods

We obtained total aerosol optical depth (AOD) from MODIS on board NASA/Terra from 2000 to 2010. The satellite-retrieved AODs are validated and adjusted by comparisons with Aerosol Robotic Network (AERONET) station observations for the seasonal climatology of wavelength-dependent AODs. The nudging schemes we used to adjust the satellite-retrieved AODs have been applied to several regional and global studies (Chung et al., 2012; Xu et al., 2013). MODIS provided multiple wavelength measurements over 440 nm, 670 nm, and 870 nm. AERONET has more than 20 sites over East Asia and South Asia for long-term measurement. The inter-comparisons of MODIS and MISR with ground-base AERONET have been intensively documented (e.g. Kahn et al., 2007).

We then used a partitioning scheme (Bahadur et al., 2012; Xu et al., 2013) to exploit the wavelength-dependence of Absorption Angstrom Exponent (AAE) to partition the total optical depths into contribution from BC, OC, and dust. The observation-based single scattering albedo (SSA) then converts the partitioned AAODs into respective AODs (Figure 2.1).

With the observed aerosol optical information, we used the Monte Carlo Aerosol Cloud Radiation model (MACR) to calculate the radiation flux from the surface to the top of the atmosphere. The codes developed for the INDOEX campaign (Podgorny and Ramanathan, 2001) were calibrated by using ground (Kim and Ramanathan, 2008) and unmanned aircraft measurements (Ramana et al., 2007). The MACR has been used in many regional and global aerosol-forcing studies (e.g., Chung et al., 2012; Xu et al., 2013). Two sets of simulations were used to determine the forcing: in one simulation, no

aerosols were used; in the second simulation, only aerosols of interest were included. Calculations under both clear-sky and cloudy-sky conditions were conducted.

In reality, aerosol particles can possibly co-exist with cloud layer at the same altitude, and this 3-D cloud effect is already taken into account by the MACR model (Podgorny and Ramanathan, 2001). A drawback in accounting for this 3-D cloud effect is that only interstitial particles (existing between cloud droplets) are considered. When BC particles are embedded in cloud droplets, these droplets enhance the solar absorption of BC particles (Kim and Ramanathan 2013). In addition, we have used a new scheme in the MACR to account for the enhancement effect from cloud droplet inclusion (Jacobson, 2012). We developed a parameterization scheme to account for this effect, in which the SSA of polluted clouds will be reduced if the cloud layer co-located with a BC layer. Here we assume that BC particles are much smaller than cloud droplets; therefore, all polluted cloud droplets contain at least one BC particle, given that the number of aerosol particles are greater than cloud droplets are. Because the aerosol, cloud, and the necessary water vapor and ozone information are all derived from the observation, we consider the radiative forcing calculated from MACR to be "observational based".

2.2.2 "Bottom-up" modeling methods

The modeling approach used in this study utilized the CESM1, coupled with a newly developed aerosol model - Modal Aerosol Model 3 (MAM3; Liu et al., 2012), which provides internally mixed representations of number concentrations and mass. The simulated aerosols are characterized by a three-radius model (Aitkin, accumulation and coarse mode). The primary carbon (referred to as BC in this study) and organic carbons are categorized into accumulation groups. MAM3 is a compromise between the more

detailed bin aerosol model (Jacobson et al., 2012) and the more computationally effective Bulk Aerosol Model (Tie et al., 2005). Ghan et al. (2012) suggest this model provides the minimal representation of aerosol information for century-long climate simulation. Simple chemistry is also included to account for the oxidation process of sulfate and secondary organic aerosol formation. MAM3 is utilized as the aerosol module for the 21st century climate simulation using CESM1/CAM5 (Meehl et al., 2013).

The radiation scheme in CESM1/CAM5 was updated to the Rapid Radiative Transfer Method for GCMs (RRTMG; Iacono et al., 2008), which employs an efficient and accurate correlated-k method for calculating radiative fluxes and heating rates. RRTMG has an extensive spectral representation of the water vapor continuum, and offline agreement with line-by-line calculations is significantly improved. One additional feature of CESM1/CAM5 is that major physics enhancements provide a physically based estimate of the impact of anthropogenic aerosol emissions on the radiative forcing of climate by clouds (Morris and Gettelman, 2008). In this paper, however, we only focus on the direct effect of aerosols, but a more realistic presentation of cloud climatology, as simulated in the model, is also important for aerosol direct forcing under cloudy-sky conditions.

We ran the model for six years at a nominal 2-degree resolution with prescribed SST and sea ice field at the year of 2000, so that the basic climatology in the simulation was consistent with the observation period of 2000s. The baseline emissions of the year 2000 were from the Representative Concentration Pathway (RCP) emission database (Lamarque et al., 2010), which included primary BC, primary OC, biomass BC/OC, and secondary OC emissions in the gas phase, from both anthropogenic and natural sources.

CESM1/CAM5/MAM3 has a diagnostic function to call another set of radiation flux simulations, in addition to the radiation calculation used in driving the modeled climate. This function provides the direct radiative forcing for total aerosol in clear-sky and cloudy-sky for all aerosols. We then ran the diagnostic simulation with BC (or OC) emissions removed, which yields the direct forcing of all aerosols except BC (or OC). The difference between those two sets of simulations gives us BC (or OC) forcing. The model calculation of the forcing was conducted in a similar manner to Ghan 2012. Note that Ghan et al. (2012) calculated the aerosol forcing as a perturbation since pre-industrial era. Instead of using 1850 emission, we used zero emission in the second set of simulations. Therefore, the calculated forcing from the model can be compared with observational estimates consistently. In that sense, all the forcing results in this paper should be interpreted as "all-source" instead of the forcing since pre-industrial time.

Bond et al. (2013) suggested that the "all-source" forcing is about 30% larger than the forcing since pre-industrial era that potentially drives climate change. However, all-sources forcing are likely to be more relevant for future climate mitigation since forcing from all sources can be mitigated effectively, including biomass burning from forest and savanna. Biomass burning aerosols are not considered as anthropogenic emissions in the model. However, Lamarque et al. (2010) showed that the biomass burning declined during 1900 to 1950 due to less ground clearing effort, which suggested that biomass burning aerosols due to human activities could potentially be mitigated in the future.

2.3 Results

The integrated aerosol optical depth is shown in Figure 2.2. Compared with

original MODIS products (not shown), the integrated AOD are enhanced over a few mega-city regions over Eastern China (Figure 2.2a). The annual average of AOD over Asia is mostly larger than 0.3, suggesting this is one of the highest polluted regions in the world. The highest AOD regions are the East part of China, where the population is intense, and the economic growth is rapid (depicted as North and South China) and the Indo-Gangetic Plain region of India (depicted as North India). Northeastern Asia (Korea and Japan), and Southeastern Asia, also feature high AOD. The transport of pollutants to the North Western Pacific and the North Indian Ocean is also clearly visible. It is also noted that the extent of influences in a latitudinal direction is stronger than the meridional direction.

The high AOD is also visible over desert regions, such as Taklimakan region over Northwestern China and the Thar Desert over Pakistan and Western India. The dust transport from Arabia to the Bay of Arabia is clearly visible. AAOD based on AERONET SSA and integrated AOD, shows a similar pattern of AOD (Figure 2.2b). The partitioned BC and OC AAOD (Figure 2.2 c, d) are based on wavelength dependence of absorption (see method section for details). The contribution of BC to total AAOD is 80% and 70% for China and India, respectively. The application of this partitioning method to the California region found that the OC absorption at 440 nm is about 40% of the BC, dropping off at 675 nm to less than 10% of EC (Xu et al., 2013).

The inter-annual variation of AOD is about 30% of its year-average, mainly due to the meteorological field in those years rather than to emission variation. The model simulation used in this study employs prescribed SST and sea ice of 2000 climatology, but the aerosol field and meteorology are fully interacted; therefore we can simulate the

inter-annual variation of AOD quite well. As for the seasonal variation, aerosols over China in the winter are about three times larger than the summer, because of both the increased emission of winter residential heating and less monsoon rainfall in the winter. In the model simulation, however, emissions have no seasonal cycle except for biomass burning sources, which are not significant over most of Asia.

The atmospheric forcing of BC and OC, from both observation and models, is shown in Figure 2.3. The climatology of forcing is consistent with the AOD/AAOD pattern. We compare the forcing results with that from CESM1/CAM5/MAM3 in Table 2.1. The model underestimates the atmospheric heating by a factor of 2 to 4. We are mostly concerned with the atmospheric heating (W/m^2), rather than the TOA forcing, and used it as a benchmark to evaluate model performance because the observational AAOD is directly retrieved from observation, while the AOD is calculated indirectly from the empirically derived SSA. If the MISR dataset is used instead of MODIS, the AAOD and the corresponding atmospheric forcing is smaller by 20%. Our comparisons and earlier studies suggest that MODIS products are more reliable than MISR over the high AOD region. However, MODIS does have a problem over high surface albedo regions (e.g. snow pack and desert), which might explain the unusually high BC AOD over desert regions (Figure 2.2a).

2.4 Discussions

The parameterization schemes in the model, to represent the mixing state of aerosols and their optical properties, introduce uncertainty in the BC forcing estimate. We test the model sensitivity of model version using different chemical packages available in

CESM, including MAM3 and MAM7. Those two modal aerosol models are developed by the DOE/PNNL group, one with three aerosol size bins and the other with seven. We also explore the uncertainty due to the selection of emission inventory and model parameterizations.

2.4.1 Sensitivity of model version

We first tested the model sensitivity based on a more detailed model - MAM7 (Liu et al., 2012), in which primary carbon and organic carbon are categorized under a separate mode. MAM7 is suggested to outperform MAM3 in simulating Arctic black carbon in high latitude and high altitude, by comparing with field campaign data of HIPPO. The default version of the aerosol model is MAM3 for century long climate simulation of CESM1/CAM5 as it is at least 50% more computationally efficient than MAM7. The result of MAM7 is nearly identical (within 10%) with that of MAM3. This suggests that over regions close to the emission sources the aerosol concentrations are mainly determined by the emission intensity rather than the simulated lifetime in the model.

2.4.2 Emission inventory biases

Bond et al. (2013) suggested that BC emission inventory biases are large over Asia. To test the model's sensitivity to the emission inventory, we arbitrarily increased the emission over regions in Asia by a factor of two. The results from doubled-emission simulation suggest that atmospheric forcing is scaled linearly with emission intensity. Therefore, we propose that we can simply scale the emission to match with the forcing if we want to attain a realistic representation of forcing for the long-term climate

simulations.

After comparing standard CESM simulation results, in which the baseline emission inventory of the year 2000 are used, with our observational estimates and previous estimates (Chung et al., 2012), we came up with "optimal adjusting factors" for individual parts of Asia (North China: 3, South China, 4; North India: 2.5; South India: 4). The emissions from other parts of the world are increased by a factor of 2 following Bond et al., 2013. The scaled forcing results are shown in Table 2.1(BC atmospheric forcing). After the adjustment, the global TOA forcing of BC is 0.8 W/m^2 compared to the default version of 0.4 W/m^2. Bond et al. (2013) suggested all source forcing is 0.9 W/m^2, while the observation-based study of Chung et al. (2012) calculates global forcing of 0.75 W/m^2 for black carbon. So, our adjusted forcing globally agrees well with latest estimates. Regionally, the adjusted modeled forcing falls into the range of our observationally constrained estimates (Section 2.3.2) and similar approaches utilizing different dataset and partitioning schemes (Chung et al., 2012). For the detailed description of how the method presented here is improved from Chung et al., 2012, readers are referred to Bahadur et al., (2012) and Xu et al., (2013).

Note these numbers are all-source BC forcing (present-day minus zero), and the forcing at 1850 is subject to additional biases of historical emission and is difficult to be constrained by observations. The CESM model produced 1850 forcing of 0.15 W/m^2 with the range of 0.1 (Chung et al., 2012) to 0.2 W/m^2 (Bond et al., 2013) of previous studies. We based our emission intensity adjustment on atmospheric forcing (W/m^2) for the reasons previously discussed. We note that if the focus is to validate atmospheric chemistry properties, more constraints from surface or aircraft measurement are needed.

Here we further discuss the possible reasons of emission inventory biases. The major sources of BC in East Asia include fossil fuel burning for industry and transportation, residential use of coal and biofuel and open-biomass burning (Figure 2.4). The anthropogenic sources are mostly energy-related. The inventory of Bond et al., (2007) is recently updated in the Representative Concentration Pathway database as discussed in Lamarque et al., (2010), and it is still the most updated global BC emission database and recommended for use in IPCC/AR5 model inter-comparisons. Regional BC emission inventories in China have been developed by various groups (see a summary in Table 2.2). Early studies also include Streets et al. (2001), which comprehensively studied China's BC emissions. A more local prospective is provided by Cao et al. (2007), which estimates BC emission by using local data of energy use and emission factors. The most recent study (Zhang et al., 2009) estimated that China's share in Asian energy-related BC emissions was over 60% in 2006. According to these studies, the sources of BC in China are mainly energy-related (coal combustion), and thus could be more profound in radiative effect due to a higher BC/OC ratio compared with emissions from biomass burning.

The BC emission inventory is generally developed by a bottom-up approach by using energy use and economic activity statistics, which have a high uncertainty of 50% to 100% (Bond et al., 2004). The data taken for the rural area in the Indo-Gangetic Plain region over India revealed two major deficiencies in state-of-the-art climate models (e.g. GISS and GFDL models). First, these models do not capture the strong diurnal variations in the BC that have been identified with diurnal cycles in cooking practices (Rehman et al., 2011). Furthermore, the concentrations of BC at the surface are smaller by a factor of

5 to 10 as also shown by other studies (Menon et al., 2010; and Ganguly et al., 2011), which may be the results of the model's shortcoming in including a realistic emission inventory.

BC emission is mainly due to incomplete combustion of carbonaceous matters. In general, energy uses are divided into several main sectors (industry, residential, and transportation), and divided further, based on fuel type (coal, diesel, gas, firewood, and crops) and combustion technology (traditional or improved); thus, BC emissions can be segregated into more than one hundred source classifications. Emissions in each source classification are estimated as the following: Fuel use (ton)* emission factor (kg/ton) = emission (kg). A key uncertainty in the calculation is emission factors. Emission factors are reported from controlled combustion experiments and local in-situ observations; however, these are subject to a lot of uncertainty due to inadequate measurements.

The top-down approaches adopted here illustrate how the observations, in particular from satellite, can help constrain model simulation. Other ways of assimilating observational information (such as from in-situ measurements) directly into high-resolution regional models are greatly needed, in order to better constrain the emission inventory, in particular to identify whether the biases of the inventory come from emission factors or the combustion sources.

2.4.3 Radiative parameters: implications on organic carbon absorption

Both black carbon and organic aerosols absorb and scatter solar radiation. BC absorption dominates scattering and hence it has a net heating effect. OC is normally assumed to have negligible absorption, and, as a result, its strong scattering effects lead to a cooling in climate models. However, data over the Indo-Gangetic Plain region of India,

and measurements over biomass burning regions of Africa (Magi et al., 2010), reveal strong absorption by organics in biomass burning regions. The absorbing organics are referred to as Brown Carbon (Andreae and Gelencser, 2006).

The model results are also sensitive to the choice of radiation parameters, such as refractive indexes. One notable feature of the model simulation is that the adjusted model has a larger TOA forcing than observation, despite having an atmospheric heating smaller than observation (Table 2.1). To address the non-correspondence of TOA and atmospheric forcing, we try to modify the refractive index, which is a key parameter in models, including in MAM3. Refractive indexes for most of species are from the OPAC dataset (Hess et al., 1998). BC refractive index in CESM1 is updated with Bond and Bergstrom (2006).

Bahadur et al. (2012), however, empirically derive the BC/OC SSA from ambient environment by exploiting the AERONET dataset close to representative regions. This alternative approach to attain BC/OC SSA may lead to a different interpretation of the results. BC SSA in our study, derived from an ambient environment measurement, is more like industrial sources containing 90% of BC. The OC SSA in our study has shown characteristics of biomass burning carbonaceous aerosols, which is 70% of OC. Therefore; our BC is not as “black” as the model simulation (see the wavelength dependence of SSA in Figure 2.5) and our OC is considered more “brown” than that in the model simulation.

To test the model sensitivity to the radiative parameter, we modified the standard OC SSA in the model to agree with Bahadur et al. (2012) (Figure 2.5). Bahadur et al. (2012) only derived SSA over three wavelengths (440 nm, 670 nm, and 870 nm), so we

extended the SSA into a shorter wavelength to cover the full spectrum required by model calculation. We note that after the adjustment of OC SSA, model simulated OC atmospheric heating has a better agreement compared with observational estimates and the results from Chung et al. (2012) (Table 2.3). These sensitivity tests of OC SSA demonstrate the importance of parameterization in radiative calculation in the model.

In this study we considered only primary organic carbon emission in the modeled simulation and we only modified the refractive index of primary organic carbon (defined as hydrophobic species in MAM3) in the sensitivity experiments. The reasons that we did not attempt to quantify the gas emission of secondary organic matters (SOA) are: (1) their emission is not well represented in the RCP emission dataset so we cannot apply an adjusting factor as we did to BC; (2) modeling the transformation from SOA to organic carbon aerosol particles is still challenging; (3) based on in-situ experiments the absorption of hydrophilic organic carbon is not significant (Feng et al., 2013)

2.5 Conclusions

From our sensitivity test with the model version and emission inventory, we conclude that the major sources of model-observation discrepancy are due to emission inventory. We note that the baseline emission in our study is scaled to the year 2000 economics activity data (with respective population and GDP), while our observation is based on more recent years (2000-2010) when such a multiple satellite dataset was available (in particular over land regions). Therefore, in principle, the time period difference in itself may already explain part of the model-observation discrepancy, because the economic growth in both China and India were quite rapid during the first

decade of the 21st century. Given the rapid growth of economy, the bottom-up development of emission inventory is considerably difficult. The sensitivity tests suggested the emission inventory over the Asia region is off by a factor of two to four. After we scaled the default emission by different factors in different regions, the simulated forcing agrees with observational estimates much better in magnitude and spatial pattern. In our sensitivity experiment, in which the aerosol module is replaced with a more sophisticated treatment (MAM7) that has weaker scavenging process and longer aerosol lifetime, the simulated forcing still has quite large biases compared to observational estimates. This implies that the major source of forcing biases is the emission inventory.

The model modification we conducted to the organic refractive index revealed another model deficiency – lack of inclusion of "brown carbon" absorption. We show that by using a more observation-based parameterization scheme, the atmospheric heating of organic carbon is agreeing with observation estimates better, and the TOA forcing organic carbon is still negative but smaller in magnitude.

In general, the study here demonstrates an effective top-down strategy for improving the model simulation of the climate impacts of carbonaceous aerosols. Our top-down approach involves retrieval of the forcing from satellite and ground-based aerosol optical properties as described in Chung et al. (2005) and modified by Chung et al. (2012), Bahadur et al. (2012) and Xu et al. (2013). This observationally constrained forcing is used to adjust the model-generated forcing, and the adjustment factor is applied to the emission inventory used in the models. The most critical observations we need are aerosol absorption of solar radiation; this is provided by the AERONET network (Holben

et al., 2001). We note that AERONET sites over East Asia and India (as well as Africa) are scarce, and long-term monitoring has been terminated due to malfunctions or lack of funds. Therefore, the observational network at national level (Zhang et al., 2012) and the studies that utilize dataset in calibrating satellite and regional chemistry models are very useful. At the least, intensive observational campaigns are needed to constrain the emission inventory and to improve understanding of the chemical transport mechanism of carbonaceous aerosols.

Tables

Table 2.1 BC TOA and atmospheric (Atm) forcing estimates (W/m^2) based on various methods.

BC TOA (W/m^2)	CESM (standard)	Chung et al., 2012	This study (AOD: MODIS+AERONET, SSA: GOCART+AERONET)	CESM (modified regionally and, globally *2)
North China	1.9	3.6	1.7	4.3
South China	2.4	3.1	1.7	4.5
North India	1.8	3.0	2.8	4.6
South India	1.1	2.2	1.1	2.8
Global	0.4	0.8	-	0.7

Table 2.1 Continued.

BC Atm (W/m^2)	CESM (standard)	Chung et al., 2012	This study (AOD: MODIS+AERONET, SSA: GOCART+AERONET)	CESM (modified regionally and, globally *2)
North China	5.3	15.1	10.8	12.9
South China	5.4	11.4	9.1	11.0
North India	5.6	9.7	14.3	13.4
South India	3.8	9.3	9.6	8.6
Global	0.9	2.7	-	1.5

Table 2.2 Estimates of BC and OC emission from various groups.

1st author	2nd author	affiliation	pub year	chemical species	study region	time period	baseline year	BC/OC(Mt)	from biomass
Bond	Streets	UIUC	2004	BC	Global		1996	1.4/2.1	0.1/0.7
Ito	Penner	Michigan	2005	BC	Global	1950-2000			
Cao	Zhang	China	2006	BC	China		2000	1.4/3.7	0.1/0.4
Ohara	Akimoto	Japan	2007	aerosol	Asia	1980-2020	2000	1.1/2.6	
Junker	Liousse	France	2008	BC	Global	1860-1997	1997	1 for BC	
Zhang	Streets	Agonne	2009	aerosol	Asia		2001	1.6/2.8	
Klimont	Cofala	Austria	2009	aerosol	Asia	1990-2030	2000	1.3/3.2	

Table 2.3 OC atmospheric forcing (W/m^2) from various sources.

OC Atm heating (W/m^2)	CESM (standard)	Chung et al., 2012	This study (AOD:MODIS+AERONET, SSA:GOCART+AERONET)	CESM (modified)
North China	0.8	3.3	1.2	2.4
South China	1.3	2.9	1.6	2.8
North India	1.3	4.4	2.8	3.9
South India	1.0	4.7	1.8	2.9
Global	0.2	1.2	-	0.5

Figures

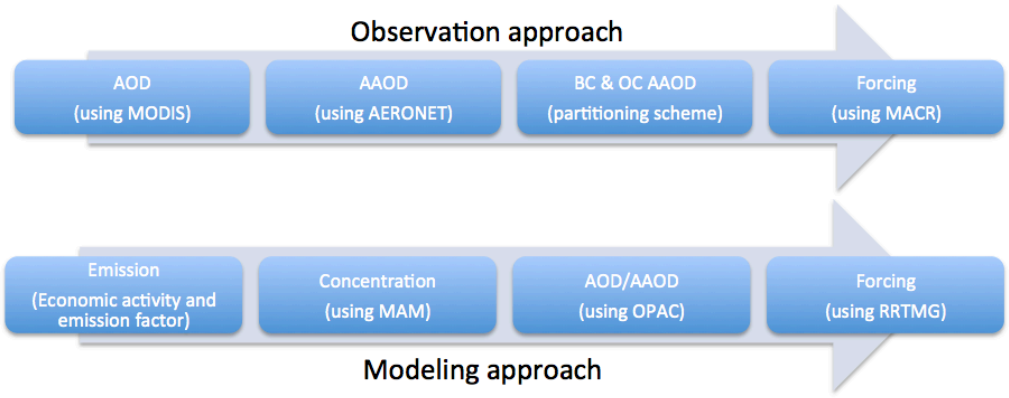

Figure 2.1 Schematics of the observational approaches and modeling approaches.

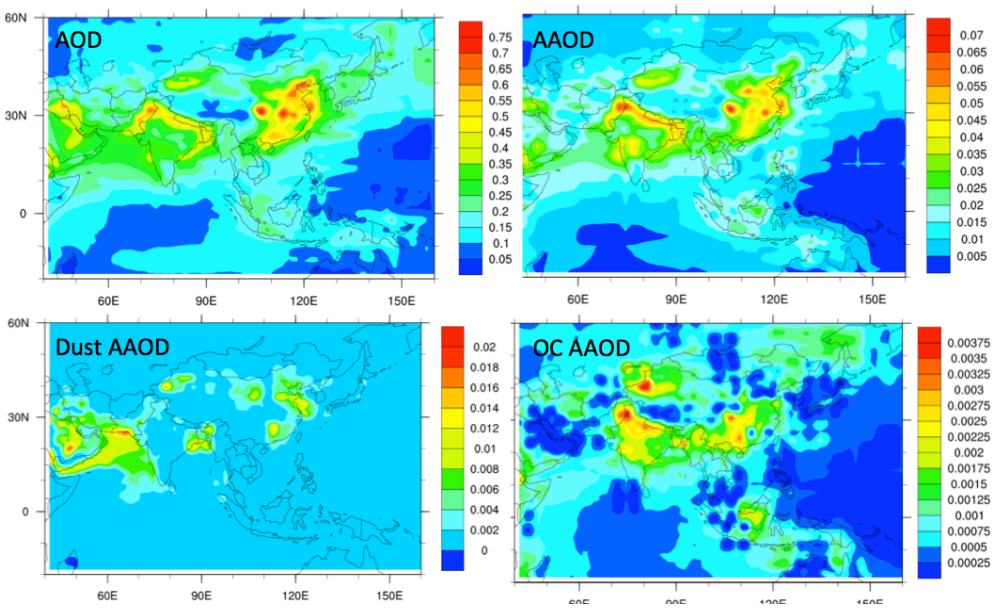

Figure 2.2 (a) Observational AOD from 2001 to 2011 and (b) retrieved AAOD. With four interested regions shown in boxes. (c) Partitioned AAOD due to dust; (d) Partitioned AAOD due to OC.

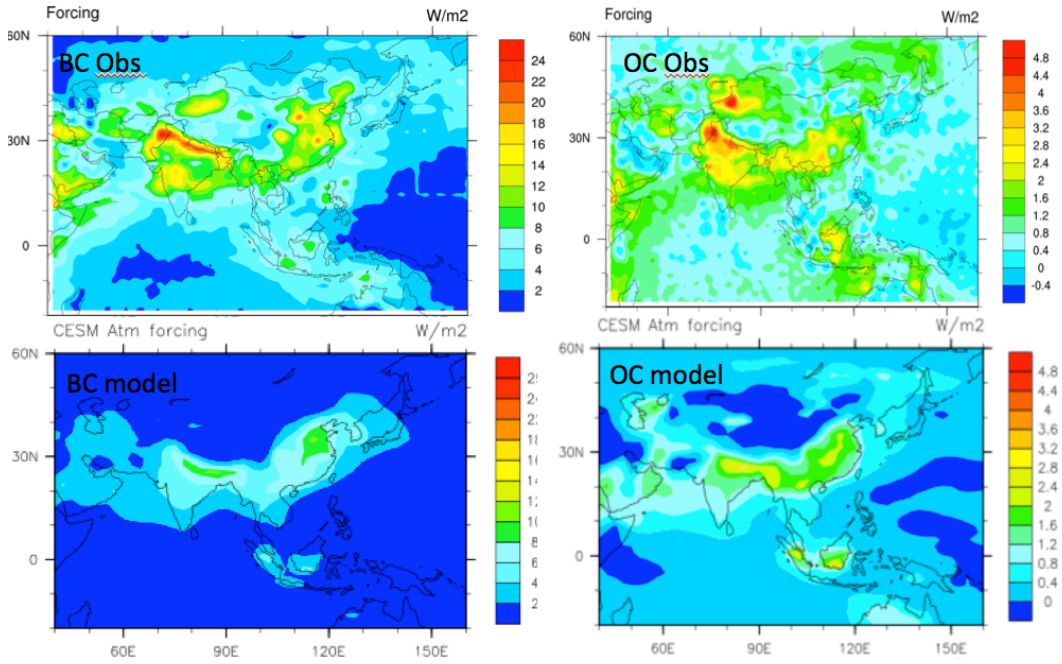

Figure 2.3 Atmospheric heating (W/m^2) of BC and OC from observational estimates, and from CESM1.

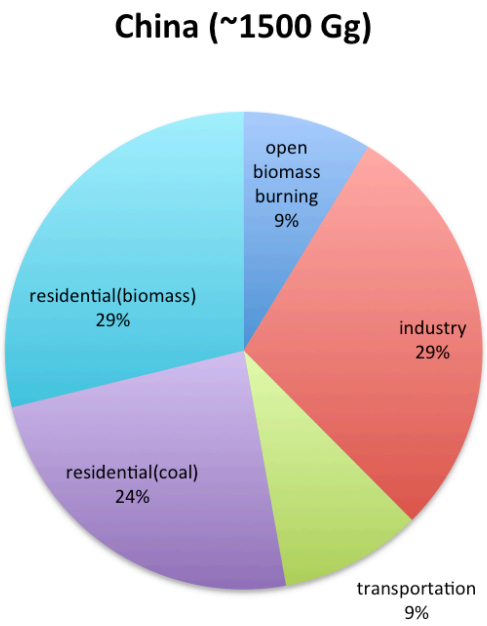

Figure 2.4 Yearly emission sources for Black Carbon in China (data source: Bond et al., 2004).

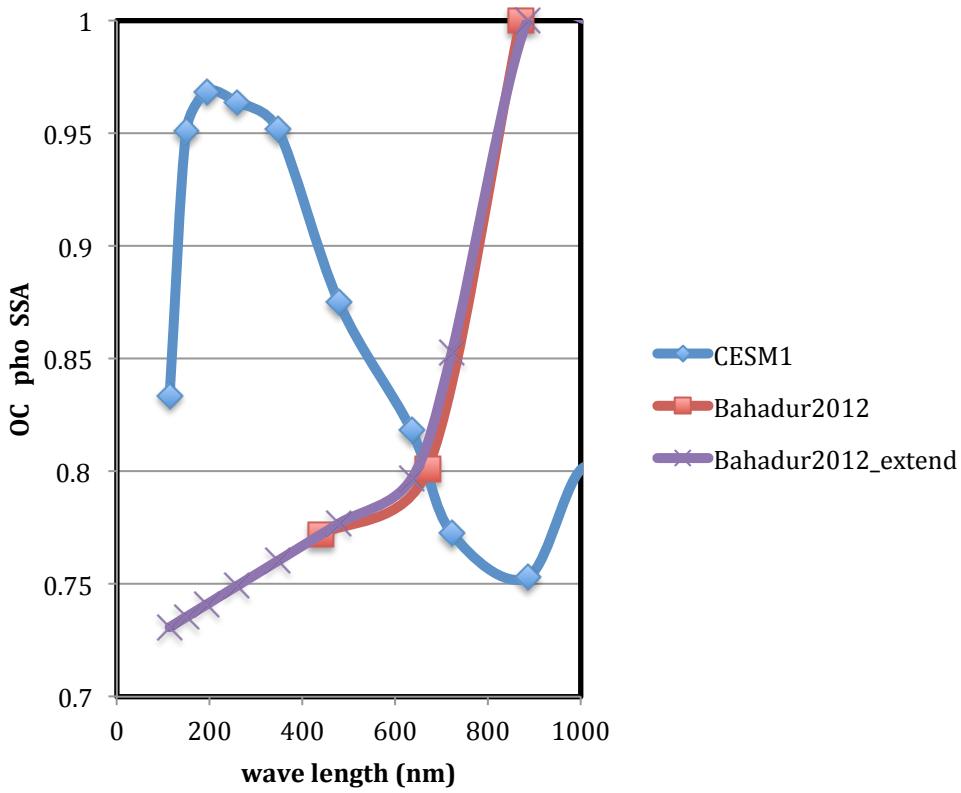

Figure 2.5 The SSA of insoluble OC (depicted as OC pho) in Y-axis label used from CESM1 at different wavelength as well as and the adjustment made based on Bahadur et al., (2012).

References

Andreae, M. O., A. Gelencs, P. O. Box, and H.- Veszpr (2006), and Physics Black carbon or brown carbon ? The nature of light-absorbing carbonaceous aerosols, , 3131–3148.

Bahadur, R., P. S. Praveen, Y. Xu, and V. Ramanathan (2012), Solar absorption by elemental and brown carbon determined from spectral observations., Proceedings of the National Academy of Sciences of the United States of America, 109(43), 17366–71, doi:10.1073/pnas.1205910109. Bond, T. C., D. G. Streets, K. F. Yarber, S. M. Nelson, J. Woo, and Z. Klimont (2004), A technology-based global inventory of black and organic carbon emissions from combustion, , 109, 1–43, doi:10.1029/2003JD003697.

Bond, T. C., D. G. Streets, K. F. Yarber, S. M. Nelson, J. Woo, and Z. Klimont (2004), A technology-based global inventory of black and organic carbon emissions from combustion, J. Geophys. Res., 109(D14), D14203, doi:10.1029/2003JD003697. [online] Available from: http://doi.wiley.com/10.1029/2003JD003697 (Accessed 18 September 2013)

Bond, T. C., and R. W. Bergstrom (2006), Light Absorption by Carbonaceous Particles: An Investigative Review, Aerosol Science and Technology, 40(1), 27–67, doi:10.1080/02786820500421521.

Bond, T. C., E. Bhardwaj, R. Dong, R. Jogani, S. Jung, C. Roden, D. G. Streets, and N. M. Trautmann (2007), Historical emissions of black and organic carbon aerosol from energy-related combustion, 1850-2000, Global Biogeochemical Cycles, 21(2), n/a–n/a, doi:10.1029/2006GB002840.

Bond, T. C. et al. (2013), Bounding the role of black carbon in the climate system: A scientific assessment, Journal of Geophysical Research: Atmospheres, 118(11), 5380–5552, doi:10.1002/jgrd.50171.

Cao, G., X. Zhang, and F. Zheng (2006), Inventory of black carbon and organic carbon emissions from China, Atmos. Environ., 40(34), 6516–6527, doi:10.1016/j.atmosenv.2006.05.070.

Chung, C. E., V. Ramanathan, and D. Decremer (2012), Observationally constrained estimates of carbonaceous aerosol radiative forcing, doi:10.1073/pnas.1203707109/-/DCSupplemental.www.pnas.org/cgi/doi/10.1073/pnas.1203707109.

Flanner, M. G., C. S. Zender, J. T. Randerson, and P. J. Rasch, 2007: Present-day climate forcing and response from black carbon in snow. J. Geophys. Res., 112, D11202, doi:10.1029/ 2006JD008003.

Ganguly, D., P. Ginoux, V. Ramaswamy, D. M. Winker, B. N. Holben, and S. N. Tripathi (2009),Retrieving the composition and concentration of aerosols over the Indo-Gangetic basin using CALIOP and AERONET data, Geophys. Res. Lett., 36, L13806, doi:10.1029/2009GL038315.

Ghan, S. J., X. Liu, R. C. Easter, R. Zaveri, P. J. Rasch, J.-H. Yoon, and B. Eaton (2012), Toward a Minimal Representation of Aerosols in Climate Models: Comparative Decomposition of Aerosol Direct, Semidirect, and Indirect Radiative Forcing, Journal of Climate, 25(19), 6461–6476, doi:10.1175/JCLI-D-11-00650.1.

Holben, B. N., et al. (2001), An emerging ground-based aerosol climatology: aerosol optical depth from AERONET, J. Geophys. Res., 106, 12067–12097, doi:10.1029/2001JD900014.

Iacono, M.J., J.S. Delamere, E.J. Mlawer, M.W. Shephard, S.A. Clough, and W.D. Collins, Radiative forcing by long-lived greenhouse gases: calculations with the AER radiative transfer models, J. Geophys. Res., 113, D13103, doi:10.1029/2008JD009944, 2008.

IPCC (2013), "Climate Change 2013: The Physical Science Basis. Working Group I Contribution to the IPCC 5th Assessment Report - Changes to the Underlying Scientific/Technical Assessment". Chapter 7: Clouds and Aerosols

Jacobson, M. Z. (2010), Short - term effects of controlling fossil - fuel soot , biofuel soot and gases , and methane on climate , Arctic ice , and air pollution health, , 115, doi:10.1029/2009JD013795.

Jacobson, M. Z. (2012), Investigating cloud absorption effects: Global absorption properties of black carbon, tar balls, and soil dust in clouds and aerosols, Journal of Geophysical Research, 117(D6), D06205, doi:10.1029/2011JD017218.

Kahn, R. a., M. J. Garay, D. L. Nelson, K. K. Yau, M. a. Bull, B. J. Gaitley, J. V. Martonchik, and R. C. Levy (2007), Satellite-derived aerosol optical depth over dark water from MISR and MODIS: Comparisons with AERONET and implications for climatological studies, Journal of Geophysical Research, 112(D18), D18205, doi:10.1029/2006JD008175.

Kim, D., and V. Ramanathan (2008), Solar radiation budget and radiative forcing due to aerosols and clouds, Journal of Geophysical Research, 113(D2), D02203, doi:10.1029/2007JD008434.

Kim, D., and V. Ramanathan (2012), Improved estimates and understanding of global albedo and atmospheric solar absorption, Geophysical Research Letters, (July), 1–22.

Lamarque, J., and T. Bond (2010), Historical (1850–2000) gridded anthropogenic and biomass burning emissions of reactive gases and aerosols: methodology and application,

… and Physics, 7017–7039, doi:10.5194/acp-10-7017-2010.

Liu, X. et al. (2012), Toward a minimal representation of aerosols in climate models: description and evaluation in the Community Atmosphere Model CAM5, Geoscientific Model Development, 5(3), 709–739, doi:10.5194/gmd-5-709-2012.

Meehl, G. a., W. M. Washington, J. M. Arblaster, A. Hu, H. Teng, J. E. Kay, A. Gettelman, D. M. Lawrence, B. M. Sanderson, and W. G. Strand (2013), Climate change projections in CESM1(CAM5) compared to CCSM4, Journal of Climate, 1, 130306100525002, doi:10.1175/JCLI-D-12-00572.1.

Menon, S., D. Koch, G. Beig, S. Sahu, J. Fasullo, and D. Orlikowski (2010), Black carbon aerosols and the third polar ice cap, Atmospheric Chemistry and Physics, 10(10), 4559–4571, doi:10.5194/acp-10-4559-2010.

Morrison, H. and A. Gettelman, A new two-moment bulk stratiform cloud microphysics scheme in the Community Atmospheric Model (CAM3), Part I: Formulation and Numerical Tests, J. Climate, 21:15, 3642-3659, 2008

Podgorny, I. A., and V. Ramanathan (2001), A modeling study of the direct effect of aerosols over the tropical Indian Ocean, J. Geophys. Res., 106(D20), 24097–24105, doi:10.1029/2001JD900214.

Ramana, M.V., V. Ramanathan, D. Kim, G.C. Roberts and C.E. Corrigan (2007). Albedo, Atmospheric Solar Absorption and Heating rate measurements with stacked UAVs, Quart. J. Roy. Meteor. Soc., 133, 1913-1931.

Ramanathan, V., M. V Ramana, G. Roberts, D. Kim, C. Corrigan, C. Chung, and D. Winker (2007), Warming trends in Asia amplified by brown cloud solar absorption., Nature, 448(7153), 575–8, doi:10.1038/nature06019. [online] Available from: http://www.ncbi.nlm.nih.gov/pubmed/17671499 (Accessed 18 September 2013)

Ramanathan, V., and G. Carmichael (2008), Global and regional climate changes due to black carbon, Nat. Geosci., 221–227. [online] Available from: http://www.nature.com/ngeo/journal/vaop/ncurrent/full/ngeo156.html (Accessed 7 November 2013)

Ramanathan, V., and Y. Feng (2008), On avoiding dangerous anthropogenic interference with the climate system: formidable challenges ahead., Proc. Natl. Acad. Sci. U. S. A., 105(38), 14245–50, doi:10.1073/pnas.0803838105. [online] Available from: http://www.pubmedcentral.nih.gov/articlerender.fcgi?artid=2567151&tool=pmcentrez&rendertype=abstract

Ramanathan, V., and Y. Xu (2010), The Copenhagen Accord for limiting global warming: criteria, constraints, and available avenues., Proceedings of the National Academy of Sciences of the United States of America, 107(18), 8055–8062.

Ramanathan, V., C. Chung, D. Kim, T. Bettge, L. Buja, J. T. Kiehl, W. M. Washington, Q. Fu, D. R. Sikka, and M. Wild (2005), Atmospheric brown clouds: impacts on South Asian climate and hydrological cycle., Proceedings of the National Academy of Sciences of the United States of America, 102(15), 5326–33, doi:10.1073/pnas.0500656102.

Rehman, I.H., T. Ahmed, P.S. Praveen, A. Kar, and V. Rmanathan (2011) Black carbon emissions from biomass and fossil fuels in rural India Atmos. Chem. Phys., 11, 7289–7299

Shindell, D. et al. (2012), Simultaneously mitigating near-term climate change and improving human health and food security., Science (New York, N.Y.), 335(6065), 183–9, doi:10.1126/science.1210026.

Shindell, D., and G. Faluvegi (2009), Climate response to regional radiative forcing during the twentieth century, Nature Geoscience, 2(4), 294–300, doi:10.1038/ngeo473.

Streets, D. G., S. Gupta, S. T. Waldhoff, M. Q. Wang, T. C. Bond, and B. Yiyun (2001), Black carbon emissions in China, Atmos. Environ., 35(25), 4281–4296, doi:10.1016/S1352-2310(01)00179-0.

Teng, H., W. M. Washington, G. Branstator, G. A. Meehl, and J.-F. Lamarque (2012), Potential impacts of Asian carbon aerosols on future US warming, Geophys. Res. Lett., 39, L11703, doi:10.1029/2012GL051723.

Tie, X. X., Madronich, S., Walters, S., Edwards, D. P., Ginoux, P., Mahowald, N., Zhang, R. Y., Lou, C., and Brasseur, G.: Assessment of the global impact of aerosols on tropospheric oxidants, J. Geophys. Res., 110, D03204, doi:10.1029/2004JD005359, 2005

UNEP. Integrated Assessment of Black Carbon and Tropospheric Ozone. 2011.

Venkataraman, C., G. Habib, a Eiguren-Fernandez, a H. Miguel, and S. K. Friedlander (2005), Residential biofuels in South Asia: carbonaceous aerosol emissions and climate impacts., Science (New York, N.Y.), 307(5714), 1454–6, doi:10.1126/science.1104359.

Wallack, J and Ramanathan, V. (2009) The Other Climate Changes, Why Black Carbon Also Matters, Foreign Affairs, Sept/Oct 2009, pp. 105-113.

Xu, Y., R. Bahadur, C. Zhao, and L. Ruby Leung (2013), Estimating the radiative forcing of carbonaceous aerosols over California based on satellite and ground observations, Journal of Geophysical Research: Atmospheres, 2013JD020654, doi:10.1002/jgrd.50835.

Zhang, X. Y., Wang, Y. Q., Niu, T., Zhang, X. C., Gong, S. L., Zhang, Y. M., and Sun, J. Y.: Atmospheric aerosol compositions in China: spatial/temporal variability, chemical signature, regional haze distribution and comparisons with global aerosols, Atmos. Chem. Phys., 12, 779-799, doi:10.5194/acp-12-779-2012, 2012.

Chapter 3

Latitudinally asymmetric response of global surface temperature: Implications for regional climate change

Abstract

The Earth's climate system was subject to two multi-decadal warming trends in the beginning (1910–1940) and end (1975–2005) of the 20th century, having been interrupted only by a cooling trend in mid-century (1940–1975). The spatial-temporal distribution of surface temperature during this time, especially the land-ocean warming contrast in recent decades, has been the subject of many climate change detection studies. The focus of this study is the south-to-north warming asymmetry and we observed a similar Latitudinal Asymmetry of Temperature Change (LATC) for the two warming sub-periods and the cooling sub-period. Basically, the temperature change was low in the Southern Hemisphere extra-tropics (60˚S) and increased monotonically to peak values (0.15 ˚C/decade for warming trends) in the Northern Hemisphere extra-tropics (60˚N). We hypothesized that the LATC is a fundamental characteristic of the planet's transient response to global forcing. We tested this hypothesis using climate model simulations of CO_2 and aerosol forcing, and the simulations revealed very similar LATC as seen in the observations. In the simulations, the LATC did not depend on the asymmetry of the forcing and furthermore weakened significantly in equilibrium simulations, leading to the

deduction that the LATC was caused by a North-South asymmetry in the land-ocean fraction, i.e., the analyses of model simulations supported the hypothesis of LATC being a fundamental characteristic of the planet's transient response. If LATC is preserved as the planet warms beyond 2 ˚C, precipitation patterns can be drastically disrupted in the tropics and sub-tropics, with major implications for regional climate.

3.1 Introduction

3.1.1 Factors governing latitudinal and regional patterns of temperature changes

Predictions of climate change phenomenon at regional level are important for assessing the societal impacts of climate change (e.g. see Chapter 14 of IPCC-AR5). In order to deepen our understanding of regional climate and improve future predictions, we need to better understand the global surface temperature patterns during the last century, since it was subject to both natural and anthropogenic influences. The pattern of temperature change due to anthropogenic forcing is controlled by two factors: Radiative forcing due to changing atmospheric composition and internal processes such as land-ocean asymmetry and ocean-atmosphere dynamics. Our objective in this chapter is to understand the relative importance of the two.

The first is the anthropogenic forcing imposed on the climate system. Greenhouse gases (e.g. CO_2) and aerosols (including warming aerosols of BC and cooling aerosols of sulfate etc.) contribute most of the external forcing. GHGs like CO_2 and methane have relatively long lifetimes and therefore homogeneous spatial distribution of forcing. On the other hand, the forcing pattern of aerosols on a regional scale can be highly

inhomogeneous, creating a regionally concentrated perturbation of energy balance. In Chapter 2, we have discussed the magnitude and distribution of BC forcing over Asia region by constraining the global climate model simulations with observations.

In Figure 3.1, we showed the zonal average of TOA forcing due to BC, CO_2 and sulfate simulated by a global climate model (see Chapter 4 for the details of simulation). BC has the highest concentration close to its sources and thus its forcing has a non-uniform forcing pattern with much higher forcing value over the north hemisphere (Figure 3.1). Similarly, sulfate forcing that origins primarily from industrial sources also concentrates more over Northern Hemisphere. On the contrary, the CO_2 forcing shows little hemispheric asymmetry but amplifications in the warmer tropical regions.

The second factor in determining temperature response pattern is the land-ocean contrast as an inherent characteristic of the climate system, which we refer to as an internal process, as opposed to the anthropogenic forcing imposed by human activities. For example, the East Asia climate is regulated by the contrast of Euro-Asia continent and western Pacific Ocean and the associated monsoon system. The fundamental question we are trying to address in this Chapter 3 is to what extent the pattern of temperature response; in particular, the north-south asymmetry is determined by climate system itself.

We first re-visit earlier studies on observed temperature change pattern and move on to look at the various model simulation of temperature change under different forcing. The implication of large-scale temperature pattern on regional rainfall distribution is demonstrated with idealized GCM simulations.

3.1.2 Previous studies on large-scale pattern of surface temperature change

As an important indicator of climate change, changes in global surface temperature during the 20th century have been studied extensively (Trenberth et al., 2007). Some of the earliest detection methods for and signals attributed to global warming began in the 1980s (Madden and Ramanathan, 1980), and these gave way to further numerous sophisticated attempts to detect and measure climate changes (Santer et al., 2009). The focus now is on determining higher order moments–spatial and temporal asymmetries of the warming trend. Numerous studies in which the land-ocean contrast has been examined have clearly established that land-surface warming is larger than the warming of the sea, especially during the rapid warming sub-period prior to the 1970s (Braganza et al., 2003; Sutton et al., 2007; Trenberth et al., 2007; Joshi et al., 2008; Lambert et al., 2011; Drost et al., 2011). Models are able to simulate this contrast but the contrast shows up both in transient simulations and equilibrium simulations, leading to the conclusion that the larger warming over land is due to surface-atmosphere feedbacks (Sutton et al., 2007; Joshi et al., 2008).

Two other spatial asymmetries examined considered the difference in warming trends between the Northern Hemisphere (NH), Southern Hemisphere (SH) (e.g., Braganza et al., 2003), and latitudinal gradient of the warming within the NH (Gitelman et al., 1997). Many studies have shown that the NH warming is much larger than that in the SH (e.g., Drost et al., 2011). Furthermore, within the NH, polar latitudes had larger warming than the lower latitudes, thus weakening the latitudinal temperature gradient

(Drost et al., 2011) within the NH. In order to factor in all above-mentioned asymmetries in the warming trend, Drost et al. (2011) proposed six indices that included global mean temperature as well as the difference in land-ocean and NH-SH warmings. In summary, past work has well established that the NH latitudinal temperature gradient is weakening, and there is asymmetry in the warming trend between the NH and the SH. From attempts to understand this asymmetry using model simulations (Braganza et al., 2003; Stott et al., 2006; Drost et al., 2011) it is inferred that the NH-SH asymmetric trend is indicative of anthropogenic influences in the global mean trend.

This study, which was built on earlier studies, identifies a new metric for the NH-SH asymmetry in terms of a normalized latitudinal temperature gradient. Also included is a detailed analysis of the underlying causal factor for the asymmetry. Our study of 20th century trends of latitudinal temperature gradients also differentiates from earlier studies in the following ways: a) We considered trends from 60˚S to 60˚N and not only in the NH. Earlier studies (Gitelman et al., 1997; Braganza et al., 2003; Drost et al., 2011) were limited to 50–55˚N and 30–35˚N. b) Whereas earlier studies focused on century time scale trends, we divided the 20th century into three sub-periods: early warming sub-period from 1910 to 1940, middle cooling sub-period from 1940 to 1975, and late warming sub-period from 1975 to 2005. This new approach enabled us to identify a characteristic pattern of asymmetry in the latitudinal temperature trend that is similar for all three sub-periods, in spite of the significant differences in the global mean trends between the three sub-periods (analysis presented in next section). Based on the empirical data, we hypothesized that this characteristic pattern of asymmetry is caused by the corresponding latitudinal asymmetry in the land-ocean fraction. We tested this hypothesis

with available 3-D climate model simulations. In the final section, we explored the implication of asymmetric trends for regional precipitation changes.

3.2 Surface temperature change in the 20th century: latitudinal asymmetry

Before examining latitudinal asymmetry, we first revisit the pattern of global and hemispherical mean temperature trends from the gridded temperature record compiled by the Goddard Institute for Space Studies (Hansen et al., 2010). Revisiting this issue was necessary because other published studies dealt largely with the 20th century as a whole or only the last half of the century. Here, we considered three sub-periods based on the NH experiencing a 0.48 ± 0.13 ˚C (95% confidence interval) warming during the first three decades ending in the 1940s, then shifting to a cooling of -0.24 ± 0.12 ˚C from 1940 to 1975, which was followed by a large warming of 0.8 ± 0.16 ˚C from 1975 to 2005 (Figure 3.2a). The SH did not demonstrate a statistically significant mid-century cooling (Figure 3.2a), and the 1975–2005 warming was only 0.3 ± 0.11 ˚C lower than the NH trend by a factor of 2.5. The hemispherical and global mean values in Fig. S1 and Table S1 show the entire trend analyses for reference. Another well-known feature from earlier studies highlights the trend's land-ocean contrast (Figure 3.2b). Multi-decadal trends were more pronounced over the land surface, with warming of 0.38 ± 0.15 ˚C, cooling of -0.16 ± 0.14 ˚C, and then warming of 0.82 ± 0.2 ˚C, respectively, during the three sub-periods. In contrast, the ocean surface experienced two smaller warming (0.3 ˚C and 0.38 ˚C) trends in the beginning and end of the century, while the mid-century trend was not significant (-0.05 ± 0.1 ˚C). Analyses separating the NH mean temperature into a land

and ocean component (Fig. S1) show that the NH land experienced larger trends compared with the NH ocean (e.g., two times the larger warming during the last sub-period), making it the strongest contributor to the warming-cooling-warming pattern observed in global average temperature trends. As to the underlying message, a time-series analysis of 20th century surface temperatures must account for multi-decadal changes in the sign and magnitude of the trends. The analysis above was performed with data from 60˚S to 60˚N, excluding Polar Regions. We limited the analysis to this latitude band because it avoids the less reliable observations from the Arctic regions (Chylek et al., 2009), particularly for the 1910–1940 sub-period (e.g., see Gitelman et al., 1997). In addition, the Antarctic continent's higher elevation makes it difficult to estimate a gradient in surface temperature from sea level to the elevated continent. However, we found that the main features of the hemispheric multi-decadal variations also appear if analysis is carried out with temperature data from 90˚S to 90˚N (Fig. S1).

We determined temperature trends separately as a function of latitude for the three sub-periods. Focusing first on the two sub-periods subject to strong warming (1910–1940 and 1975–2005), the trends over the ocean were relatively small in the SH extra-tropics (Figure 3.3a) and increased northward with a maximum of about 0.25–0.35 ˚C /decade in the NH extra-tropics. The mid-century cooling sub-period also showed a similar pattern of maximum change in the NH extra-tropics. We illustrated the latitudinal gradient of oceanic temperature trends in Figure 3.3b (slope of linear fits). It should be noted that, to better display the similarity in the latitudinal asymmetry, the trend in 1940–1975 (negative) was reversed in sign and adjusted with an offset of 0.1 ˚C. This offset does not affect the asymmetric feature or the latitudinal gradient. The trend's latitudinal gradient

for 1940–1975 (blue curve) is 0.0012 ˚C /decade/degree (95% confidence interval ranging from 0.0009 to 0.0016, as shown by color shading). The other two linear fits (0.0009 for 1910–1940 and 0.0018 for 1975–2005) are nearly within the 95% confidence interval. The factor-of-two difference in the gradient between the two warming sub-periods reduced to a factor of about 1.5 when the trends were normalized with the respective global mean (60˚S to 60˚N) warming trends (Figure 3.3c). Normalized trends are also compared in the next section due to large differences in trends between observations and various simulations.

In summary, irrespective of the differences in the magnitudes and signs of the three observed trends, their latitudinal asymmetries were statistically similar. Thus, the asymmetry of temperature trends (see Fig. S2 for land) is possibly a fundamental characteristic of the response of the climate system to global forcing.

3.3 Understanding latitudinal asymmetry

The fundamental causal factors for similarity in the latitudinal asymmetry of temperature trends for the three sub-periods are explored using simulations from a Global Climate Model (GCM) developed at the Geophysical Fluid Dynamics Laboratory (GFDL-CM2.1 (Delworth et al., 2006)). The 20th century simulation output was used to calculate trends for the three sub-periods following our approach for the observational record. The 20th century simulation adopted time-varying anthropogenic greenhouse gases and aerosol forcing, as well as changes in natural forcing such as incident solar radiation and volcanic aerosols. Trends simulated by the model (Fig. S3a) were generally consistent with observed trends (Figure 3.3a). The asymmetry of the normalized trend for

the last sub-period had a gradient of 0.019 (0.015–0.024) deg^{-1} (Figure 3.3d) and was consistent with the observed asymmetry of 0.015 (0.012–0.018) (Figure 3.3c). One confounding issue with the 20th century simulation was the inclusion of aerosol forcing, which had strong inter-hemispheric asymmetry and, thus, could influence temperature trend asymmetry. To eliminate this possibility, we redid the analysis with the GFDL-CM2.1 output for the so-called CO_2-doubling simulation. For this simulation, the CO_2 concentration was initiated at 280 ppm for year 1 and was increased 1% per year until it reached 560 ppm at year 70. The CO_2 concentration was fixed at 560 ppm, and the model continued to run for another 180 years. The temperature change during the transient phase (defined as $2CO_2t$) was calculated for year 15–45 by comparison with another control simulation in which the CO_2 concentration was fixed at 280 ppm. The normalized temperature increase for the transient phase yet again demonstrated a pattern of south-to-north asymmetry that was similar to that for the 20th century simulation (Figure 3.3d). The analyses were repeated with output from the MPI GCM (ECHAM5/MPI-OM) (Jungclaus et al., 2006). Even though the MPI model yielded a different absolute value of temperature trends for the three sub-periods, the south-to-north asymmetry pattern was similar (Fig. S4). Note that the two GCM simulations from GFDL and MPI utilized different CO_2 and aerosol forcings for the 20th century simulation, but the CO_2-doubling simulation used only CO_2 forcing. Despite diverse forcing magnitudes, latitudinal asymmetry in the temperature response was preserved in both models. The fundamental inference was the asymmetry pattern of normalized temperature trend with a gradient of 0.015–0.019 $degree^{-1}$, which was a model-independent characteristic.

From these model simulations, we concluded that the observed latitudinal

asymmetry was independent of the asymmetry from forcing; hence, forcing was not a causal factor for the asymmetry. The logical deduction is that the asymmetry was due to a corresponding latitudinal asymmetry in the landmass fraction, which increased monotonically from 0% at 60˚S to 70% at 60˚N (Figure 3.3d). Why then did the latitude band with the larger land fraction exhibit larger temperature trends? Studies have shown two potential contributing factors to the larger warming seen over land compared to that over the ocean at the same latitude (Lambert et al., 2011). First, the ocean has a much larger heat capacity than does land. Second, a model has shown (Sutton et al., 2007) that in response to the same forcing, equilibrium temperature changes over land are larger than those over the ocean due to stronger negative evaporation feedbacks over the sea surface (Manabe et al., 1991). Because of the climate system's fixed land-ocean area, the cumulative effect of the land-ocean warming contrast was mapped onto a pattern of south-to-north asymmetry in temperature trends, both over land and over the ocean. The analysis was also extended to include the Arctic region up to 90˚N in Fig. S5, and the same asymmetric feature is reproduced. However, we note that the amplified warming over the Arctic was potentially contributed from sea ice feedback mechanism, which is beyond the scope of our discussion.

One way to verify the above conclusion was to examine temperature changes for the equilibrium state, which should exhibit a weaker asymmetry because the factor dealing with the ocean's heat capacity would not play a role. The temperature change in a quasi-equilibrium state ($2CO_2e$, year 190–220, 120 years after CO_2 was doubled) was calculated by comparison to a control simulation (280 ppm CO_2 fixed). As shown in Fig. S3c (see $2CO_2e$), the asymmetry is less than 0.008 deg^{-1} compared with 0.019 deg^{-1} for

the transient case ($2CO_2$t curve). The asymmetry did not completely diminish because (1) 120 years is not long enough for the coupled ocean-atmosphere system to reach a true equilibrium state, and (2) even if equilibrium was reached, for the same forcing, the warming over land is larger than that of the ocean due to less climate sensitivity over the ocean.

Our finding that the latitudinal asymmetry is governed by latitudinal variations in land and ocean fraction is intuitive and could have been inferred from earlier studies (e.g. Drost et al., 2011). Yet our study is unique in demonstrating this fundamental feature of transient warming and in using a combination of observations and model simulations to establish its causal factor. In particular, (1) by subdividing the 20th century trend into three sub-periods, we have shown that the asymmetric response is statistically similar for all periods (Figure 3.3b) irrespective of the forcing being different and the global mean trend being different in both magnitude and sign. This near similarity provides compelling proof that the latitudinal gradient is a fundamental characteristic of the climate system response to global forcing. (2) By comparing the latitudinal gradient ($0.015\ deg^{-1}$) of the normalized temperature trend in the last sub-period from observing (Figure 3.3c) model simulations of the 20th century (with aerosol + CO_2 forcing) and with CO_2 forcing only (Figure 3.3d), we have shown that the simulated gradient of $0.019\ deg^{-1}$ not only compares well with the observed value of $0.015\ deg^{-1}$ but is also independent of the spatial patterns of the forcing. (3) Finally, the gradient of normalized temperature trend decreased significantly from $0.019\ deg^{-1}$ in CO_2 -doubling transient simulations to less than $0.008\ deg^{-1}$ in equilibrium simulations. This factor-of-two decrease in the gradient further confirmed that asymmetry in the normalized temperature

trends was driven by corresponding asymmetry in the land-ocean fraction.

3.4 Implications for regional climate changes: present and future

The latitudinal asymmetry of temperature response is likely to be a zeroth-order approximation of global warming spatial pattern in the 21st century. An important consequence is the potential impact on regional precipitation response, a topic receiving increasing attention (Held et al., 2005; Chung and Ramanathan, 2006; Xie et al., 2010; Vecchi et al., 2011). We conducted idealized GCM experiments with a zonally uniform SST latitudinal gradient to illustrate the impact of latitudinal asymmetry of ocean warming. We used the National Center for Atmospheric Research (NCAR) CESM1.0 model (Gent et al., 2011) to simulate a global climate response to two distinctly different patterns of sea surface temperature (SST) increases from a climatological SST pattern. The first imposed a uniform SST increase of 0.3 ˚C everywhere in the model domain (SST_Uniform). The second imposed a linear gradient of SST increase (SST_Grd) ranging from 0 ˚C at 60˚S to 0.6 ˚C at 60˚N with a global mean increase of 0.3 ˚C to mimic the observed trends during 1975–2005. The control run prescribed observed sea surface temperature (SST_control). CESM simulations were run for 35 years in a resolution of 2.8˚ x 2.8˚. The first 5 years was for spinning up, and the remaining 30 years enabled us to obtain a statistically significant long-term temperature and precipitation average. The simulated precipitation changes in the asymmetric SST warming experiment (SST_Grd, Figure 3.4b) showed an increase in northern tropical precipitation. A particularly strong precipitation increase (20%) over the Northern Indian

Ocean illustrated the strong sensitivity of the Indian monsoon to changes in the SST gradient (Chung and Ramanathan, 2006), which was also seen in the observed trend. Simulated precipitation over many parts of the Southern tropics and Western North America decreased by about 10%, and these features were also seen in the observed trend. However, the observed negative trend was much stronger. A one-to-one comparison across the globe was not warranted, since the simulation ignored the important effects of aerosol forcing on regional precipitation (Rotstayn et al. 2002) and the detailed spatial pattern of SST change over past decades.

One major implication of these results is that the planet's future transient warming will continue to be subject to the south-to-north asymmetry (Figure 3.3d), meaning the impact of the asymmetric response is likely to grow with time. Even if CO_2 concentration is stabilized at current levels, the committed warming due to current GHG forcing (Wigley, 2005; Ramanathan and Feng, 2008) would be as much as 2.5 ˚C compared with preindustrial era. To explore the implications of a larger warming accompanied by the asymmetric pattern, we performed another model simulation (SST_GrdLarge) in which the imposed warming had a south-to-north asymmetry similar to the gradient in Figure 3.3b but with a global mean sea surface warming of 2.5 ˚C. Results showed a similar pattern to that from the SST_Grd simulation but the change was larger in magnitude by a factor of 5–10 (Figure 3.4c). Africa, Western North America, the Amazon region of South America, and Australia were subject to intense droughts of up to a 50% decline in precipitation. The droughts simulated in these regions were accompanied by a large increase (50%) in Indian monsoon rainfall. Shifts in regional precipitation patterns shown in Figure 3.4c would pose enormous challenges for the ecosystem and the populations

living in the tropical and sub-tropical regions. Since the models (at least the ones used in this study) accounted for latitudinal asymmetry, in principle, their simulations for the 21st century should simulate the large precipitation shifts shown in Figure 3.4c. However, given the enormous difficulty in interpreting model results, findings here can guide the interpretation of model simulations for the future.

Acknowledgments

The text of Chapter 3, in full except the Section 3.3.1 and Figure 3.1, is a reprint of a published paper entitled “Latitudinally asymmetric response of global surface temperature: Implications for regional climate change” in July 2012 issue of Geophysical Research Letters. The dissertation author was the primary researcher and author of this paper. Co-author on this paper is V. Ramanathan.

We thank the two anonymous reviewers for their insightful comments on the paper, which immensely helped in improving the clarity of the presentation. The study was supported by the National Science Foundation (ATM07-21142). We also acknowledge NCAR’s Computational and Information Systems Laboratory for providing computing resources.

Figures

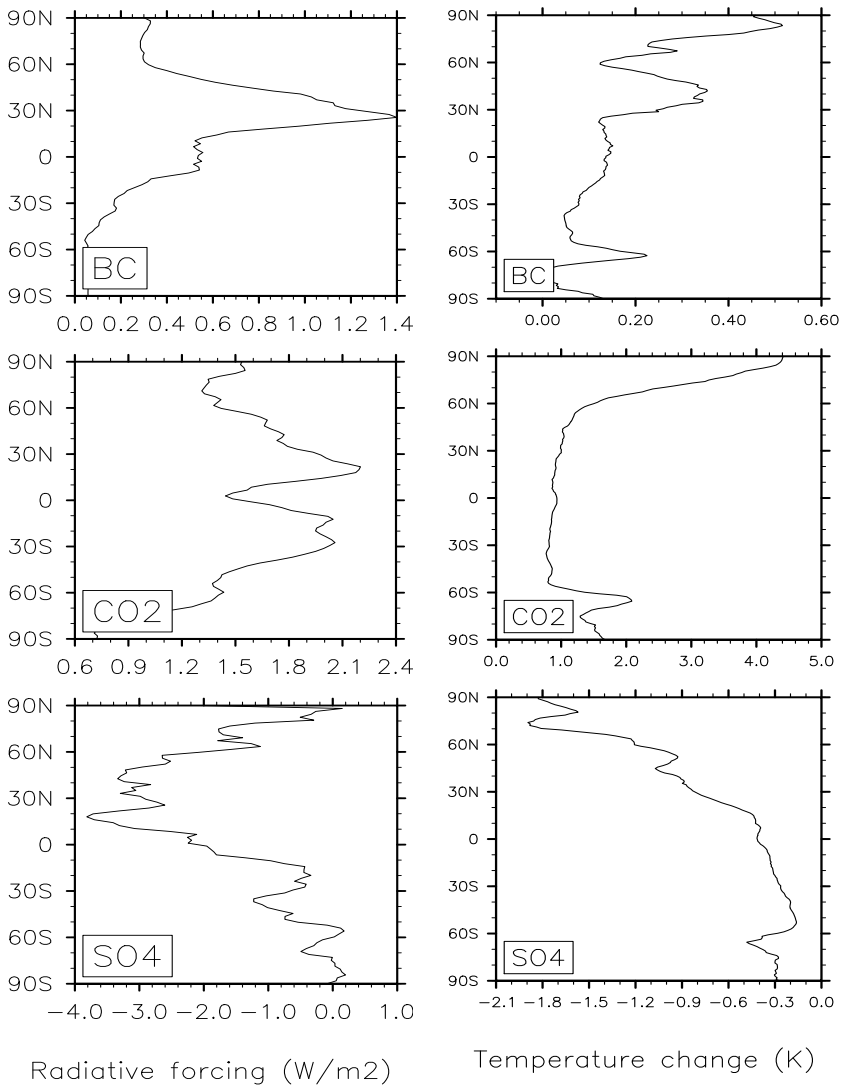

Figure 3.1 (Left) zonal average of radiative forcing (W/m^2) of BC (direct only, shortwave), CO_2 (longwave) and SO_4 (direct+indirect, shortwave). The forcing is calculated by running atmospheric model for 6 years. (Right) zonal mean of Surface temperature change (C) in response to different forcings shown in (Left). Surface temperature change is calculated from a 60-year average of coupled model simulation, and is effectively the model response at the year 45 after the forcing is applied. The details of the simulations are provided in Chapter 4. Note that the global and hemispheric mean of radiative forcing and temperature response is shown in Table 4.2 of Chapter 4.

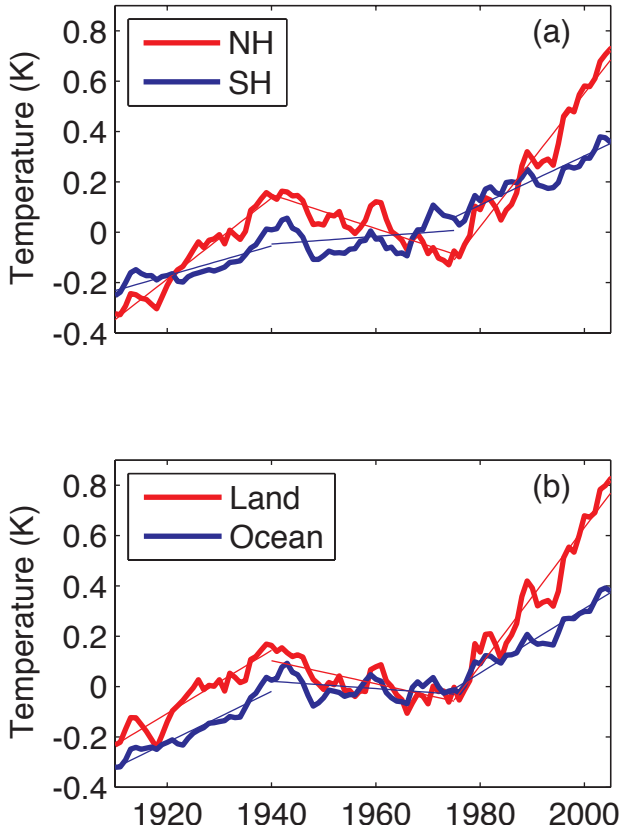

Figure 3.2 Observed temperature changes (1910–2005) for (a) NH and SH and (b) land and ocean. Temperature is shown as an anomaly relative to the base period 1951–1980. Linear fits of temperature trends (thin lines) made for the three sub-periods illustrate multi-decadal temperature variations (1910–1940, 1940–1975, 1975–2005). The sub-period intervals were chosen based on multi-decadal global mean trends (Trenberth et al., 1990). Using this approach also avoided incorporating years containing questionable measurements (Thompson et al., 2008; Thompson et al., 2010) as starting or ending points.

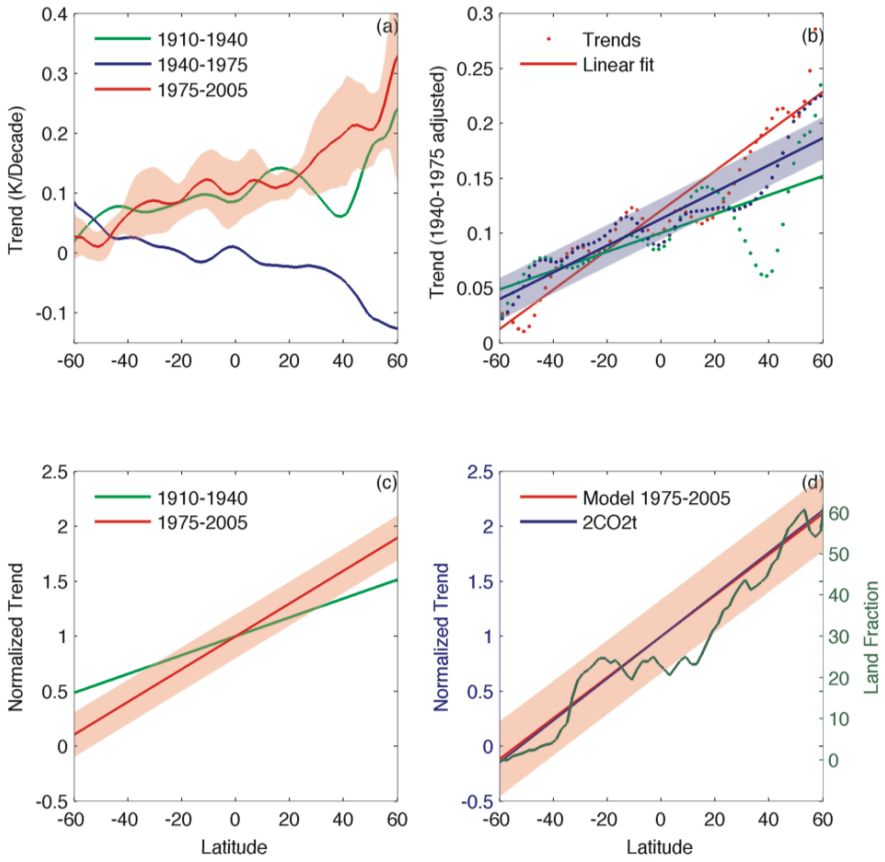

Figure 3.3 Latitudinal asymmetry of temperature trends for the ocean. (a) Warming trends (˚C/decade) of surface ocean temperature for the three sub-periods of the 20th century, as a function of latitude (60˚S–60˚N). Trends were calculated based on a linear fit method shown in Figure 3.2. Uncertainty in the warming trend for one sub-period is shown in shading area. (b) Temperature trends (color dots) are the same as for (a), except the 1940–1975 trends were reversed in sign and adjusted with 0.1 ˚C. The latitudinal gradient is shown with linear fits (solid lines). Uncertainty of linear fits is shown in shaded color. (c) Latitudinal gradients of normalized trends (relative to global average) for 1910–1940 and 1975–2005 warming sub-periods. (d) Latitudinal gradient of normalized trends (relative to global average) in the GFDL model resulted under two different simulations (1975–2005 in the 20th century simulation, CO_2 -doubling transient simulation or $2CO_2t$). Surface temperatures from GFDL and MPI model outputs were obtained from the World Climate Research Program's Coupled Model Inter-comparison Project phase 3 (CMIP3) multi-model dataset (Meehl et al., 2007). Temperature change for the transient phase (year 10–40) and for the quasi-equilibrium phase (year 190–220) were calculated by differencing a 30-year average temperature with the average temperature in the corresponding sub-periods from a control simulation.

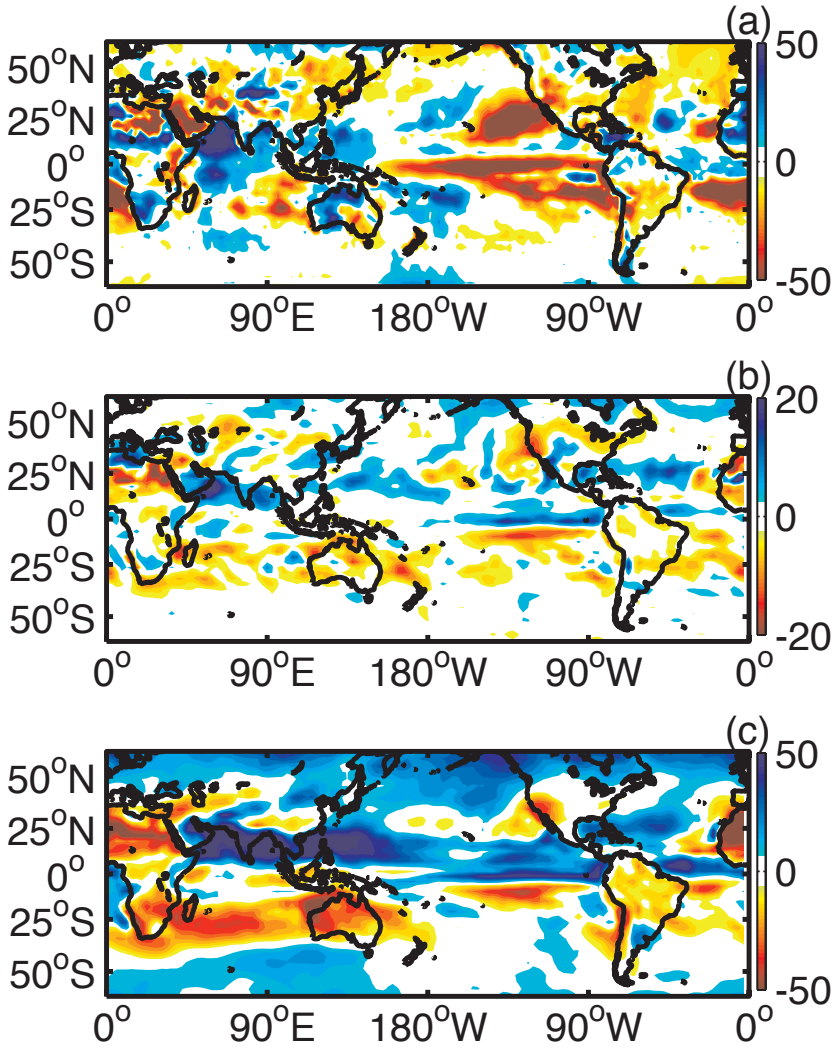

Figure 3.4 Precipitation rate changes (%). (a) 1979–2009 observations. The absolute precipitation change was determined from linear fits of a 30-year long time-series at each grid. The percentage of change was the absolute change divided by the long-term mean. (b) Simulated changes in the experiment (SST_Grd) in which the SST gradient was imposed with global mean increase of 0.3 ˚C. (c) Simulated changes in the experiment (SST_GrdLarge) in which SST gradient was imposed with global mean increase of 2.5 ˚C. The percentage of simulated change was determined by comparison with a control experiment incorporating climatologic SST. Areas with small changes were considered statistically insignificant and thus left white. Observed precipitation was obtained from Global Precipitation Climatology Project (GPCP version 2.1; Adler et al., 2003). Precipitation trends were calculated using the method adopted for temperature observation.

Supplementary Table

Table S1. Land and ocean temperature changes (˚C) in each hemisphere during the three sub-periods of the 20th century. The changes are calculated from linear estimation method shown in Figure 3.2. 95% confidence interval of linear estimation is shown in brackets.

		1910-1940	1940-1975	1975-2005
Land+Ocean	Globe	0.33[0.24, 0.42]	-0.09[-0.19, 0.01]	0.54[0.42, 0.67]
	NH	0.48[0.35, 0.61]	-0.24[-0.36, -0.11]	0.79[0.63, 0.96]
	SH	0.18[0.1, 0.25]	0.05[-0.06, 0.16]	0.29[0.18, 0.4]
Land	Globe	0.38[0.23, 0.52]	-0.16[-0.3, -0.02]	0.82[0.62, 1.03]
	NH	0.51[0.33,0.7]	-0.27[-0.46, -0.09]	1.02[0.78, 1.26]
	SH	0.10[-0.01, 0.21]	0.06[-0.08, 0.2]	0.43[0.22, 0.64]
Ocean	Globe	0.30[0.23, 0.38]	-0.05[-0.15, 0.05]	0.38[0.29, 0.47]
	NH	0.45[0.35, 0.55]	-0.20[-0.32, -0.08]	0.58[0.46, 0.69]
	SH	0.20[0.13, 0.28]	0.05[-0.06, 0.16]	0.25[0.16, 0.34]

Supplementary Figures

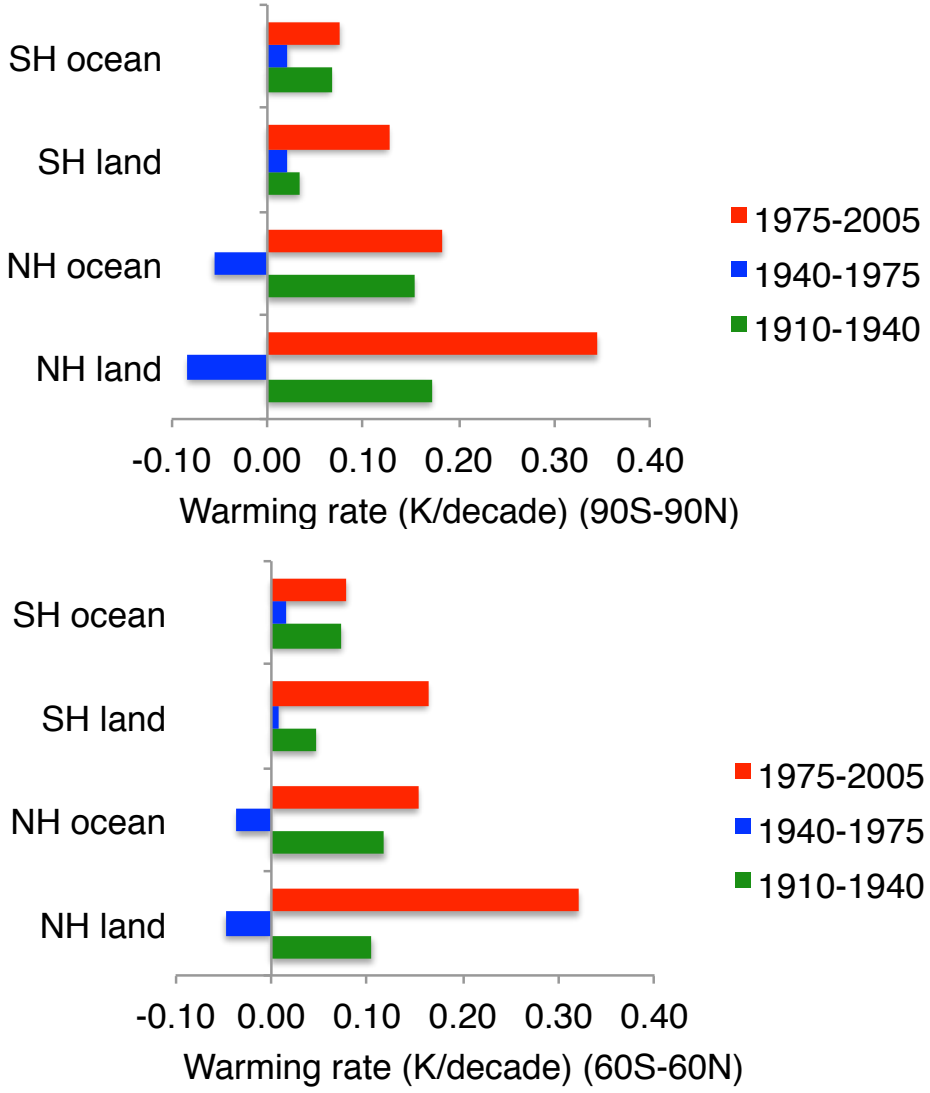

Fig. S1. Warming rates (˚C/decade) for different sub-periods of the 20th century. (a) Calculated with data in 90˚S–90˚N. (b) Same as (a) but data used only in 60˚S–60˚N.

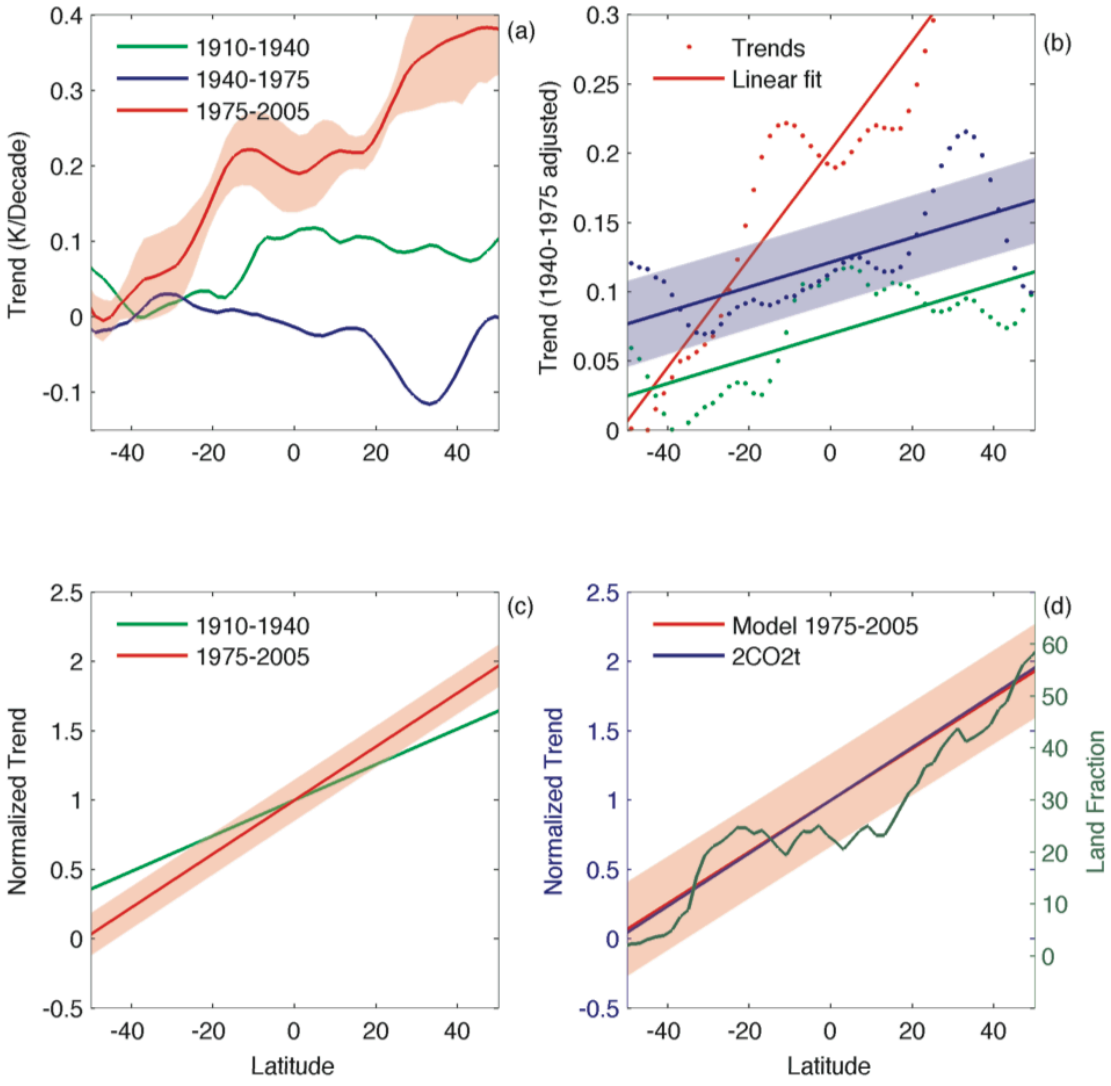

Fig. S2. Same as Figure 3.3 but with land temperature data.

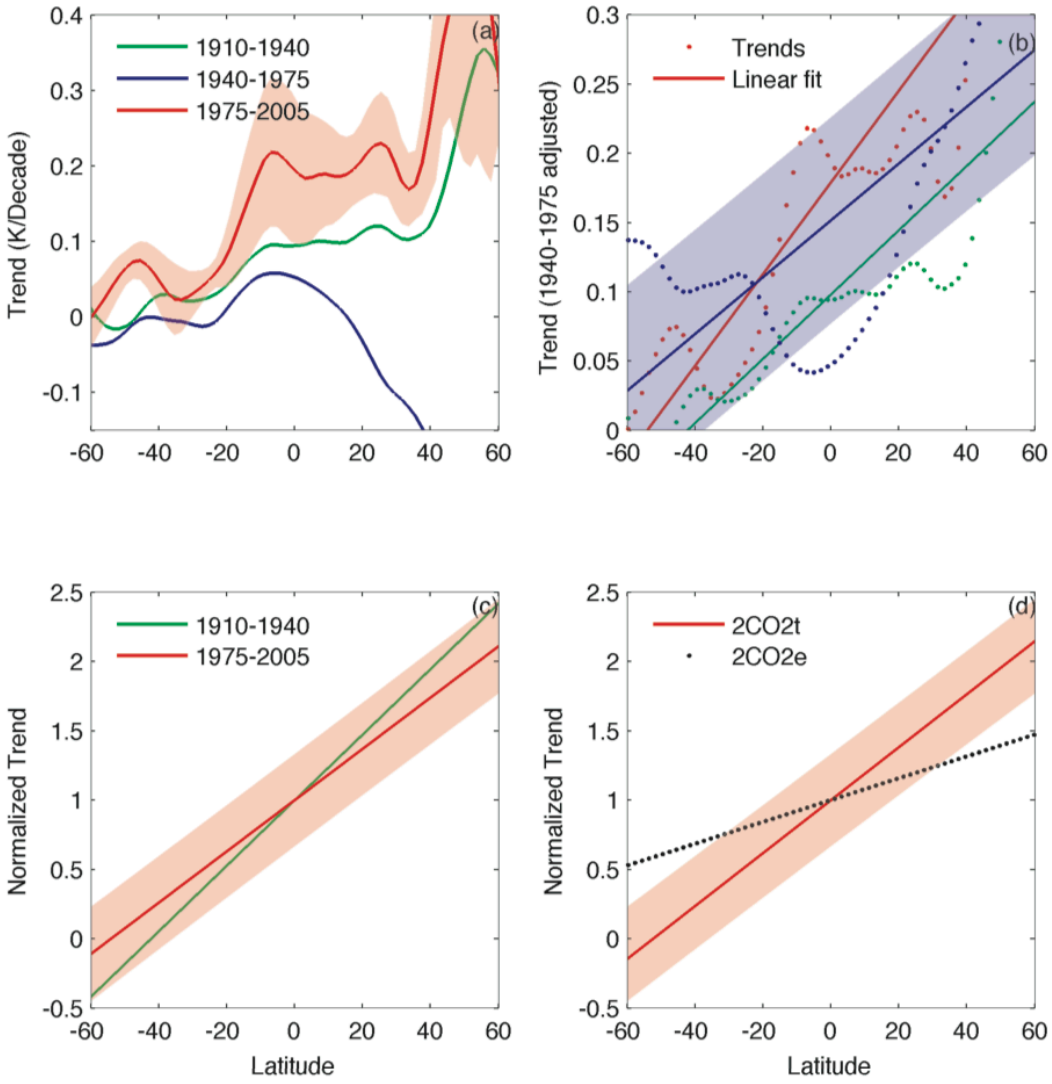

Fig. S3. Same as Figure 3.3, but observation data are replaced with the 20th century simulation of GFDL model. In (d), both transient and equilibrium cases (GFDL model CO_2 -doubling simulation) are shown.

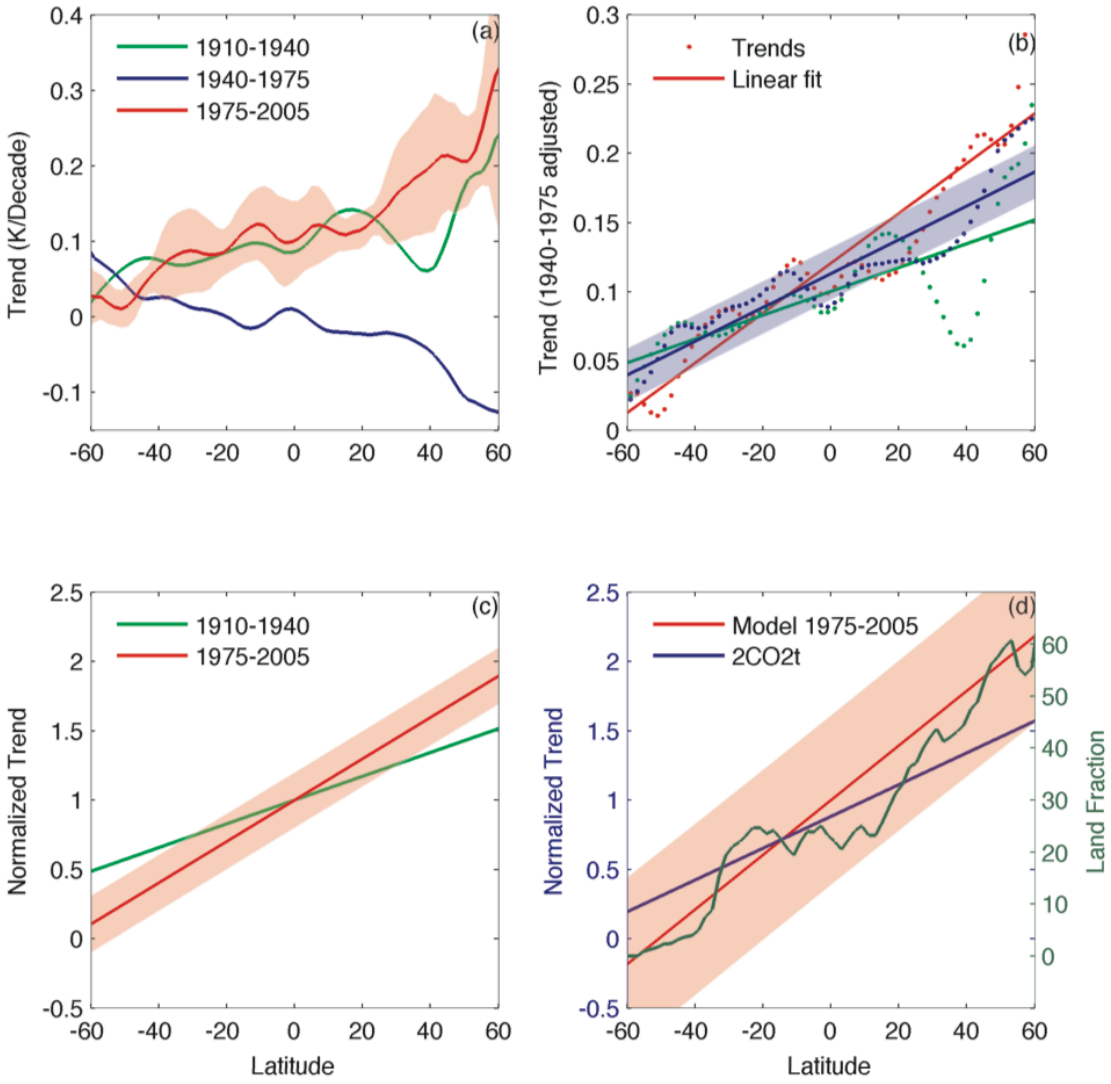

Fig. S4. Same as Figure 3.3, but model data originate from MPI corresponding simulations.

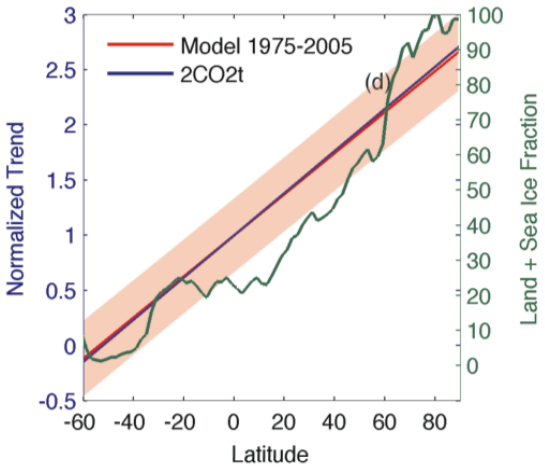

Fig. S5. Same as Figure 3.3d but extended to include Arctic regions. Ocean heat capacity, when covered by sea ice has very little heat capacity like land surface, so the land fraction shown here also includes sea ice fraction and hence Arctic ocean over the North Pole (which is covered with ice throughout the year) is shown as having 100% land fraction.

References

Adler, R.F. et al. (2003), The Version-2 Global Precipitation Climatology Project (GPCP) Monthly Precipitation Analysis (1979–Present). Journal of Hydrometeorology 4, 1147-1167.

Braganza et al., (2003), Simple indices of global climate variability and change: Part I - variability and correlation structure, Climate Dynamics 20, 491-502.

Chung, C.E. and Ramanathan, V. (2006), Weakening of North Indian SST Gradients and the Monsoon Rainfall in India and the Sahel. Journal of Climate 19, 2036-2045.

Chylek, P. et al. (2009), Arctic air temperature change amplification and the Atlantic Multidecadal Oscillation. Geophysical Research Letters 36.

Delworth, T.L. et al. (2006), GFDL's CM2 global coupled climate models. Part I: formulation and simulation characteristics. Journal of Climate 19, 643-674.

Drost et al., (2011), Communicating global climate change using simple indices: an update, Climate Dynamics, DOI 10.1007/s00382-011-1227-6.

Gent, Peter R., et al., (2011), The Community Climate System Model Version 4. J. Climate, 24, 4973–4991.

Gitelman A, Risbey J, Kass R, Rosen R (1997) Trends in the surface meridional temperature gradient. Geophys Res Lett 24:1243–1246.

Hansen, J. et al. (2010), Global surface temperature change. Reviews of Geophysics 48, 1-29.

Held, I.M. et al. (2005), Simulation of Sahel drought in the 20th and 21st centuries. Proceedings of the National Academy of Sciences of the United States of America 102, 17891-6.

Joshi M.M., et al., (2008), Mechanisms for the land/sea warming contrast exhibited by simulations of climate change. Clim Dyn 30(5):455–465.

Jungclaus, J.H et al. (2006), Ocean Circulation and Tropical Variability in the Coupled Model ECHAM5/MPI-OM. Journal of Climate 19, 3952.

Lambert, F.H., Webb, M.J. & Joshi, M.M. (2011), The Relationship between Land–Ocean Surface Temperature Contrast and Radiative Forcing. Journal of Climate 24, 3239-3256.

Madden, R.A. and Ramanathan, V. (1980), Detecting Climate Change Due to Increasing CO_2 in the Atmosphere. Science 209, 763-768.

Manabe, S. et al. (1991), Transient responses of a coupled ocean-atmosphere model to gradual changes of atmospheric CO_2. Journal of Climate 4, 785-818.

Meehl, G. et al. (2007) THE WCRP CMIP3 Multimodel Dataset: A New Era in Climate Change Research. Bulletin of the American Meteorological Society 88, 1383.

Ramanathan, V. & Feng, Y. (2008), On avoiding dangerous anthropogenic interference with the climate system: formidable challenges ahead. Proceedings of the National Academy of Sciences of the United States of America 105, 14245-50.

Rotstayn, L.D. & Lohmann, U. (2002), Tropical Rainfall Trends and the Indirect Aerosol Effect. Journal of Climate 15, 2103-2116.

Santer, B.D. et al. (2009), Incorporating model quality information in climate change detection and attribution studies. Proceedings of the National Academy of Sciences of the United States of America 106, 14778-83.

Stott, P. et al. (2006), Observational Constraints on Past Attributable Warming and Predictions of Future Global Warming. Journal of Climate 19, 3055-3069.

Sutton, R.T., Dong, B. & Gregory, J.M. (2007), Land/sea warming ratio in response to climate change: IPCC AR4 model results and comparison with observations. Geophysical Research Letters 34, 2701.

Trenberth, K.E. (1990), Recent observed interdecadal climate changes in the Northern Hemisphere. Bull. Amer. Meteor. Soc 71, 988–993.

Trenberth, K.E. et al. (2007), Observations: Surface and Atmospheric Climate Change. In: Climate Change 2007: The Physical Science Basis. Contribution of Working Group I to the Fourth Assessment Report of the Intergovernmental Panel on Climate Change [Solomon, S. et al (eds.)]. Cambridge University Press, Cambridge, United Kingdom and New York, NY, USA.

Thompson, D.W.J. et al. (2008), A large discontinuity in the mid-twentieth century in observed global-mean surface temperature. Nature 453, 646-649.

Thompson, D.W.J. et al. (2010), An abrupt drop in Northern Hemisphere sea surface temperature around 1970. Nature 467, 444-447.

Vecchi, G. et al. (2011), Statistical-Dynamical Predictions of Seasonal North Atlantic Hurricane Activity. Monthly Weather Review 139, 1070-1082.

Wigley, T.M.L. (2005), The climate change commitment. Science 307, 1766-9.

Xie, S.-P. et al. (2010), Global Warming Pattern Formation: Sea Surface Temperature and Rainfall. Journal of Climate 23, 966-986.

Chapter 4

Climate response to black carbon: with focus on high elevation warming and snow pack retreat in Tibet and Himalayas

Abstract

Himalayan mountain glaciers and the land snow over Tibet Plateau are the headwater of several major rivers in Asia, which provide vital fresh water resources for billions of people. Observations (in-situ measurement of snow depth and satellite measurement of surface albedo) suggest that the Himalayan mountain glaciers and Tibet snow cover have gradually retreated during the last few decades. The observations also revealed the vertical pattern of enhanced warming over high altitude regions.

The CESM1 model with improved representation of black carbon (BC) aerosols provides tools to study the climate system response to BC aerosols. Here we show that the global mean temperature increases by 0.2 to 0.3 °C following the pre-industrial to present-day BC emission change. The global mean precipitation change in response to BC is close to zero. BC aerosols emitted from both sides of the Himalayan Mountains play a vital role in causing the observed snow cover reduction. The surface warming at high elevation (around 1 to 1.5 °C at 5000 m) associated with the direct heating effect of BC and the BC deposition on the snow surface are both important physical processes in causing the snow reduction.

In the idealized simulations that mimic the contribution from the pre-industrial to present-day increase in BC emissions, the yearly averaged snow cover area over Tibet is reduced by more than 2% and the snow depth is reduced by at least 5% (0.2 cm). Surprisingly, compared to the response to BC, the reduction of Tibet snow in response to pre-industrial to present-day increase CO_2 concentration is only 1.5 times larger for snow cover fraction and only 60% for snow depth, despite that the global mean temperature response is 5 times larger.

Because of snow reduction, the surface albedo under all-sky conditions decreases by more than 5% along the Himalaya mountain range and nearly 1% over entire Tibet, therefore providing a positive local feedback mechanism to the warming. The effect on the hydrological cycle is the shifts of the river runoff to the beginning of the year, due to the largest reduction of snow observed during springtime.

4.1 Introduction

Rapid growth in economic activities and human population has caused intense air pollutions over Asian region. Among many air pollutants, black carbon aerosols have been shown to have significant impact for global and regional climate change (Ramanathan and Carmichael, 2008). In additional to causing global warming, many previous studies have linked Asia aerosols including sulfates and black carbon with monsoon system and have demonstrated the consequential implications of aerosols on summer rainfall and extreme precipitation events, and therefore the hydrological cycles (Ramanathan et al., 2005). Ramanathan et al., (2005) pointed out the absorbing aerosol emission contributes to the observed decrease in Southern Asia summer rainfall and

causes the increase in drought frequency. Meehl et al., (2008) showed with a global climate model that BC causes an enhanced precipitation over pre-monsoon months and decreased precipitation during summer monsoon. The changes of precipitation pattern and intensity over Asia region in response to black carbon aerosols have major impacts on the hydrological cycles and river systems.

Another important factor in determining river runoff and water supply is the cryosphere systems. In the Asian region, the major cryosphere are the Himalayan mountain glaciers and the adjacent land snow and ice over the vast Tibetan Plateau. Himalayan mountain glacier and snow pack have enormous impact on the water systems of major rivers and the people living nearby the rivers and the eco-system. The observations suggest a continuing decline in snow cover and Himalaya mountain glaciers, which has raised environmental concerns. Bajracharya et al., (2006) observed that the Himalayan glaciers are retreating at rates ranging from 10 to 60 m per year and many small glaciers disappeared. Gardner et al. (2013) also showed with satellite observations the steady reduction of Western China glaciers with the most rapid declined observed in Himalaya mountain regions.

The causes of such a steady change in the cryosphere on Tibet and Himalaya glacier and snowpack is still unclear. From an energy and water budget perspective, there are at least four controlling factors that can possibly influence the total mass of snow and ice over Tibet regions.

(1) Warming induced by greenhouse gases. Increased atmospheric CO_2 and other greenhouse gases (GHGs) are the major cause of global warming. Tibet regions also witness increasing surface temperature. One feature of the surface warming over Tibet is

that the warming trend increases significantly with altitude (Liu et al., 2009). In theory, the CO_2 -induced warming should also have altitude dependency due to moist convection.

(2) Monsoon precipitation change due to aerosols. By intercepting sunlight, black carbon and other cooling aerosols like sulfates both lead to large-scale surface dimming over Asia. The surface dimming can weaken reduces monsoon precipitation over South Asia and therefore reduce the supply of snow and ice to the glaciers and snowpack for two reasons: (a), dimming by aerosols over the ocean decreases evaporation, the source of moisture for the monsoon; and (b) the surface cooling due to the dimming is mainly concentrated over the northern Indian Ocean due to larger aerosol loading. The resulting weakening of the sea surface temperatures north to south has weakened the monsoon circulation.

(3) Atmospheric heating due to black carbon aerosols. Black carbon aerosols absorb significant amount of sunlight (as much as 25% measured by in-situ observations of unmanned aircrafts, Ramanathan et al., (2007)). Such anomalous heating in the atmospheric over the elevated regions will contribute to the loss of surface ice and snow in two different ways: 1) It will increase melting of the glaciers; 2) More of the precipitation will fall as rain instead of snow.

(4) Surface melting by black carbon deposition. Snow and ice surface has high surface albedo and reflects as much as 50% to 90% of incoming solar radiation. Black carbon aerosols are transported over the Himalayas and Tibet Plateau and removed from the atmospheric due to precipitation. When black carbon aerosols are deposited over the snow and ice, it increases the absorption of solar radiation and causes surface warming.

Regard to the third and fourth mechanism of BC impact on snow, recent studies

have also suggested that cryosphere is subject to the influence of black carbon aerosols over regions including the Alps (Painter et al., 2013) and Eurasia land snow cover (Flanner et al., 2009). Model-based studies on Himalayan Mountain are also limited because current generation of the model still has limited capacity in the land component of the global climate model in simulating land ice and glacier change. Menon et al. (2010) found using a GISS climate model with atmospheric only simulations, that spatial pattern of observed decline snow coverage in 1990 to 2000s is similar to that from model simulations due to present day black carbon aerosols.

In this study, we use a state-of-the-art global climate model to conduct a suite of well-designed model experiments to understand BC's role in cryosphere response. The BC forcing in our model simulations is constrained with observations (Chapter 2) and therefore likely have a better representation of present-day BC. Also, the simulations we conducted are using a fully coupled ocean-atmospheric-land model at a high resolution of 1 degree by 1 degree. The land model are improved with updated land snow module to account for BC deposition effect on snow and. These simulations provide us great opportunity to look at BC's impact on coupled climate system, in particular on the cryosphere.

Moreover, in addition to the BC perturbed simulations, we run similar model simulations with imposed present-day CO_2 (greenhouse gases that causes warming) and sulfate (major aerosols species that causes cooling) to understand the relative contribution from those species. By doing so, we can gain insight of the physical mechanism behind observed snow retreat.

The model description and experiment design is presented in Section 2. The main

results regard to simulated forcing and response of temperature and precipitation is shown in Section 3. In Section 4, we discussed the snow retreat and physical mechanisms. Section 5 discussed the implication of such a snow decline on surface albedo and hydrological cycle.

4.2 Methods

4.2.1 Model descriptions

CESM1 (Community Earth System Model 1) is a coupled ocean–atmosphere–land–sea-ice model developed by the National Center for Atmospheric Research and many Department of Energy and academic scientists (http://www2.cesm.ucar.edu/). The atmospheric and land components of CESM1 are CAM5 and CLM4, respectively (Neale et al., 2013; Lawrence et al., 2012). CESM1 climate simulations have been documented extensively (Meehl et al., 2013).

The anthropogenic forcing in CESM1 include time-evolving greenhouse gases (GHGs), as well as prescribed time- and space-evolving concentrations of tropospheric ozone, stratospheric ozone, the direct effect of sulfate aerosols and black and primary organic carbon aerosols (Lamarque et al., 2011). The 3-mode modal aerosol scheme (MAM3) has been implemented and provides internally mixed representations of number concentrations and mass for Aitken, accumulation, and course aerosol modes. The radiation scheme has been updated to the Rapid Radiative Transfer Method for GCMs (RRTMG) and employs an efficient and accurate correlated-k method for calculating radiative fluxes and heating rates.

The deposition of BC particles due to gravity or rainfall removal is a mechanism

to remove aerosol from the atmosphere and therefore is a sink term for the atmospheric BC mass balance. Some BC particles deposit on the surface of snow or ice (high albedo area) and reduce surface albedo. The snow model of CLM4 is significantly modified via incorporation of SNICAR (SNow and Ice Aerosol Radiation) which represents the effect of aerosol deposition (e.g. black and organic carbon and dust) on albedo, introduces a grain-size dependent snow aging parameterization, and permits vertically resolved snowpack heating (Flanner et al., 2007). This new module considers the albedo change by counting the surface concentration of BC and calculates the surface energy flux change at multiple wavelengths with a parameterization scheme. The surface albedo change will alter the energy balance on the surface and in the atmosphere. The net effect is enhanced absorption of solar radiation into the surface layer of the earth and an overall warming within the atmospheric column.

Time-evolving land use and land cover change are also included (Lawrence et al., 2011). The land model (CLM4) also has provision for major updates making it more versatile in simulating snow-related problems (sea ice, land snow pack, etc.). The spatial resolution also increases to one degree, so that the river runoff and the slope of the mountains can be better captured in the model.

As described in Chapter 2, we made efforts to improve the performance of BC simulation. The model now represents the BC aerosol atmospheric forcing and presumably its deposition on the surface better according to observational constrains.

4.2.2 Design of experiments

We have conducted several simulations using different initial conditions of atmosphere from a 319-year-long pre-industrial control run (blue line in Figure 4.1) and

extended it with an additional 70-year run to test if there was any discernible drift in the mean climate state. The Northern Hemisphere temperature does not show any statistically significant drift. Therefore, we lay the foundation to our analysis by employing the original 319-year data and the extended 70-year climate simulation data (389 years in total) as the control case.

We have conducted perturbed simulations by keeping the greenhouse gases and land same as the control run but boosting BC emissions by four fold from the pre-industrial level to the present-day level. Bond et al. (2013) show that the BC forcing has been most likely underestimated previously. In our experiments, the present day emission level is adjusted from the standard model emission inventory to account for the potential model underestimation of BC forcing. Our analysis presented in Chapter 2 show that such a correction would improve model simulated radiative forcing compared with direct observations.

We run the simulations for 70 years starting from the end of the 319th year (red solid line in Figure 4.1), similar to the extension of the original control simulation (black lines). To fully capture the uncertainty of natural variability of the climate system, five ensembles of simulations are conducted (green lines in Figure 4.1) using slightly different atmosphere as the initial condition. The average of the five ensemble members (red solid line in Figure 4.1) and its difference with the unperturbed simulation (black line in in Figure 4.1) will provide us the response signal to the imposed BC forcing.

To test the statistical significance of the temperature difference between perturbed simulations and long term control run, we also plotted the probability distribution function of the annual mean temperature in both time-series for global mean (Figure 4.1b)

and NH mean (Figure 4.1c).

4.3 Simulated forcing and model response of temperature and precipitation

4.3.1 Simulated forcing

We calculated the forcing (energy perturbation due to BC emission increase) using the diagnostic techniques by running the atmospheric-only model for five years. The forcing diagnostic calculation is described in detail in Chapter 2. The forcing we discussed here are "industrial-era forcing" due to BC emission increase from pre-industrial to present day level, also this is the "direct forcing" without involving slow response mechanism of SST/cloud/snow response. The diagnosed forcing is consistent with the radiative forcing imposed on the coupled model for the impact simulations, which is "pre-industrial to present day" value.

The BC TOA forcing (pre-industrial to present day) is 0.5 W/m^2 (Table 4.1), and this is 2.5 times larger than the modeled BC direct forcing (0.196 W/m^2) with standard BC emission inventory (Ghan et al., 2012). We described in Chapter 2 that such an adjustment of emission inventory is necessary for the simulated forcing to agree with observational estimates. The pre-industrial forcing itself (versus the zero BC emission simulations) is 0.15 W/m^2.

The all-source BC forcing in our simulation is therefore 0.65 W/m^2 (0.5+0.15), slightly lower than the estimates by Chung et al., (2012) (0.75 W/m^2). Bond et al., (2013) suggested a higher 0.88 W/m^2 for BC forcing, but also a -0.25 W/m^2 forcing of the co-emitted OC. Since our modified model has a close-to-zero TOA forcing for OC (see

Chapter 2 for details), the BC impact simulations discussed in this chapter is effectively equivalent to the simulation due to carbonaceous aerosols (BC+OC). Nevertheless, in addition to the five-member ensemble BC simulations, we also conducted a simulation with a higher BC forcing (global average forcing of 0.85 W/m^2, temperature response as red dash line of Figure 4.1). We consider the results from this simulation with high emission level provide the upper limit of BC impact. The BC TOA forcing used in this study and from previous studies is summarized in Table 4.1. For the following sections, the results are presented using the five-member ensemble BC simulations unless noted elsewhere.

Similar to the imposed BC forcing, we have also conducted simulations in which CO_2 concentration and SO_4 emissions are instantaneously increased from preindustrial level to present day level. The CO_2 concentrations were increased from 287 ppm to 400 ppm, and the associated TOA radiative forcing is 1.8 W/m^2 (Table 4.2).

The sulfate (SO_4) emission is increased from approximately 16 Tg S per year to the present day level of 50 Tg S per year. The total forcing (direct+indirect) is -0.9 W/m^2 (Table 4.1b), in which direct forcing contributes -0.2 W/m^2. The direct forcing due to SO_4 is calculated by calling the radiative transfer code twice at pre-industrial run and present-day run (similar to the techniques applied to BC and CO_2 forcing calculation). The total forcing that involves cloud albedo change due to increasing cloud condensation nuclei number concentration is calculated from the TOA flux difference of pre-industrial run and present-day run. The short wave indirect forcing (about -1.5 W/m^2) is compensated by a relatively large long wave indirect forcing (0.8 W/m^2) due to increasing cirrus at upper troposphere (Ghan et al., 2013).

4.3.2 Temperature response at global and hemispheric scale

In the impact-study simulations, the $BC/CO_2/SO_4$ forcing is imposed onto ocean-atmosphere coupled model and the model is run for 75 years. We calculate the average model properties using the last 60 years of simulations (after the 15 year of model spin-up period) and contrast the average of the last 60 year with the long-term control average to obtained the climate response signal due to imposed forcing ($BC/CO_2/SO_4$). The mean surface temperature change due to imposed BC forcing is 0.21 °C (Figure 4.1a). Note that this is only a fraction of the equilibrium temperature response to imposed BC forcing (0.5 W/m^2). Our simulation (75 years) is not long enough for the model to reach full equilibrium state, and due to the 60-year averaging scheme, we were effectively calculating the model response on the year 45 after the imposed forcing. The probability distribution function of global mean temperature in the long-term control run and BC perturbed run show clear departure (Figure 4.1b), suggesting the statistical significance of climate response.

We note that there seems to be an increasing trend in temperature during the simulated 70 years, but this is more likely due to the initial condition of the model's starting year and more of a consequence of climate system inertia. The moderate warming (0.5 °C) is likely a rebound from the previous cooling period (year 270 to year 320). Such warming/cooling periods of this magnitude were seen multiple times during the course of the 319-year simulation, and therefore the trend during the last 70-year simulation shall not be taken as a response signal but rather as the natural variability within the climate system.

On the contrary, in the case of perturbed simulations initialized from year 319, all

five-ensemble members (green lines) demonstrate a warming trend that exceeds the natural variability (black line). The temperature of the Northern Hemisphere increased by 0.8 $^{\circ}$C during the 70 years of simulation, and it was, on an average, 0.3 $^{\circ}$C warmer in the perturbed simulation than in the unperturbed simulations during the same period (Table 4.2). The wide range of warming signals found in five ensemble simulations (from 0 to 1°C) is due to the selection of initial conditions and is likely able to capture the possible uncertainty of the warming signal. Additionally, the upper limit of BC warming signal over North Hemisphere (red dash in Figure 4.1) is about 0.8 $^{\circ}$C at the end of the 70-year simulation, corresponding well to the larger forcing imposed (0.85 W/m^2 instead of 0.5 W/m^2 in the five ensembles).

Globally, BC induced warming is less than 20% of CO_2 warming, which is approximately scaled with the imposed TOA forcing. The simulated warming due to BC and CO_2 is at about 0.4-0.5 $^{\circ}$C/(W/m^2), smaller than the equilibrium climate sensitivity reported for this model (Gettelman et al., 2011), because the temperature response is effectively calculated at the model simulation year of 45. As noted in earlier studies, the BC (SO_4) forcing produced a stronger north-south asymmetry in temperature response: Northern hemisphere warming (cooling) is 2-3 times larger than Southern hemisphere warming (cooling). The asymmetric feature in temperature response to CO_2 is much smaller (with only 30% stronger warming over North hemisphere) and is probably only due to the land-ocean fraction difference in north-south hemisphere (see discussions in Chapter 3 and Xu and Ramanathan, 2012).

The north-south asymmetric feature induced by BC aerosols, which has a larger loading over industrial Northern Hemisphere, is well simulated in the model. The

Northern Hemisphere (30 °N to 90 °N) is warmed by over 1°C in the high-end case (red dash line). In the medium forcing case (red solid line), the average of the five-ensemble simulations is warmer than the unperturbed simulation by 0.7 °C.

Over Arctic, the warming is amplified by a factor of 3.5 in both BC and CO_2 cases. Over Tibet, the warming is amplified by a factor of 4 in BC cases and only a factor of 1.5 in CO_2 case. The mechanisms of such an amplification of warming due to BC and its consequences on snow and ice will be discussed in detail later.

4.3.3 Hydrological cycle response

The global change of precipitation in response to BC is slightly increased but close to zero (Table 4.3 and Figure 4.1(c)). The negligible global precipitation response is probably due to the cancellation of two opposing effects of BC forcing (Ming et al., 2010) (1) the increasing precipitable water (0.37 mm, Table 4.4) from enhanced evaporation due to surface warming and (2) the increase of atmospheric stability due to the atmospheric heating. However, BC induces shifts of precipitation from southern hemisphere to northern hemisphere, with an increased cumulative precipitation of 0.54 cm and decrease of similar amount over south hemisphere. Such a feature of hemispheric shift of precipitation and in particular the shift of Inter-tropical Convergence Zone has been studied extensively (Chung and Seinfeld, 2002; Wang et al., 2008; Bond et al., 2013).

The precipitation in response to CO_2 warming is an over increase (1.7 cm in cumulative precipitation) with almost no hemispheric difference (Table 4.3). The global reduction of precipitation in response to SO_4 is also significant (2.1 cm). The precipitation reduction in response to sulfate aerosols are due to reduced solar radiation

reaching the surface in addition to the cooling of surface temperature (Ramanathan et al., 2001), and therefore, the reduction of precipitation scaled with temperature (cm/K) is much larger for the sulfate cooling (4.3 cm/K) than CO_2 warming (1.5 cm/K). The reduction of precipitation in response to SO_4 also shows a stronger asymmetry, with north hemispheric reduction 5 times larger than southern hemisphere, consistent with the emission sources spatial distribution. Such a hemispheric asymmetry can also be found in the surface latent heat flux change (Table 4.8).

4.4 Enhanced warming and snow reduction over Tibet due to BC

4.4.1 Modeled enhanced warming at high altitude

For the Tibet snow and ice, more important than the warming signal at the surface is the vertical thermal structure change. Such a change of atmospheric temperature profile is a strong indicator of human-induced climate change and has been used in detection and attribution studies (Santer et al., 2012). The thermal structure change in response to BC aerosol is also examined here by contrasting the average of the 70-year perturbed run versus the unperturbed run during the same period. Figure 4.2(b) shows the temperature response (as a function of altitude and latitude) to BC aerosols as well as CO_2 and SO_4. The responses of five individual simulation members of BC case are similar as the ensemble average.

As discussed earlier, the warming is more concentrated over Northern Hemisphere due to larger emissions there from industrial activities. The Southern Hemisphere witnessed limited warming in general, except for ensembles 2 and 3, where

it propagated to the Southern Hemisphere through tropical upper tropospheric warming. Such a mechanism is suggested to be important in determining the overall structure of global warming pattern (Xie et al., 2013).

In Figure 4.2b, the notable feature of the elevated warming signal at locations at altitude of 4 to 8 km and 30 to 60°N is mostly contributed by the elevated warming over Tibet Plateau. The warming (of about 0.5 to 0.6°C) extends from the surface all the way up to about 200 hPa. Figure 4.4 shows the daily-minimum surface temperature response as a function of elevation (m) due to three different forcing agents. The temperature responses are calculated from the all model grid cells over Tibet Plateau and surrounding region (20-50°N, 70-110°E). The standard deviation (due to spatial variation of temperature response) is shown as error bars of X-axis. The altitude dependence of simulated warming is clear. At altitudes below 800 hPa, warming is minimum and in some cases zero or even slightly negative. As the altitude goes up, the magnitude of warming increases up to 2 °C in 500 hPa with a large spread of uncertainty.

Other studies have shown that the recent three decades have witnessed warming of two times larger in the interior of Tibetan Plateau than the warming trend detected at the edge of the plateau and lower altitude (Liu et al., 2009). The observed warming also revealed such altitude dependence (blue dots in Figure 4.4). The observations (Liu et al., 2009) were made during 1965 to 2006 from the ground meteorological stations around Tibet Plateau. The reported warming rate per decade is multiplied by 4.5 to obtain the temperature change in 45 years (blue dots in Figure 4.4). Since the changes of our model simulations is effectively the response at the 45^{th} model years, we also plotted the combined temperature response by adding the responses due to BC, CO_2 and SO_4

together. Despite the fact our model simulation used an instantaneous increase of atmospheric compositions rather than the gradual increase of aerosol and greenhouse gases, the combined temperature response shows surprisingly similar pattern with observations. Qualitatively this provide us the relative contributions of BC, CO_2 and SO_4 in Tibet warming.

The CO_2 warming structure (Figure 4.2b) features an amplified warming signal at the surface of the Arctic and heating anomaly in upper tropical troposphere. Such heating structure is often seen as a strong indication of human-induced global warming (Santer et al., 2012). Sulfate cooling suggests similar vertical structure (Figure 4.2), but with a strong inclination of north-south asymmetry (north cooling, south slightly warming). The dependence of warming on altitude is much smaller in the CO_2 cases, which only increase from 1.2 °C warming at low altitude to 1.6 °C at higher altitude at more than 5 km. The normalized temperature responses from SO_4 cases show that the cooling is more concentrated at the surface (Figure 4.3b), because most of the SO_4 cooling is induced at the surface layer while the atmospheric forcing is close to zero (Figure 4.3a).

Note that the surface warming due to CO_2 is over five times larger than that of BC globally and four times larger over the Northern Hemisphere. However, over the entire Tibetan Plateau, CO_2-induced surface warming is 1.3 °C, compared to the BC-induced warming of 0.83 °C (Table 2.2). CO_2 induced warming at upper atmosphere (500 mb) over Tibet is 1 °C, compared to a BC-induced warming of 0.5 °C. Therefore, the surface warming over Tibet is amplified by a factor of 4 in the BC case from its global average and only 130% in the CO_2 case. The fact that CO_2 warming is amplified over Tibet but to a much smaller extent suggests that at least over high-altitude region, BC is a warmer as

effective as CO_2.

4.4.2 Mechanism of elevated warming due to BC

The elevated warming demonstrated in Figure 4.3(b) is mostly due to the BC aerosol emission over India and China, and its transport over Tibet Plateau and the Himalayan Mountain range (Kopeck et al., 2011), since the industrial activity and population density over Tibet Plateau itself is very limited. Such an elevated signal of warming is the direct result of the large amount of aerosol emission from both sides of Tibet Plateau and Himalayan Mountain elevated by topography. Because the monsoon system over South Asia and East Asia is very strong, and the precipitation over Tibet is not sufficient in removing aerosols from atmosphere, the transport of aerosols into the air above the Tibet Plateau is quite efficient (Lu et al., 2012).

The physical mechanism of the amplified warming due to BC at higher altitude is two-fold:

(1) Direct heating of the atmosphere. BC absorbs a significant amount of solar radiation (25% in typical pollution events as directly measured by multiple unmanned aircrafts over North Indian Ocean (Ramanathan et al., 2007 and Ramana et al., 2008). The BC layer placed at higher altitude is even more efficient in absorbing solar radiation than the sea level due to stronger solar radiation reaching surface. In our model simulation, the transport of BC into the atmosphere above Tibet plateau cause radiative heating due to solar absorption (Figure 4.3a), which is at more than 0.1 K/day at the surface layer and extend to about 4 km at a rate of 0.03 K/day. The elevated BC layer due to the topography of Tibet plateau and Himalaya Mountains contributes to the elevation of heating. In addition to the direct radiative heating, the moist convection is also

magnified due to the reduced atmospheric stability and therefore it distributes more surface heating into higher atmosphere at a rate of more than 0.1 K/day (Figure 4.2).

Similarly, for the CO_2 warming case, the enhancement of warming at upper troposphere of low latitude (Figure 4.2b) are also a combined heating effect due to both long wave heating (Figure 4.2a) and heating of moist convection. Such an enhancement of moisture convection heating is necessary for the model to maintain the moist adiabatic lapse rate, which is more stable in CO_2 warming case (Manabe and Wetherald, 1974).

(2) The BC deposition of the snow surface will cause the decrease of surface albedo and therefore enable the land surface absorb more solar radiation (e.g. Hansen and Nazarenko, 2004). Observation evidence of ice-core measurements of historical BC over Tibet glacier also suggests such a link (Xu et al., 2009). Recent global modeling studies (e.g. Menon et al., 2009) showed that when the model includes snow albedo change due to black carbon, the snow cover reduction is twice larger than the simulation with black carbon atmospheric heating effect only. Flanner et al., (2009) also suggest that BC surface albedo darkening effects are important in causing Eurasian springtime snow/ice cover decline and are comparable to that of CO_2. The surface warming due to BC deposition over Tibet is estimated to be 4.6 W/m^2 based on a 6-year atmospheric-only simulation (Figure 4.5b). Because of this strong positive surface forcing, the shortwave adjusted forcing due to BC at the surface increased from the -1.5 W/m^2 (initially due to BC dimming effect) to a positive value of 2.6 W/m^2. The positive surface forcing is even larger than the adjusted atmospheric heating due to BC over Tibet (1.6 W/m^2). We note that to accurately diagnose the surface forcing only due to BC deposition, an offline radiative transfer code is needed.

The elevated warming and surface darkening are operating simultaneously to cause local warming and consequentially leads to snow melting and further reduction of surface albedo, which then provides a positive feedback mechanism. The net results of such a positive loop is the amplification factor of 4 for Tibet warming from global average and associated snow and ice retreat, which we will discuss next.

4.4.3 Reduction of snow fraction and snow depth

Due to such an elevated warming, the cryosphere response is significantly larger than natural variability. This provides a good indicator in detecting climate change due to air pollutants. Of course, such a change in snow and ice in cryosphere by itself is significant and of environmental consequence.

The National Snow and Ice Data Center (Armstrong and Brodzik, 2005) data shows that the snow cover over the Himalayan range has declined at a rate of more than 10% per decade as per satellite measurements of 1990–2001 (Menon et al., 2010). This decline in snow coverage in the simulation has largely been reproduced compared to the observed pattern. Overall, over the Northern Hemisphere, the ice fraction has reduced by 0.4 million sq. km (0.3% reduction from control simulations) in response to BC. Tibet Plateau is one of the regions witnessing largest reduction in snow fraction with average reduction of 2%. Figure 4.7a shows the simulated change of snow cover fraction over Tibet. The snow fraction also shrinks by 2.8% due to present-day CO_2. Notably, snow fraction over Eastern China decreased by 0.7% and 1.3% due to BC and CO_2, respectively. Along the Himalayas mountain range where the near-permanent snow cover exists, the reduction of snow fraction exceeds 10% in both BC and CO_2 cases.

The increased ground temperature leads to a larger snow melting heat flux, which

averages 0.2 W/m^2 over Tibet. Along the Himalaya mountain range, the snow melting heat flux is as much as 2 W/m^2. Such an increase of heat flux into the snow layer causes larger snow melts by about 0.5 mm/day at the edge of Tibet Plateau. Due to higher temperature, the precipitation in the form of snow also reduced by 0.3 mm/day along the mountain range and by 0.03 mm/day averaged over Tibet Plateau.

In addition to the shrink in snow coverage, snow depth is also reducing considerably. Our model estimates that over the entire Northern Hemisphere, the snow depth has reduced by more than 7% from the long-term control run (Figure 4.6). The significance test suggests a more than 95% likelihood of BC contributing to it. The average snow reduction over Tibet region is at least five times larger than that due to CO_2. Over the Tibetan Plateau, reduction in snow depth reduction is more pronounced with a reduction of 5% to 10%. In contrast, low elevation regions (Sichuan and northeastern China) also signal reduction but at a smaller magnitude. The spatial pattern of snow depth reduction is consistent in all five ensembles of model simulations.

In response to CO_2 warming, part of Himalayan region actually shows slight increase in the depth of snow by 1% to 5%). This is probably resulting from the snowfall increase compensating for the melting due to warming. In fact, the precipitation over Tibet and Himalayan region indeed increase by 5% to 10% due to BC aerosols, which is comparable to the magnitude of CO_2 response. The magnitude of snow depth retreat simulated in the idealized model simulations is effectively the response in a 45-year time period after the emission increases. In ensemble 3 and 4 of BC runs, we also see a small increase in snow depth, but in most of the ensembles, the snow depths are reduced.

As the volume of snow is proportionate to its depth, such as thinning of the layer

has tremendous impact on river runoff and fresh water availability, which we will discuss in the next section.

4.5 Implication of snow and ice reduction

4.5.1 Surface albedo decrease

One consequence of land ice and snow reduction is the surface albedo change, which may provide a feedback mechanism to the localized warming. Such a surface albedo change in response to ice loss has been observationally detected (Pistone et al., 2013, Kay and L'Ecuyer, 2013) and is important to explain the amplified Arctic warming. Our calculations show that surface albedo over Tibet region decreased by over 5% (Figure 4.8). Again, such a decrease in albedo is consistently shown in all five-ensemble simulations with limited variability. The maximum reduction occurs right along the Himalayan mountain range and part of Tibet-Sichuan Mountains. The surface albedo reduction from CO_2 shares similar spatial pattern with BC but with smaller magnitude highlighting the importance of BC in causing regional cryospheric change.

4.5.2 Seasonality of the impact on river runoff and hydrology

The ice and snow over Tibet and Himalayas provide valuable water sources for several major rivers in Asia. The statistics on Tibet suggest that the snow depth snow decreases from 12 cm to 9 cm during spring and lessens towards summer when the overall snow cover reduces due to warmer summer weather. The surface runoff along Himalaya mountain range increase by 0.4 mm/day.

During June–August snow cover reduces to zero over bulk of Tibet Plateau; however, maximum river runoff happens when the melting water flows through the rivers

downstream. The early melting of snow mass also creates a slightly bigger runoff. Correspondingly, the runoff during the subsequent months (May and June) is reduced by 5%. Effectively the seasonality of the run off shifts to early spring.

Such a seasonal shift in hydrological cycle was also investigated by earlier studies focusing on greenhouse-gas-induced warming. Recently people also started studying the aerosols' effect on mountain snow and river runoff (Painter et al., 2010). These studies along with the results presented here demonstrate that human factors need to be considered in future operation of hydrological facilities or in planning of dam construction and operation.

4.6 Conclusions

In this study, we demonstrate that, with a state-of-the-art ocean–atmosphere–land–chemistry model, the cryosphere over Tibet and Himalayan regions is under the direct influence of anthropogenic pollutants transported from both sides of the high elevation regions. The magnitude of elevated warming and spatial patterns of reduced snow coverage simulated by the model corresponds well with the observational data from satellite and ground network.

Additional experiments with increased CO_2 show that BC is the dominant force in causing snow reduction. It is a two-fold process: (i) direct atmospheric heating, and (ii) BC deposition on snow surface. Though future work is needed to clearly differentiate the relative contributions from each source, previous studies have suggested that surface darkening due to deposition on snow plays a major role in the reduction in snow (Flanner et al., 2007).

Our study also highlights the elevated warming structure that is unique to BC. The elevated warming is as big as, if not bigger than CO_2 warming, over Tibet Plateau. Such an anomaly is bringing in more moisture into the Tibetan region leading to more snowfall. However, the overall effect is a reduction in snow cover due to warming. Further analysis is needed to gain a better understanding of the causes of snow reduction.

Tables

Table 4.1 CESM simulated global average of TOA forcing (W/m^2) of BC and sulfate aerosols, compared with selected previous studies. The "direct" radiative forcing of BC and sulfate aerosols (not involving changes of clouds and water vapor, etc.) were calculated with the diagnostic procedures described in detail in Chapter 2. For example, to calculate the direct forcing of "all-sources" BC, two sets of 6-year simulation of the atmospheric only model at year 2000 climatology were conducted: one with present-day emission, one with zero emission of BC. Similar sets of calculations were done to calculate "pre-industrial to present-day" forcing of BC and sulfate. The range of BC radiative forcing is due to uncertainty of emission inventory used in the simulation. The lower limit of forcing (0.49 W/m^2 for pre-industrial to present day) is used in the five-ensemble climate impact simulations. The higher limit of forcing (0.85 W/m^2 for pre-industrial to present day) is used in only one ensemble member of climate impact simulations. Note that total sulfate forcing (direct+indirect, so called "effective forcing") is calculated using similar two sets of atmospheric only simulation but allowing water vapor and clouds to adjust to sulfate emission change.

BC (W/m^2)	This study	Bond et al., 2013	Chung et al., 2012	Ramanathan and Carmichael, 2008	IPCC_AR5 (Figure 7.18)
All-sources	0.65-1	0.88	0.75	0.9	-
Since pre-industrial	0.49-0.85	0.71	0.65	-	0.05-0.8 (best estimates at 0.4)

Table 4.1 Continued.

Sulfate (W/m^2)	This study (direct only)	This study (direct+indirect, or so called "effective forcing")	Ghan et al., 2013 (direct only)	IPCC_AR5 (Fig 7.18, direct only)	IPCC_AR5 (Fig 7.19 (expert judgement, effective forcing, due to all aerosols)
Since pre-industrial	-0.15	-0.85	-0.176	-0.2 to -0.6 (best estimates of -0.4)	-0.45 to -1.5 (best estimates of -0.9)

Table 4.2 (a) TOA forcing (W/m^2, shortwave + longwave) due to BC (direct radiative forcing, pre-industrial to present-day; not including snow albedo effect), CO_2 (pre-industrial to 400 ppm), and SO_4 (direct+indirect effect, so called "adjusted forcing", pre-industrial to present-day). The forcing is calculated by running atmospheric model for 6 years. (b) Surface temperature change (˚C) in response to different forcings in (a). Surface temperature change is calculated from a 60-year average of coupled model simulation, and is effectively the model response at the year 45 after the forcing is applied. The domains of selected regions are the following: Arctic: north of 75˚N; Antarctic: south of 75˚S; Tibet: 30 to 40˚N and 80 to 100˚E; East China: 20 to 50˚N and 105 to 120˚E; India: 0 to 30˚N and 70 to 90˚E.

(a) TOA net forcing (W/m^2)	BC	CO_2	SO_4
Global	0.5	1.7	-0.9
NH	0.7	1.7	-1.5
SH	0.2	1.7	-0.2
Arctic	0.3	1.4	-0.7
Antarctic	0.1	0.9	0.8
Tibet	1.1	0.6	-0.3
E China	3.6	1.2	-1.5
India	2.0	2.1	0.5

Table 4.2 Continued.

(b) Surface temperature change (˚C)	BC	CO_2	SO_4
Global	0.21	1.15	-0.49
NH	0.29	1.29	-0.74
SH	0.14	1.01	-0.25
Arctic	0.71	4.12	-1.42
Antarctic	0.2	1.61	-0.12
Tibet	0.84	1.53	-0.73
E China	0.42	1.28	-0.94
India	0.13	1.01	-0.56

Table 4.3 Cumulative precipitation (cm) change in response to different forcing agents. The global change of precipitation in response to BC is close to zero. This is due to the cancellation of two opposing effects: (1) increasing precipitable water (Table 4.4) due to the warming (Table 4.2b) and (2) tendency of reducing surface evaporation (Table 4.8) due to surface dimming (Table 4.6). In addition, the increasing of atmospheric stability due to warming of atmospheric tends to suppress precipitation. However, BC induces latitudinal shifts of precipitation from southern hemisphere to northern hemisphere. The reduction of precipitation in response to SO_4 is large and shows very strong hemispheric asymmetry. The relative change of precipitation in percentage is shown in parenthesis next to the absolute change.

	BC	CO_2	SO_4
Global	-0.01 (0%)	1.73 (2%)	-2.09 (-2%)
NH	0.54 (1%)	1.74 (2%)	-3.71 (-6%)
SH	-0.56 (-1%)	1.72 (2%)	-0.48 (1%)
Tibet	2.32 (4%)	3.73 (6%)	-2.93 (-5%)
E China	0.12 (0%)	2.32 (2%)	-9.85 (-8%)
India	4.01 (2%)	5.64 (3%)	-11.92 (-7%)

Table 4.4 Similar with Table 4.3. Precipitable water (mm) change in response to different forcing agents. The relative change of precipitation in percentage is shown in parenthesis next to the absolute change.

	BC	CO_2	SO_4
Global	0.37 (2%)	1.72 (7%)	-0.67 (-3%)
NH	0.5 (2%)	1.8 (7%)	-0.92 (-4%)
SH	0.23 (1%)	1.64 (7%)	-0.41 (-2%)
Tibet	0.25 (5%)	0.55 (11%)	-0.3 (-6%)
E China	0.7 (3%)	1.68 (8%)	-0.95 (-4%)
India	0.98 (3%)	2.76 (7%)	-1.29 (-4%)

Table 4.5 Similar with Table 4.2(a), but separately showing both direct radiative forcing and adjusted forcing that involves rapid cloud changes. Note that SST were fixed in both calculations preventing slower feedback mechanisms. (a) TOA net forcing (W/m^2, shortwave + long wave) due to BC (pre-industrial to present-day), CO_2 (pre-industrial to 400 ppm), and SO_4 (pre-industrial to present-day). The forcing is calculated by running atmospheric model for 6 years. The forcings are shown in both radiative forcing (direct forcing) and adjusted forcing (direct forcing + semi-direct forcing + indirect forcing that involves fast feedback. (b) TOA shortwave forcing. (c) TOA long wave forcing.

(a)	BC		CO_2		SO_4	
TOA net forcing (W/m^2)	Radiative forcing	Adjusted forcing	Radiative forcing	Adjusted forcing	Radiative forcing	Adjusted forcing
Global	0.5	0.3	1.7	1.8	-0.2	-0.9
NH	0.7	0.6	1.7	2.0	-0.3	-1.5
SH	0.2	-0.1	1.7	1.6	0.0	-0.2
Tibet	1.1	3.8	0.6	0.3	0.0	-0.3
E China	3.6	6.0	1.2	2.9	-0.6	-1.5
India	2.0	1.6	2.1	-0.2	-0.5	0.5

Table 4.5 Continued.

(b)	BC		CO_2		SO_4	
TOA Shortwave forcing (W/m^2)	Radiative forcing	Adjusted forcing	Radiative forcing	Adjusted forcing	Radiative forcing	Adjusted forcing
Global	0.5	0.6	0.0	0.4	-0.2	-1.7
NH	0.7	0.9	0.0	0.7	-0.3	-2.7
SH	0.2	0.4	0.0	0.2	-0.1	-0.7
Tibet	1.0	5.6	0.0	-3.3	0.0	-2.3
E China	3.6	5.9	0.0	-0.9	-0.7	-2.9
India	2.0	3.0	-0.1	1.0	-0.5	-5.8

Table 4.5 Continued.

(c)	BC		CO_2		SO_4	
TOA Longwave (W/m^2)	Radiative forcing	Adjusted forcing	Radiative forcing	Adjusted forcing	Radiative forcing	Adjusted forcing
Global	0.0	-0.4	1.7	1.4	0.0	0.9
NH	0.0	-0.3	1.8	1.3	0.0	1.3
SH	0.0	-0.5	1.7	1.5	0.0	0.5
Tibet	0.0	-1.8	0.6	3.6	0.0	2.1
E China	0.0	0.0	1.1	3.8	0.1	1.4
India	0.0	-1.4	2.3	-1.2	0.0	6.2

Table 4.6 Similar to Table 4.5, but showing surface forcing (W/m^2, due to BC (pre-industrial to present-day), CO_2 (pre-industrial to 400 ppm), and SO_4 (pre-industrial to present-day). The forcing is calculated by running the atmospheric model for 6 years. Forcing shown are shortwave for BC and SO_4, longwave for CO_2).

	BC (shortwave)		CO_2 (longwave)		SO_4 (shortwave)	
Surface forcing (W/m^2)	Radiative forcing	Adjusted forcing	Radiative forcing	Adjusted forcing	Radiative forcing	Adjusted forcing
Global	-0.6	-0.6	0.7	0.5	-0.2	-1.9
NH	-1.0	-1.0	0.7	0.4	-0.3	-2.9
SH	-0.3	-0.2	0.6	0.6	-0.1	-0.8
Tibet	-1.5	2.6	-0.6	3.7	-0.4	-3.4
E China	-6.6	-4.4	0.8	0.2	-1.3	-3.5
India	-3.8	-3.1	0.5	0.4	-0.6	-5.6

Table 4.7 Similar to Table 4.6, but showing the change of atmospheric heating (W/m^2, shortwave + long wave) due to BC (pre-industrial to present-day), CO_2 (pre-industrial to 400 ppm), and SO_4 (pre-industrial to present-day). The forcing is calculated by using atmospheric model for 6 years. The change of atmospheric heating is the difference of TOA forcing (Table 4.5 b and c) and surface forcing (Table 4.6).

	BC (shortwave)		CO_2 (longwave)		SO_4 (shortwave)	
Atmospheric forcing (W/m^2)	Radiative forcing	Adjusted forcing	Radiative forcing	Adjusted forcing	Radiative forcing	Adjusted forcing
Global	1.1	1.2	1.1	0.9	0.0	0.1
NH	1.7	1.9	1.1	1.0	0.0	0.2
SH	0.5	0.5	1.1	0.9	0.0	0.1
Tibet	2.5	3.0	1.2	-0.2	0.4	1.1
E China	10.2	10.3	0.3	3.7	0.6	0.6
India	5.8	6.1	1.8	-1.6	0.2	-0.2

Table 4.8 The change of surface latent heat flux and sensible heat flux (W/m^2) as a consequence of imposed forcing. The changes are calculated by contrasting two sets of 60-year long coupled model simulations in which respective forcing are included or not.

Latent heat flux	BC	CO_2	SO_4
Global	0.0	1.3	-1.6
NH	-0.3	1.1	-2.1
SH	0.3	1.6	-1.2
Tibet	1.1	1.2	-1.8
E China	-0.5	0.6	-4.5
India	-1.0	0.9	-3.1

Sensible heat flux	BC	CO_2	SO_4
Global	-0.2	-0.2	0.0
NH	-0.4	-0.1	0.1
SH	-0.1	-0.3	0.0
Tibet	0.0	0.4	-0.4
E China	-2.1	1.0	-1.1
India	-2.3	0.0	-0.3

Table 4.9 Snow depth over land (water equivalent, cm) change in response to different forcing agents. The changes are calculated by contrasting two sets of 60-year long coupled model simulations in which respective forcing are included or not. The relative change of precipitation in percentage is shown in parenthesis next to the absolute change.

	BC	CO_2	SO_4
Global	-0.06 (-2%)	-0.15 (-4%)	0.1 (3%)
NH	-0.11 (-6%)	-0.28 (-14%)	0.2 (10%)
SH	-0.01(0%)	-0.02 (0%)	-0.01 (0%)
Arctic	-1.44 (-7%)	-4.75 (-25%)	2.27 (12%)
Tibet	-0.2 (-19%)	-0.06 (-6%)	0.16 (15%)
E China	-0.02 (-17%)	-0.02 (-17%)	0.01 (8%)
India	-0.03 (-50%)	-0.01 (-17%)	-0.01 (-17%)

Table 4.10 Snow fraction (%) change in response to different forcing agents. The changes are calculated by contrasting two sets of 60-year long coupled model simulations in which respective forcing are included or not.

	BC	CO_2	SO_4
Global	-0.13 (-2%)	-0.35 (-4%)	0.14 (2%)
NH	-0.26 (-3%)	-0.67 (-7%)	0.36 (4%)
SH	-0.01 (0%)	-0.04 (-1%)	-0.09 (-2%)
Arctic	-0.32 (-1%)	-1.06 (-4%)	-0.06 (0%)
Tibet	-1.9 (-6%)	-2.83 (-9%)	1.65 (5%)
E China	-0.75 (-9%)	-1.31 (-15%)	0.62 (7%)
India	-0.15 (-19%)	-0.15 (-19%)	0.02 (3%)

Table 4.11 Surface albedo change (units: %) in response to different forcing agents. The changes are calculated by contrasting two sets of 60-year long coupled model simulations in which respective forcing are included or not.

	BC	CO_2	SO_4
Global	-0.2 (-1%)	-0.68 (-4%)	0.28 (2%)
NH	-0.3 (-2%)	-0.79 (-5%)	0.44 (3%)
SH	-0.1 (0%)	-0.56 (-4%)	0.12 (1%)
Arctic	-1.5 (-2%)	-7.74 (-11%)	2.15 (3%)
Tibet	-1.4 (-2%)	-1.1 (-2%)	1.1 (2%)
E China	-0.3 (-2%)	-0.32 (-2%)	0.26 (2%)
India	-0.1 (-1%)	-0.05 (-1%)	0.06 (1%)

Figures

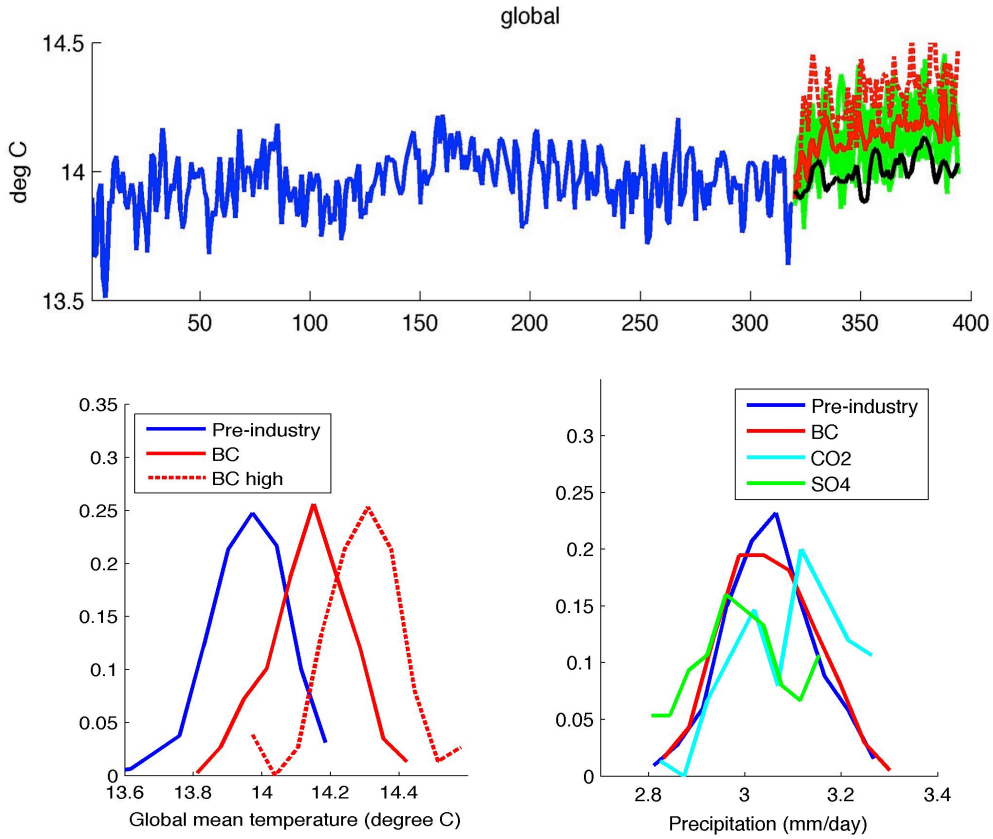

Figure 4.1 (a) Global mean tempeaurea change in the coupled model simulations. Blue line is the long-term control simulation (319 years) with pre-industrial BC. Black line is the extension of the long-term control simulations for another 70 years. Green lines are five ensemble members of the simulations, in which BC emission instantaneously increases from pre-industrial level to present day level. Red solid line is ensemble average of the green lines. Red dash line is an individual simulation in which BC emission is increased to a higher level to account for the upper limit of BC forcing. (b) Probability distribution function of annual mean temperature in pre-industrial simulations of 319 years (blue), BC perturbed simulations of 75 years (red) and perturbed simulations of 75 years with higher BC emission (red dash). (c) Probability distribution function of precipitation rate in pre-industrial simulations (blue), BC perturbed simulations (red), CO_2 perturbed simulations (cyan) and SO_4 perturbed simulations (green).

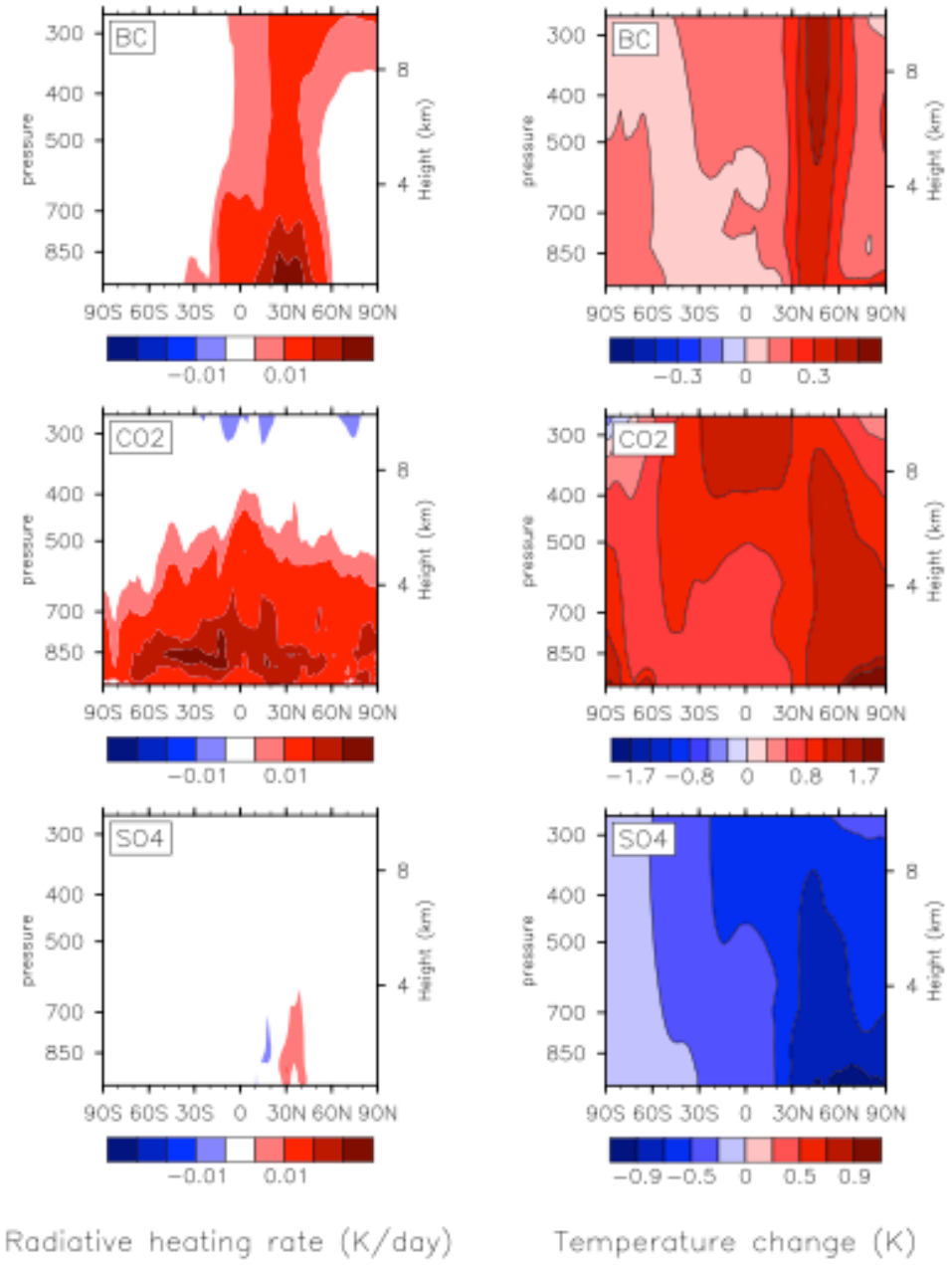

Figure 4.2 (a) Radiative heating rate (K/day) as a function of altitude and latitude due to BC, CO_2 and SO_4, calculated from the five year atmospheric only simulations using the radiative diagnostic procedure. (b) The temperature response ($^{\circ}$C, calculated as the difference of the last 60 years of perturbed simulation and the 319 year long term control), under three different forcing agents (BC, CO_2 and SO_4).

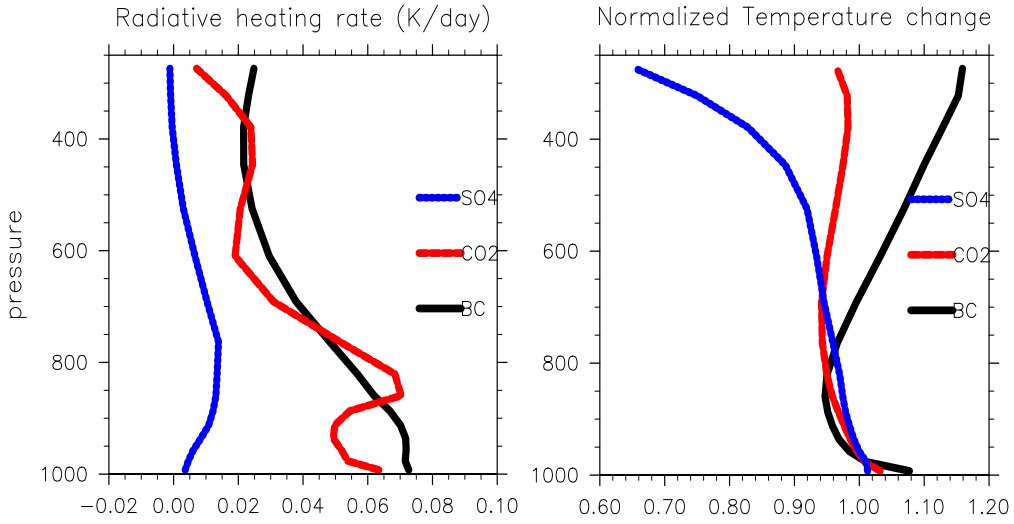

Figure 4.3 Similar with Figure 4.2, but showing the vertical profile averaged over Tibet region of radiative heating rate (K/day) in left panel, and temperature change (K) in right pandel. The calculation methods are the same as described in Figure 4.2. Note that the temperature changes are simulated atmospheric temperature change.

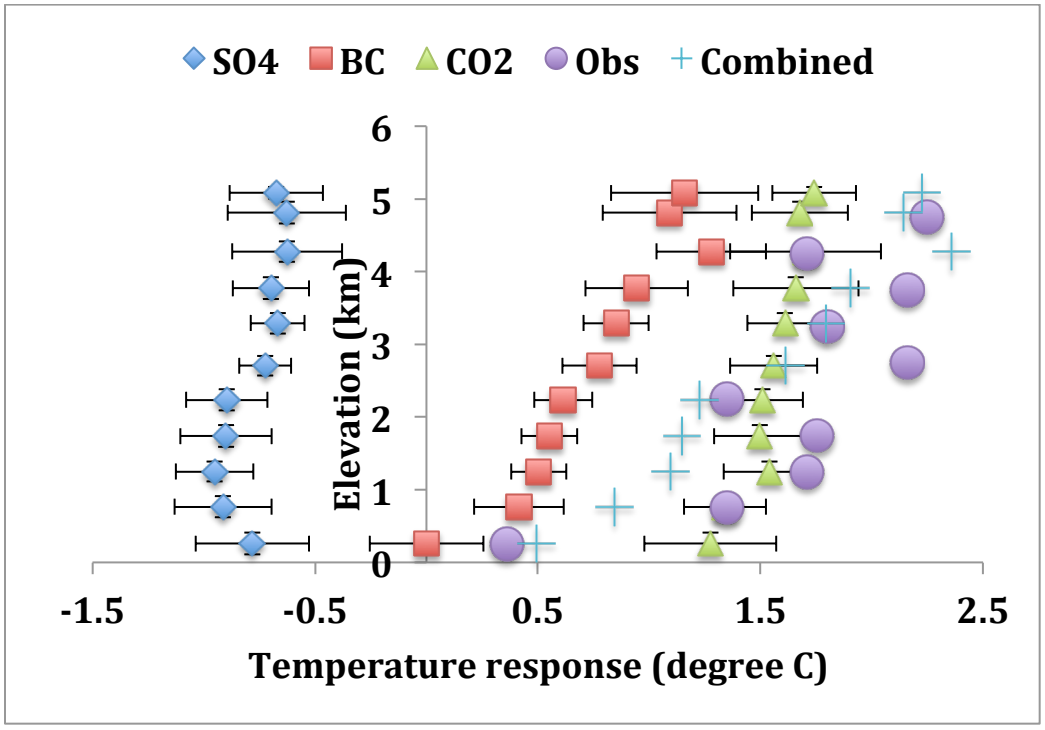

Figure 4.4 The daily-minimum temperature change (°C) as a function of elevation (m) due to three different forcing agents. The temperature responses are calculated from the all model grid cells over Tibet Plateau and its surrounding region (20-50°N, 70-110°E). The standard deviation (due to spatial variation of temperature response) is shown as error bar of X-axis. Observations from 1961 to 2006 (°C) are taken from Figure 3 of Liu et al., (2009). The addition of BC, SO_4 and CO_2 response are shown in crosses. Note that simulated temperature changes here are ground temperature at different altitude, in order to compare with observed ground temperature.

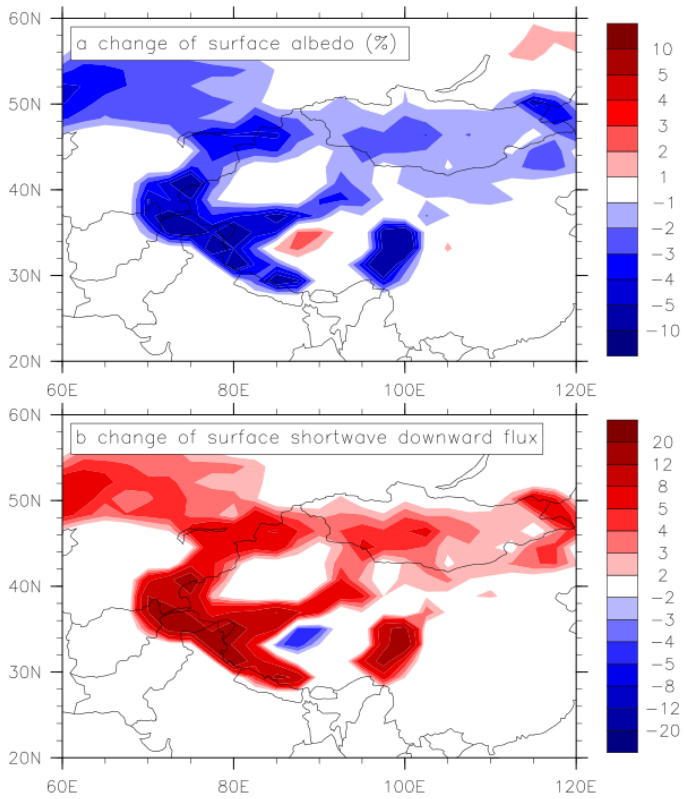

Figure 4.5 (a) Surface albedo change in the five-year atmospheric only model simulations, due to BC deposition on snow and consequential melting, (b) change of shortwave radiation reaching the surface (W/m^2) due to surface albedo change. Over Tibet, the surface albedo is reduced by 2.2%, and causing surface heating of 4.6 W/m^2. Globally, the radiative forcing at the surface is 0.1 W/m^2. The changes of surface albedo are calculated by using the first year of atmospheric only simulation in which BC emission is increased, therefore the change largely represents the albedo decrease due to BC deposition, although we cannot completely rule out the associated melting during the first year.

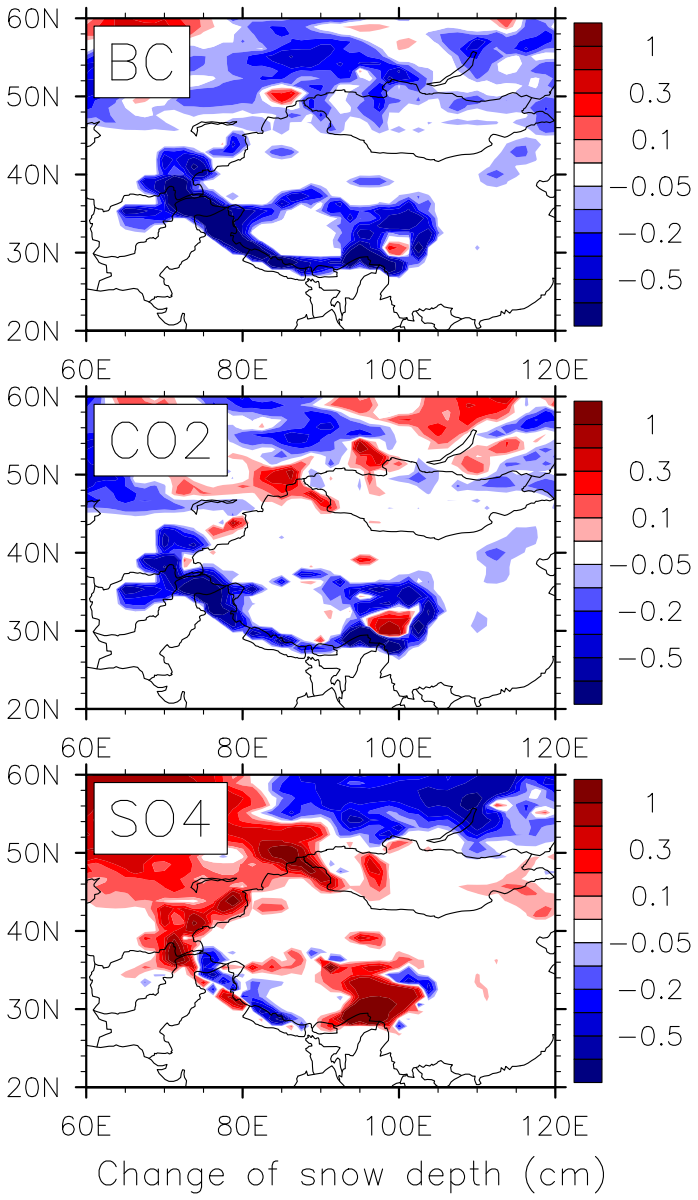

Figure 4.6 Snow depth (water equivalent) change (cm, calculated as the difference of the last 60 year of perturbed simulation and the 319 year long term control) due to three different forcing agents (BC, CO_2, SO_4). The average reduction of snow depth water equivalent Tibet Plateau (30-40°N, 80-100°E) is 0.2 mm, three times larger than that due to CO_2.

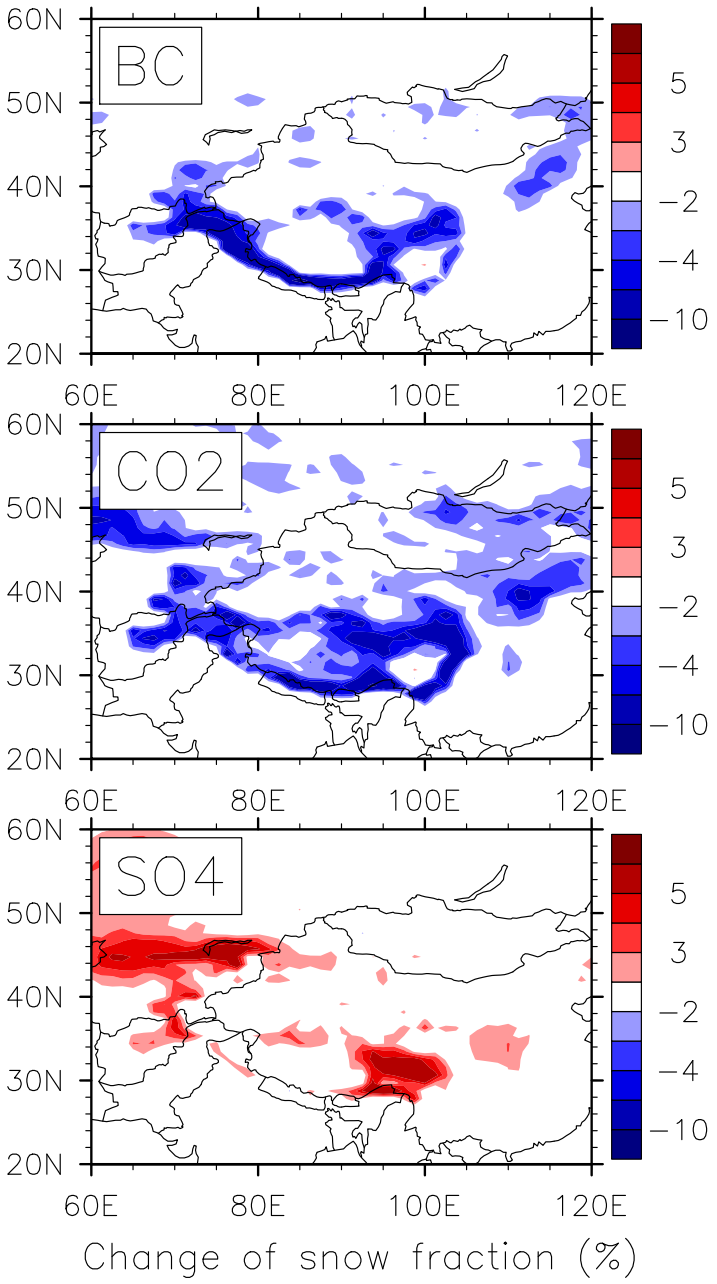

Figure 4.7 (a) The change of snow cover fraction due to present day BC in the simulation. (b) Due to CO_2. (c) Due to SO_4. The regional averaged statistics are shown in Table 4.10.

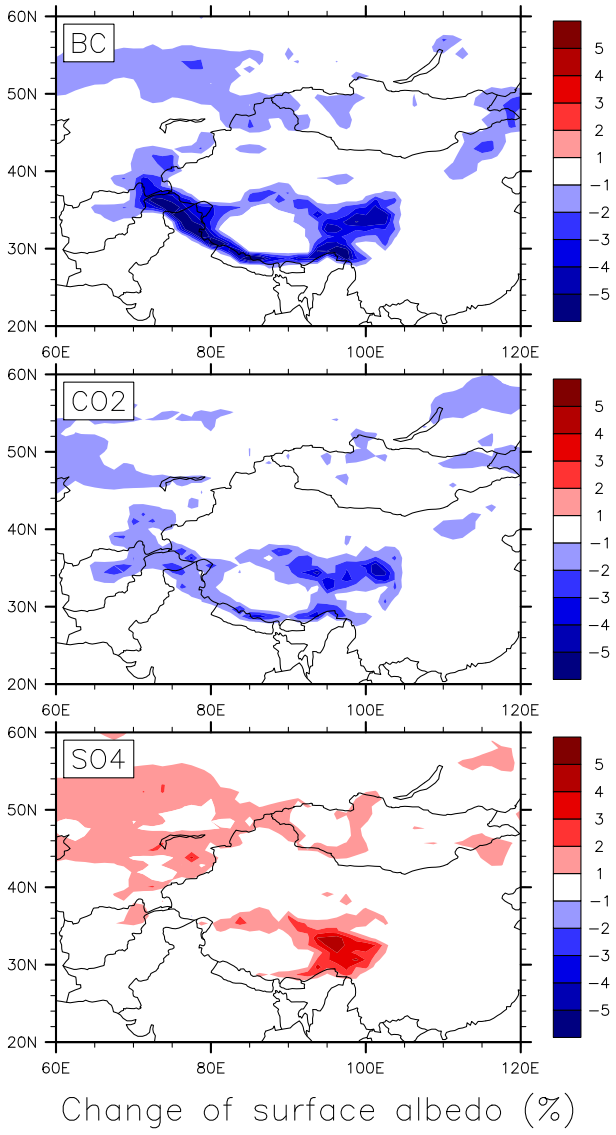

Figure 4.8 Surface albedo (unitless, calculated as the difference of the last 60 year of perturbed simulation and the 319 year long term control) under three different forcing agents (BC, CO_2, SO_4). The average reduction of surface albedo over Tibet Plateau (30-40°N, 80-100°E) is 0.74%, 1.5 times larger than that due to CO_2. Other statistics are shown in Table 4.11.

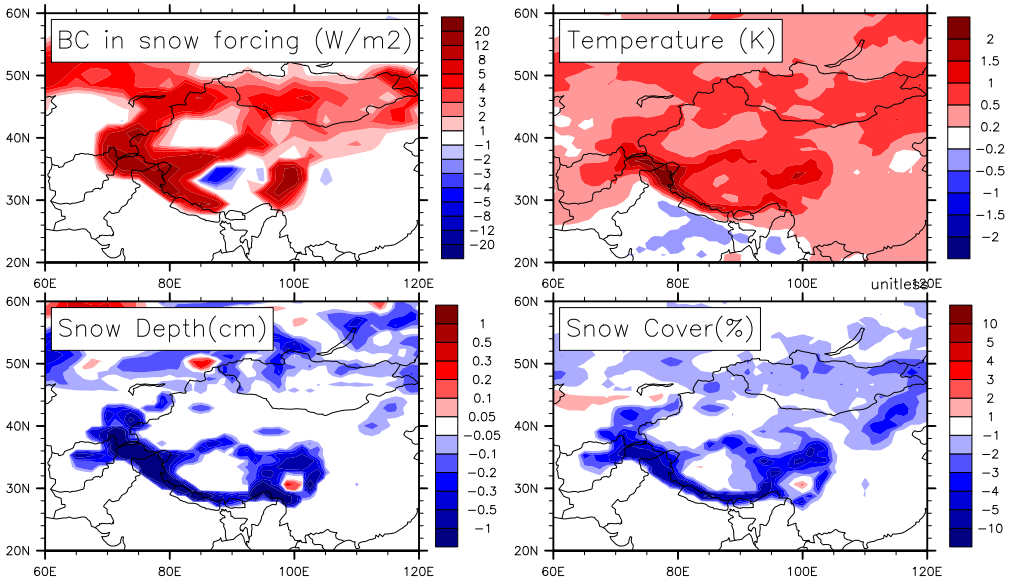

Figure 4.9 (a) Surface shortwave flux change due to surface albedo change, as shown in Figure 4.5(b), and climate responses to BC forcing: (b) Surface temperature; (c) Snow depth, as shown in Figure 4.6(a); (d) Snow cover fraction, as shown in Figure 4.7(a).

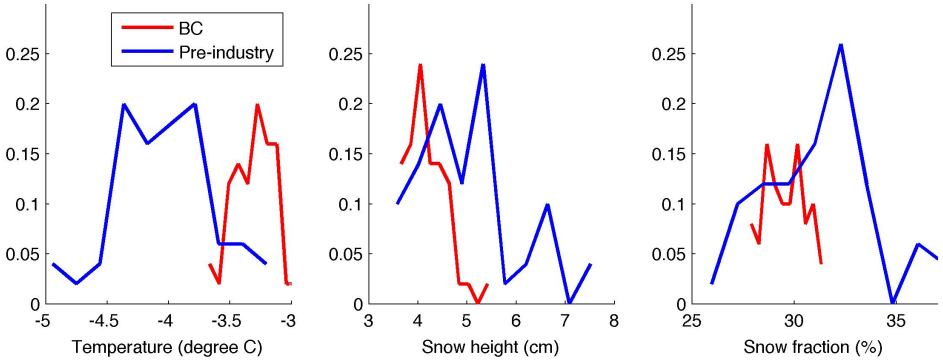

Figure 4.10 Probability distribution functions of annual averaged climate variables over Tibet region (30-40°N, 80-100°E). (a) Surface temperature (b) Snow depth, and (c) Snow cover fraction. The values in the pre-industrial control simulation (blue) and perturbed simulations with BC forcing (red). The probability distribution is calculated with 50 yearlong simulations. The spatial variations of the difference are shown in Figure 4.9 (b)-(d). In response to the increase of BC emission, temperature is increasing by 0.84 (Table 4.2(b)). Snow depth is reduced by 0.2 cm (Table 4.9), and snow fraction is reduced by 1.9% (Table 4.10).

References

Armstrong, R. and Brodzik, M.: Northern Hemisphere EASE-Grid weekly snow cover and sea ice extent version 3. Boulder, Colorado USA, National Snow and Ice Data Center, Digital media, 2005.

Bajracharya, Samjwal Ratna, Pradeep Kumar Mool, and Basanta Raj Shrestha. "Global climate change and melting of Himalayan glaciers." Melting glaciers and rising sea levels: Impacts and implications (2008): 28-46. Environ. Res. Lett. 7 014021 doi:10.1088/1748-9326/7/1/014021.

Bond, T. C. et al. (2013), Bounding the role of black carbon in the climate system: A scientific assessment, J. Geophys. Res. Atmos., 118(11), 5380–5552, doi:10.1002/jgrd.50171. [online] Available from: http://doi.wiley.com/10.1002/jgrd.50171 (Accessed 18 September 2013)

Chung, S. H. and J.H. Seinfeld (2005), Climate response of direct radiative forcing of anthropogenic black carbon, J. Geophys. Res., 110(D11), D11102, doi:10.1029/2004JD005441. [online] Available from: http://doi.wiley.com/10.1029/2004JD005441 (Accessed 18 September 2013)

Flanner, M. G., C. S. Zender, J. T. Randerson, and P. J. Rasch (2007), Present day climate forcing and response from black carbon in snow, J. Geophys. Res., 112, D11202, doi: 10.1029/2006JD008003.

Flanner, M. G., C. S. Zender, P. G. Hess, N. M. Mahowald, T. H. Painter, V. Ramanathan, and P. J. Rasch (2009), Springtime warming and reduced snow cover from carbonaceous particles, Atmos. Chem. Phys, 9, 2481-2497.

Gardner, A. S. et al. (2013), A reconciled estimate of glacier contributions to sea level rise: 2003 to 2009., Science, 340(6134), 852–7, doi:10.1126/science.1234532. [online] Available from: http://www.ncbi.nlm.nih.gov/pubmed/23687045 (Accessed 10 November 2013)

Ghan, S. J., X. Liu, R. C. Easter, R. Zaveri, P. J. Rasch, J.-H. Yoon, and B. Eaton (2012), Toward a Minimal Representation of Aerosols in Climate Models: Comparative Decomposition of Aerosol Direct, Semidirect, and Indirect Radiative Forcing, J. Clim., 25(19), 6461–6476, doi:10.1175/JCLI-D-11-00650.1. [online] Available from: http://journals.ametsoc.org/doi/abs/10.1175/JCLI-D-11-00650.1 (Accessed 22 June 2012)

Gettelman, A., J. E. Kay and K. M. Shell, The Evolution of Climate Sensitivity and Climate Feedbacks in the Community Atmosphere Model, J. Climate 25:5, 1453-1469

Hansen J, Nazarenko L (2004) Soot climate forcing via snow and ice albedos. Proc Natl

Acad Sci USA 101:423–428Kay, J. E. and T. L'Ecuyer (2013): Observational constraints on Arctic Ocean clouds and radiative fluxes during the early 21st century, J. Geophys. Res., 118, doi:10.1002/jgrd.50489.

Kay, J. E. and T. L'Ecuyer (2013): Observational constraints on Arctic Ocean clouds and radiative fluxes during the early 21st century, J. Geophys. Res., 118, doi:10.1002/jgrd.50489.

Kopacz, M., Mauzerall, D. L., Wang, J., Leibensperger, E. M., Henze, D. K., and Singh, K.: Origin and radiative forcing of black carbon transported to the Himalayas and Tibetan Plateau, Atmos. Chem. Phys., 11, 2837-2852, doi:10.5194/acp-11-2837-2011, 2011.

Lawrence, D.M., K.W. Oleson, M.G. Flanner, P.E. Thornton, S.C. Swenson, P.J. Lawrence, X. Zeng, Z.-L. Yang, S. Levis, K. Sakaguchi, G.B. Bonan, and A.G. Slater, 2011: Parameterization improvements and functional and structural advances in version 4 of the Community Land Model. J. Adv. Model. Earth Sys., 3, DOI: 10.1029/2011MS000045.

Lee, W. L., K. N. Liou, and A. Hall, 2011: Parameterization of solar fluxes over mountain surfaces for application to climate models. J. Geophys. Res., 116, D01101, doi:10.1029/2010JD014722 .

Liu, X., Z. Cheng, L. Yan, and Z.-Y. Yin (2009), Elevation dependency of recent and future minimum surface air temperature trends in the Tibetan Plateau and its surroundings, Glob. Planet. Change, 68(3), 164–174, doi:10.1016/j.gloplacha.2009.03.017. [online] Available from: http://linkinghub.elsevier.com/retrieve/pii/S0921818109000642 (Accessed 6 November 2013)

Lu, Z., D. G. Streets, Q. Zhang, and S. Wang (2012), A novel back-trajectory analysis of the origin of black carbon transported to the Himalayas and Tibetan Plateau during 1996–2010, Geophys. Res. Lett., 39, L01809, doi:10.1029/2011GL049903.

Manabe, Syukuro, Richard T. Wetherald, 1975: The Effects of Doubling the CO_2 Concentration on the climate of a General Circulation Model. J. Atmos. Sci., 32, 3–15.

Meehl, G.A., and co-authors, 2012: Climate change projections in CESM1/CAM5. J. Climate, in preparation.

Meehl, G.A., J.M. Arblaster, and W.D. Collins, 2008: Effects of black carbon aerosols on the Indian monsoon. J. Climate, 21, 2869—2882.

Menon, S., D. Koch, G. Beig, S. Sahu, J. Fasullo, and D. Orlikowski (2010), Black carbon aerosols and the third polar ice cap, Atmos. Chem. Phys., 10(10), 4559–4571, doi:10.5194/acp-10-4559-2010. [online] Available from: http://www.atmos-chem-

phys.net/10/4559/2010/ (Accessed 18 September 2013)

Ming, J., Z. Du, C. Xiao, X. Xu, and D. Zhang (2012), Darkening of the mid-Himalaya glaciers since 2000 and the potential causes, Environmental Research Letters, 7(1), 014021.

Ming, Y., V. Ramaswamy, and G. Persad (2010), Two opposing effects of absorbing aerosols on global - mean precipitation, , 37, 1–4, doi:10.1029/2010GL042895.

Painter, T. H., J. Deems, J. Belnap, A. Hamlet, C. C. Landry, and B. Udall (2010), Response of Colorado River runoff to dust radiative forcing in snow, Proceedings of the National Academy of Science.

Painter, T. H., M. G. Flanner, G. Kaser, B. Marzeion, R. A. Vancuren, and W. Abdalati (2013), End of the Little Ice Age in the Alps forced by industrial black carbon, PNAS , doi:10.1073/pnas.1302570110/-/DCSupplemental.www.pnas.org/cgi/doi/10.1073/pnas.1302570110.

Pistone P. I Eisenman, V Ramanathan, (2013). Observational determination of albedo decrease caused by vanishing Arctic sea ice. PNAS. In press.

Qian, Y., Flanner, M. G., Leung, L. R., and Wang, W.: Sensitivity studies on the impacts of Tibetan Plateau snowpack pollution on the Asian hydrological cycle and monsoon climate, Atmos. Chem. Phys., 11, 1929-1948, doi:10.5194/acp-11-1929-2011, 2011.

R. B. Neale, C. Hannay, G. Danabasaglu, D. M. Lawrence, J. E. Kay, M. Holland, A. Gettelman, S. Park, P. J. Rasch, S. Ghan, X. Liu and M Zhang, 2012: Coupled simulations from CESM1 using the Community Atmosphere Model version 5: (CAM5) J. Climate. In preparation.

Ramanathan, V., C. Chung, D. Kim, T. Bettge, L. Buja, J. T. Kiehl, W. M. Washington, Q. Fu, D. R. Sikka, and M. Wild, (2005). Atmospheric Brown Clouds: Impacts on South Asian Climate and Hydrological Cycle. PNAS, Vol. 102, No. 15, 5326-5333.

Ramanathan V., M.V. Ramana, G. Roberts, D. Kim, C.E. Corrigan, C.E. Chung & D. Winker (2007).Warming trends in Asia amplified by brown cloud solar absorption. Nature, 448, 575-578 doi:10.1038/nature06019.

Ramana, M.V., V. Ramanathan, D. Kim, G.C. Roberts and C.E. Corrigan (2007). Albedo, Atmospheric Solar Absorption and Heating rate measurements with stacked UAVs, Quart. J. Roy. Meteor. Soc., 133, 1913-1931.

Santer, B. D. et al. (2013), Identifying human influences on atmospheric temperature., Proc. Natl. Acad. Sci. U. S. A., 110(1), 26–33, doi:10.1073/pnas.1210514109. [online] Available from: http://www.pubmedcentral.nih.gov/articlerender.fcgi?artid=3538189&tool=pmcentrez&rendertype=abstract (Accessed 6 November 2013)

Wang, C., 2004: A modeling study on the climate impacts of black carbon aerosols, J. Geophys. Res., 109,D03106, doi:10.1029/2003JD004084.

Xie, S.-P., B. Lu, and B. Xiang, 2013: Similar spatial patterns of climate responses to aerosol and greenhouse gas changes. Nature Geosci., 6, 828-832, published online 1 September 2013, doi:10.1038/NGEO1931.

Xu, Y., and V. Ramanathan (2012), Latitudinally asymmetric response of global surface temperature: Implications for regional climate change, Geophys. Res. Lett., 39(13), n/a–n/a, doi:10.1029/2012GL052116. [online] Available from: http://doi.wiley.com/10.1029/2012GL052116 (Accessed 18 September 2013)

Xu, B. et al. (2009), Black soot and the survival of Tibetan glaciers., Proc. Natl. Acad. Sci. U. S. A., 106(52), 22114–8, doi:10.1073/pnas.0910444106. [online] Available from: http://www.pubmedcentral.nih.gov/articlerender.fcgi?artid=2790363&tool=pmcentrez&rendertype=abstract

Chapter 5

Assessing black carbon's role in climate change mitigation

Abstract

Black carbon (BC) aerosols have been demonstrated to be an important factor for Asian climate change. The East Asia region is also currently the largest emitter of BC aerosols. Here we used a comprehensive global climate model to evaluate the climate mitigation benefits associated with a rapid reduction of BC aerosols. The regional temperature and snow cover over Tibet is shown to be very sensitive to BC emission control measures. We show that the aggressive BC reduction leads to a significant amount of avoided warming and recovery of snow loss due to ongoing global warming. We further discussed the major sources of BC emissions from China and the potential practical measures to cut BC emissions. As an example, the cost of a specific mitigation measure, cook stove improvement, is calculated and compared against the valuation of climate change mitigations benefits, which are in terms of (1) the delaying of global mean warming and (2) the reduced mortality of local population.

5.1 Introduction

Assessing the future climate impact of controlling BC and other short-lived climate pollutants (SLCPs) will have important societal significance. Ramanathan and Xu (2010) identified three avenues by which major greenhouse gas-emitting countries can

avoid reaching the warming threshold of 2°C, a point beyond which climate change will present unmanageable negative consequences for society. The recommended avenues are summarized as the following: 1) Decrease the rate of thickening of the blanket of GHGs: Stabilize CO_2 concentration below 441 ppm. 2) Offset the addition of radiant energy resulting from the reduction of aerosol cooling: Reduce BC and ozone concentrations. 3) Thin the GHG blanket: Reduce emissions of methane and HFCs. The central idea behind the proposal in Ramanathan and Xu (2010) is that these steps to cut CO_2 and other short-lived climate pollutants must be taken simultaneously to avoid the 2-degree warming threshold, and carbon dioxide control alone is not sufficient. Compared to the "Herculean" effort of decarbonizing the energy sector to sufficiently reduce CO_2 emissions, reducing other climate warming factors is the low-hanging fruit with available technology and policy. If action is taken immediately, society will have more time to develop and scale up clean energy and other technologies to stabilize and mitigate CO_2 concentrations. Similar proposals have been raised by other groups, focusing on one or more SLCPs (Jacobson et al., 2010, Kopp et al., 2010, Molina et al., 2009).

Climate science research has provided emerging evidences that BC as one of the SLCPs plays a major role in global (temperature and sea level rise) and regional climate change (Ramanathan and Carmichael, 2008). The observed tropical expansion (Allen et al., 2012) and hurricane frequency over India Ocean (Evan et al., 2011) have been linked with anthropogenic aerosols, in particular BC. For the climate in China, BC is suggested to contribute to the observed pattern of the flooding in the south and the drought in the north (Menon et al., 2002).

Here we use a state-of-the-art NCAR GCM with a newly updated aerosol

chemistry treatment to evaluate the potential climate mitigation benefits from aggressive BC reduction. The emission inventories under different scenarios (business-as-usual, aggressive regulation) are adopted from the Representative Concentration Pathway database. The database is widely used by modeling groups for IPCC AR5 model inter-comparisons.

5.2 Methods

5.2.1 Major sources of BC emissions in China

The major sources of BC emission in East Asia include: industry, biofuel combustion and open-biomass burning. Bond et al., (2007) is still the most updated global BC emission database and used in Representative Concentration Pathway (RCP) database. Regional BC emission inventories in China have been developed by different groups (see a summary in Table 5.1). Streets et al. (2001) comprehensively studied China's BC emissions. Cao et al. (2007) provided BC emission estimates using local source of data in energy use and emission factors. The most recent study (Zhang et al., 2009) estimated that China's share in Asian energy-related BC emissions was over 60% in 2006. According to these studies, the sources of BC in China are mainly energy-related (coal combustion), and thus could be more pronounced in radiative effect due to a higher BC/OC ratio compared with emissions from biomass burning.

China is the largest emitter of BC (1500 Gg out of 8000 Gg global value, Bond et al., 2004). The major sources of BC (Figure 5.1; Cao et al., 2008; Bond et al., 2004) are transportation sector (diesel trucks, off-road vehicles), residential sector (biomass and coal burning for cooking and heating), agriculture (rural combustion of crop residues)

and small industrial sectors (raw coal combustion). We will mainly focus on residential sector in the analysis of section 4 because: a) Residential sector accounts for more than half of the emission (Figure 5.1). b) China had the experience from 1980s to 1990s of improving rural cooking conditions. c) The analysis of residential sectors can be directly applied to other developing countries in South Asia, Southeast Asia, and Africa.

The methodology adopted by different groups to develop BC inventory are similar. BC emission is mainly due to incomplete combustion of carbonaceous matter. The anthropogenic sources are most energy-related. In general, energy uses are divided into several main sectors (industry, residential, and transportation), and divided further based on fuel type (coal, diesel, gas, firewood, crops) and combustion technology (traditional, improved); thus, BC emissions can be segregated into more than one hundred source classifications. Emissions in each source classification are estimated as the following: Fuel use (ton)* emission factor (kg/ton) = emission (kg). Data sources for fuel use (energy activity) include: International Energy Agency, China National Bureau of Statistics, China State Environment Protection Administration. Emission factors are reported from controlled combustion experiments and local in-situ observations, but are subject to large uncertainty due to inadequate measurements.

5.2.2 Model simulations

The model we used in this study is Community Earth System Model 1 (CESM1) developed at National Center for Atmospheric Research (NCAR), Department of Energy, and university scientists. CESM1 is a coupled model with atmospheric and land components of CAM5 and CLM4 (Neale et al., 2013; Lawrence et al., 2012). CESM1 climate simulations have been documented extensively (Meehl et al., 2013). The

anthropogenic forcing in CESM1 include time-evolving GHGs, as well as prescribed time- and space-evolving concentrations of tropospheric ozone, stratospheric ozone, the direct effect of sulfate aerosols and black and primary organic carbon aerosols (Lamarque et al., 2011). The 3-mode modal aerosol scheme (MAM3) has been implemented and provides internally mixed representations of number concentrations and mass for Aitken, accumulation, and course aerosol modes.

In Chapter 2, we have conducted a model sensitivity test to calibrate the model with observation-based estimates. We show that the current emission inventory used in the standard model is too low compared with observations, and a factor of 3 to 4 adjustment is needed to make the simulated atmospheric forcing agree with observational estimates. In Chapter 3, we used the improved model to assess global and regional climate change response to global increase of BC from pre-industrial to present-day level, with a focus on Tibet warming and glacier retreat. Our results in Chapter 4 suggest that present-day BC is very influential in causing the mountain glacier retreat over Tibet and Himalaya regions. The comparative simulations, in which CO_2 and SO_4 are instantaneously increased from pre-industrial level to present-day level, suggest that the contribution of CO_2 is even less than that from BC for Tibet region, despite a much larger global influence from CO_2.

In this chapter, our objective is to test the impact of rapid BC reduction over China to see if the impact signals emerge from the climate noise. We also put the impact in context with global emission reduction and India emission reduction to look at the relative contribution from each region. We reduce the year 2000 emission back to zero to test the reversibility of response, namely to test whether the climate system can respond

to such a rapid reduction of emission quickly.

We first run the year 2000 control simulation for 75 years. There is a slight warming trend during the 75-year "control" simulation due to the energy imbalance at the top of the atmosphere (TOA). In another three sets of simulation, we branched from the year 2000 control simulations but decrease the emission of BC in 25 years (from Global sources, from East Asia sources and from South Asia sources) to zero. The first 25-year is considered model spin-up period. We average the model output of year 26 to year 75. The difference between the year 2000 control run (in which BC emission is kept at current level) and the mitigation run (in which BC emission is aggressively reduced to zero) is calculated as the benefits of climate mitigation.

In Chapter 4, we have demonstrated the pre-industrial to present-day BC emission increase has tremendous impact on global and regional climate change. The global and regional warming of Asia is significant. In addition, the elevated warming over Tibet causes significant glacier retreat.

The simulations discussed in this chapter provide additional insights. (1) We want to test the climate reversibility following aggressive reduction of BC. Similar simulation to test the reversibility of climate in response to extraction of CO_2 from atmosphere have been carried out, in which the CO_2 concentration is rapidly reduced to the pre-industrial level. (2) Another objective of the simulation discussed in this chapter is to look at the relative contribution to climate change from specific regions (e.g. China or India). The linearity of emission on climate impact remains to be tested with comprehensive model such as CESM1, and this piece of information is relevant to the policy-making process.

However, since the global response to BC increase as we have shown in Chapter

2 is not very large and a multiple ensemble of simulation for very long time periods is needed to seperate the signal from the noise (Tebaldi and Friedlingstein, 2013). Therefore, in this chapter, we took an aggressive approach to reduce BC to zero to test the climate system sensitivity. We note that we take an extreme case in which the emission of BC is reduced to zero and this scenario may be too aggressive and unrealistic. We will further discuss the approaches and cost-benefits associated with BC reduction in section 4.

5.3 Climate mitigation through BC reduction

We do note here that the global emission increase of BC aerosols can lead to significant impact to regions far away from sources (e.g. Arctic (Figure 5.2) and Western North America (Figure 5.3)). For example, the sea ice concentration and sea ice thickness is greatly reduced over Arctic region, as well as the snow depth over sea ice. The spatial pattern of sea ice loss due to BC forcing is similar to that due to CO_2 but with smaller magnitude (Figure 5.3). Over North America regions, our simulations also indicate that BC forcing is responsible for the precipitation reduction of 5% to 20% in the Western states (Figure 5.3). The precipitation response to CO_2 and SO_4 show different pattern that largely cancel each other. Since the continuing drought of Southwestern states have raised many concerns of water resources, further studies in attributing the observed trends into various forcing factors as well as natural variability is greatly needed.

Here following the discussion of Chapter 4, in this chapter we will mainly focus on Tibet warming and Himalaya glacier retreat. In response to global reduction of BC, the global mean temperature is reduced by 0.15 K from the BAU simulations. Note that

due to climate inertia following 2000 CO_2 emission, the global mean temperature in all cases is increasing. Therefore, the cooling we discussed here is actually "avoided warming."

In terms of latitudinal distribution of "avoided warming", the Northern hemisphere is cooling by more than 0.2 °C and Southern Hemisphere cooling is negligible. The cooling is smaller by one-third than the warming we calculated in Chapter 3 due to pre-industrial to present day emission increase, despite that the emission reduction in this simulation is larger. The contribution from East Asia and South Asia are both too small to pass the statistical test. Eastern China is cooled by 0.2 °C with most of contribution from China emission reduction; India contribution is negligible. The warming over Tibet and Western China is reduce by 0.9 °C. As we discussed in Chapter 3, the Tibetan plateau is one of regions most likely be affected by BC aerosols. Our simulations here demonstrate that aggressive reduction in BC emission can indeed reduce the warming trend over Tibet by a significant amount over a 50-year period. The contribution from East Asia aerosols is about 36% and contribution from South Asia aerosols is about 47%. East Asia is cooling by 0.2 °C with most of the contribution from aerosols in that region.

With respect to precipitation, BC emission control increases the global mean precipitation by 0.7 cm, with similar contribution from China and India. This is in contrast to the slight reduction of global mean reduction due to increase of BC emission from pre-industrial level to present day level. The hemispheric response of BC reduction is also reversed with the precipitation shifted towards the Southern Hemisphere, in both the East Asia reduction and South Asia reduction cases. The regional response of

precipitation is more difficult to understand and the results might be influenced by the model uncertainties. For example, India precipitation is decreased by 1.4 cm in the global BC reduction case, but we witness an increase in both East Asia and South Asia reduction cases. Because the limitation of spatial resolution and precipitation physics, we cannot place much confidence in the simulations.

Following the discussion in Chapter 3, we here also focus on Tibetan glacier retreat. The Tibetan snow depth on average is reduced by 0.3 cm, with 0.1 cm contribution from East Asia aerosol and 0.2 cm from South Asia aerosols. As a result, the surface albedo over Tibet increases by 1.6%, with 0.3% contributed by East Asia aerosols and 0.8% contributed by South Asia aerosols. East Asia surface albedo also increases by 0.4% with half of the contributions from East Asia.

5.4 Discussions relevant to policy

5.4.1 How to reduce BC emission from China

Effective measures to reduce BC emission in China also include: (1) For urban residential sources: cleaner fuels (with processed-coal or electricity should be used to replace coal burning practice. In addition, China should regulate unprocessed-coal burning. (2) For rural residential sources: clean-burning biomass stoves with higher burning efficiency can be used to replace traditional cook stoves. A pilot program in promoting such kind of advanced cook stove is being carried out over India (Project Surya). Modern facilities that convert biofuel to biogas are also desirable but may require more labor effort. (3) For transportation sources: diesel particle filters can be enforced to install on heavy-duty trucks and off-road vehicles. In addition, cleaner fuels including

burning of natural gas, electricity powered cars should also be promoted. (4) For industrial sources: Higher emission standard for small coal- burning power plants, cokes ovens, and brick kilns. Enforce stronger small business regulation; (5) For agriculture sources: we could impose stronger regulation or ban open burning of agricultural waste.

The potential control plan on BC emission includes the following: installing diesel engine filters to reduce transportation-related emissions; upgrading biofuel cook stoves to improving combustion efficiency; switching biofuel to biogas; banning open burning of crop residuals; regulating unprocessed-coal burning for residential and small business use.

5.4.2 Cost of cutting emission from cook stove

As we have discussed, there are multiple mechanisms through which the BC reduction over China is feasible. However, up to now, China has been reluctant in acting in BC reduction and climate change mitigation in general. A subset of the larger question of how to get China engaged is whether addressing short-lived climate pollutants (SLCPs), including black carbon, methane, halo carbons, ozone) would change China's interest in joining international cooperation combating climate change.

As an example in this paper to demonstrate the feasibility of BC reduction plan, we proposed to cut residential emission sources by 2/3 at the year of 2050 from its current level (2005 as baseline year) through an intensive "cook stove upgrade plan" and examine the cost and benefits associate with this hypothetical plan. The analysis here can also be applied to other sources of BC or other SLCPs.

The 2/3 BC reduction from China's residential emission (500 Gg reduction) would be a significant contribution to the larger global goal of cutting BC emission by

half at 2050 (UNEP, 2011). In the next sections, we will analyze the cost and benefit for this plan. The costs associated with the emission control are from two categories, technological transfer and regulatory measures. The benefits of emission control include: energy savings from the improvement of combustion efficiency, mitigation of the climate change, reduction in the air pollution, and the improvement of public health. The cook stove upgrade plan includes two types of strategies to reduce emission. a) Switching fuel from biomass to biogas or LPG, and from lump coal-to-coal briquettes. b) Upgrading cook stoves to improve combustion efficiency. The cost in implementing such a massive upgrade plan is difficult to estimate. Here we adopted the empirical values from literature assessments. Amann et al. (2008) estimated that the cost range from -$6 to $7 per ton of CO_2 equivalent for biomass cook stove and 0$ for coal cook stove. The negative costs are due to accounting for immediate benefits of energy saving from increased combustion efficiency. Bond and Sun (2005) gave the estimates of $2-11 per ton of CO_2 equivalent (using 20-year time frame). The program is almost cost-neutral even without considering the external benefits of climate change and public health. However, due to high risk factor, initial subsidies and financing mechanisms are required to offset the upfront payment for switching fuel and upgrading stoves. Following the converting factor of BC emission to CO_2eq in section 2.2, the total costs associated with 500 Gg annual emissions are estimated to be less than 1.5 billion USD at 2050.

5.4.3 Climate benefits from BC reduction

Figure 5.5 illustrated the approaches to evaluate the benefits of BC emission reduction. We first started with the calculation of benefits from reducing global emission by half. According to current estimates of radiative forcing from various methods based

on climate model and satellite observations, a 50% reduction will reduce radiative forcing by 0.5 W/m^2. Following the energy balance model used in Ramanathan and Xu (2008), we estimated that such a forcing reduction would avoid 0.15 K warming at 2050. Considering that the threshold of global warming is 2 K (relative to pre-industrial, namely 1.2 K relative to 2005 mean temperature), an avoided warming of 0.15 K can be a significant contribution. Combined with other SLCP control measures, the likelihood of exceeding the threshold at mid-century will be decreased (Shindell et al., 2012).

Previous valuations of climate change are mainly focusing on GHGs including CO_2, and the concepts of "social cost of carbon" are widely used to quantify the external costs of carbon emission (or external benefits of carbon emission reduction). Here we used a carbon cycle model (Joos et al., 1996) to show that 0.15 K avoided warming will be equivalent to 2.5 Gt CO_2 emission reduction (current global CO_2 emission is about 30 Gt). If adopting $266/ton carbon as "social cost of carbon" (Tol et al., 2008), the external benefits of cutting global BC emission is estimated to be 180 billion US dollars (current value without considering inflation) per year at the year of 2050.

The proposed cook stove upgrade plan in China will contribute 500-Gg BC reductions to the total 4000-Gg global targets, so we estimated its benefits to be 22.5 billion USD. We need to emphasize that the estimation here has not been taken into account BC's impact on regional climate in China (perturbing regional rain fall pattern, influencing glacier retreat) and therefore may significantly underestimate the climate benefits.

5.4.4 Benefits to public health

Particles smaller than 2.5 um (PM2.5, including BC particles) have strong

negative impact on human health. The chemical transport model simulation (Carmichael, 2009) suggested that PM2.5_BC loading in China is as high as 2 microgram/m^3 in metropolitan regions, and PM2.5_OC (organic carbon) is about 5 microgram/m^3. Since BC emission reduction will also simultaneously reduce co-emitted organic carbon aerosols, we roughly estimate that 500 Gg BC emission reduction from cook stove improvement program will lead to a decrease of PM2.5 concentration by 2.3 microgram/m^3 at the year of 2050. According to the public health concentration-response model (Anenberg et al., 2012), a decrease of pollution concentration will have enormous health benefits and reduce mortality rate by 2.5%. Considering the projected population growth (UNEP, 2010) and mortality rate (World bank, 2010) at 2050, 2.5% decrease of mortality rate will reduce 200k premature death by then. According to the "valuation of a statistic life" concept (EPA, 1999), and taking into account the income level difference between China and Western world (worldsalaries.org), the benefits of avoiding 200k premature deaths will contribute about 800 billion USD. This estimation is based on ambient PM2.5 concentration from model simulations, and due to limited data sources, the health impact of indoor pollution that is more directly caused by residential emission are not considered here. Inclusion of the indoor pollution into this analysis may significantly increase the estimated benefits.

5.5 Concluding remarks

Top-down engagements from China central government are still not observed, despite the huge potential benefits (23 billion USD from climate change mitigation and 800 billion from public health) and relatively lower cost (less than 1.5 billion). China

joined the Global Alliance for Clean Cook stoves in May 2012. The national assessment on SLCP is not available, and it is not clear if China will join the effort of Climate and Clean Air Coalition to Reduce SLCPs. Scientists from China Meteorology Agency (Zhi et al., 2009) remarked that China should pay special attention to BC emission reduction, but the implementation of emission control should mainly served for public health but not climate change, given the uncertainties in sciences and the international pressure that China may encounter. Another possible explanation for why the central government is reluctant in addressing SLCP issue is that high-level regulations on provincial and local activities (e.g. residential and small business sectors) are not easy. Therefore bottom-up approaches through NGO and social media to promote grass root activities and increase the public awareness are highly desired.

Next, we discuss future research direction that is helpful for scientific understanding of BC's climate impact and policymaking. In assessing BC's effect on delaying global warming, a fundamental quantity that can give us critical insight is the rate of change of ocean heat content (OHC) with time, which is an indicator of disequilibrium of Earth's input and outgoing energy. Since the 1960s, OHC has been measured with sufficient accuracy, especially after 2000 due to a comprehensive float observational network. From the simulation results of the simple energy balance model, the OHC trend shows a reversal from positive to negative in 2030, within two decades after the mitigation actions begin, and before the temperature trend shows a reversal. If 3-dimensional climate models can verify this finding, the time rate of change of OHC would prove to be a powerful diagnostic for evaluating the success of mitigation actions. In addition to global mean temperature and OHC, future study with a 3-dimensional

coupled climate model will enable us to understand potential consequences on a regional scale. Focusing on East Asia, the monsoon variability and associated precipitation change will be carefully assessed.

In this chapter, we only discussed the relative contributions from different regions (China vs India). One piece of information that is more relevant to policy making in the future breakdown of contributions to individual sectors. The difficulty in further attributing climate change to emissions from individual sectors is that the signal-to-noise ratio in the climate model is too low because of large internal climate variability. Therefore, we cannot place much confidence in the climate response due to emissions from specific sectors. Although the benefits on climate change due to emission reduction in individual sectors is difficult to isolate with global climate model, we can use higher resolution regional chemistry model to calculate the atmospheric loading of aerosol and assess the benefits associated with public health.

Therefore, after the climate simulation results are obtained for 2050, we can use them as a boundary condition to run the high-resolution regional climate model (WRF, Weather Forecast Research model). With the proper model downscaling techniques, we can obtain a more detailed picture of climate change, such as extreme weather events and extreme pollution events, and map those events to population distribution to assess human exposure and risks. The impact of BC will also be compared with mitigation measures targeting CO_2 and other SLCPs. The impact assessment and cost-benefit analysis, which may result from my study, will provide useful information for East Asian policy makers.

In this chapter, we only roughly valuated the costs and benefits associated with

one type of BC reduction measures – cook-stove improvement. In future study, we will also analyze the cost and benefits of various measures to propose a technologically feasible emission control plan. For example, we can estimate the cost of legislation to ban open burning of crop residuals. The capital required to implement crop-to-methane devices in rural areas can be secured through a tax in surrounding cities, which will benefit from less pollutions. In addition, the rural residents receive further incentives when using methane for cooking and heating. The cost-and-benefit of BC emission control can be compared with CO_2 and other SLCPs, and provide valuable information for policymakers in East Asia.

Tables

Table 5.1 Emission inventory (emission per area, units: $1e^{11}$ molecule carbon/cm2/s) used in CESM model simulations (updated from Bond et al., 2004).

	Agriculture Waste	Domestic	Energy	Industry	Shipping	Transportation	Waste	Total
Global	0.02	0.29	0.01	0.22	0.02	0.19	0.01	0.74
NH	0.04	0.46	0.02	0.51	0.04	0.44	0.01	1.52
SH	0.01	0.01	0	0.02	0	0.03	0	0.06
Tibet	0	0.11	0	0.11	0	0.01	0	0.23
India	0.06	4.83	0.06	1.57	0.03	1.18	0.03	7.77
China	0.35	4.44	0.12	5.81	0.03	0.97	0.07	11.79
US	0.03	0.23	0.02	0.4	0.04	0.91	0.01	1.65
Brazil	0.03	0.04	0	0.06	0	0.1	0	0.23

Table 5.2 Temperature changes over various regions in response to BC reduction globally or from East Asia or from South Asia.

TS (K)	BC	BC-E Asia	BC-S Asia
Global	-0.1	0.0	0.0
NH	-0.2	0.0	0.0
SH	0.0	0.0	0.0
Tibet	-0.9	-0.3	-0.4
E China	-0.2	-0.2	0.0
India	-0.1	0	-0.1

Table 5.3 Precipitation change over various regions in response to BC reduction globally or from East Asia or from South Asia. The percentage change relative to climatology is shown in parentheses.

Precipitation (cm)	BC	BC-E Asia	BC-S Asia
Tibet	-1.0 (-1%)	-0.4 (-1%)	-0.4 (-1%)
E China	-1.3 (-1%)	-0.6 (-1%)	-1.2 (-1%)
India	-1.4 (-1%)	-0.3 (0%)	-0.9 (1%)

Table 5.4 Snow depth change (cm) over various regions in response to BC reduction globally or from East Asia or from South Asia. The percentage change relative to climatology is shown in parentheses.

Snow depth (cm)	BC	BC-E Asia	BC-S Asia
Tibet	0.26 (39%)	0.03 (5%)	0.15 (23%)
E China	0.03 (30%)	0.01 (10%)	0.0 (0%)
India	0.02 (67%)	0.0 (0%)	0.02 (67%)

Table 5.5 Surface albedo change (%) over various regions in response to BC reduction globally or from East Asia or from South Asia. The percentage change relative to climatology is shown in parentheses.

Surface albedo (%)	BC	BC-E Asia	BC-S Asia
Tibet	1.58 (5%)	0.34 (1%)	0.8 (3%)
E China	0.43 (3%)	0.2 (1%)	0.04 (0%)
India	0.07 (1%)	0 (0%)	0.06 (1%)

Figures

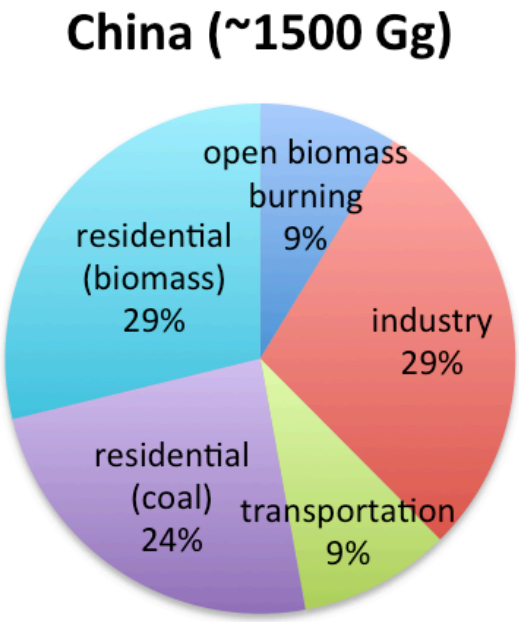

Figure 5.1 China BC emissions from various sectors. Date sources are from Bond et al., (2004) and Cao et al. (2008).

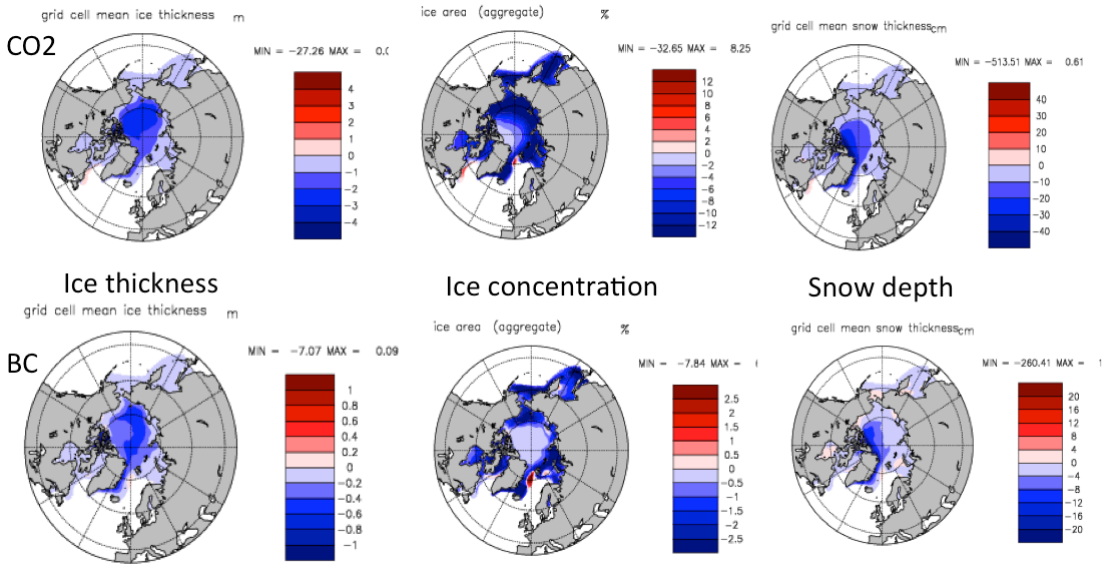

Figure 5.2 The sea ice and snow changes over Arctic in response to CO_2 and BC.

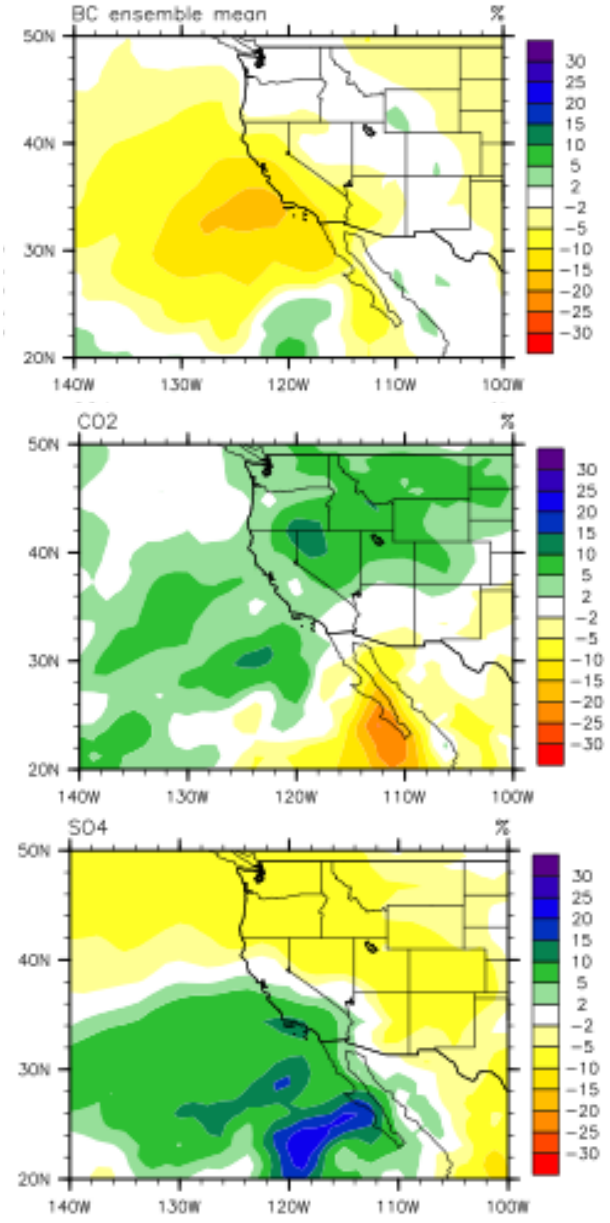

Figure 5.3 The change of precipitation relative to climatology (%) over Western US in response to BC, CO_2 and sulfate aerosols.

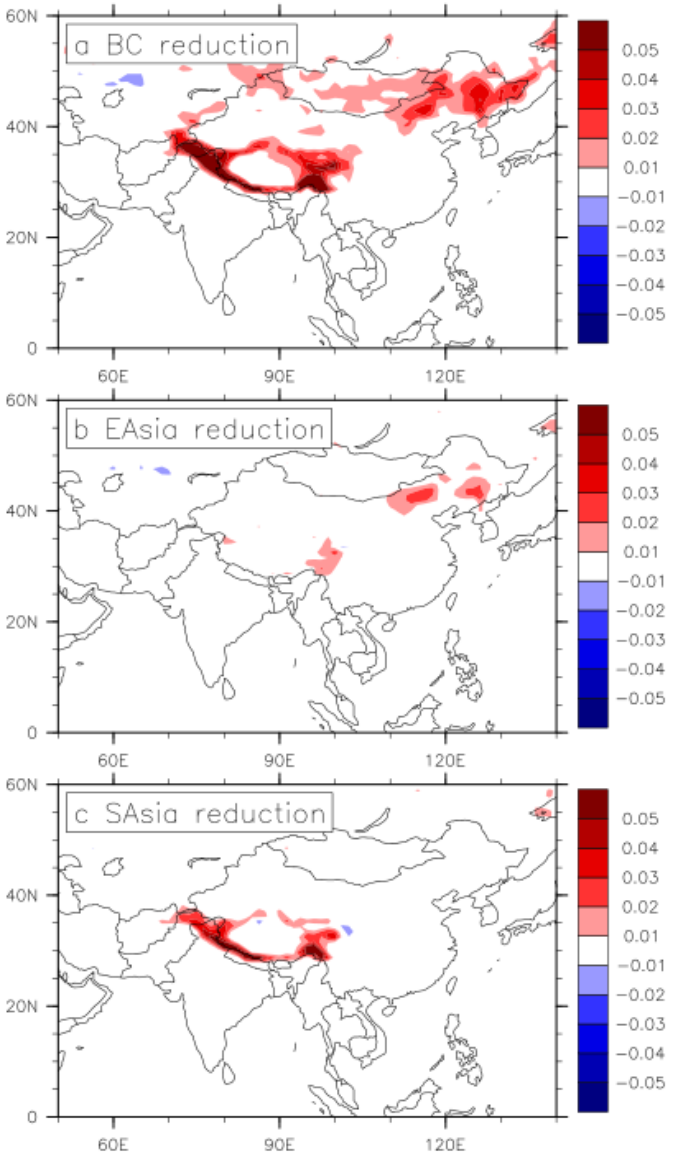

Figure 5.4 Surface albedo increase following BC reduction (a) globally, (b) from East Asia, (c) from South Asia.

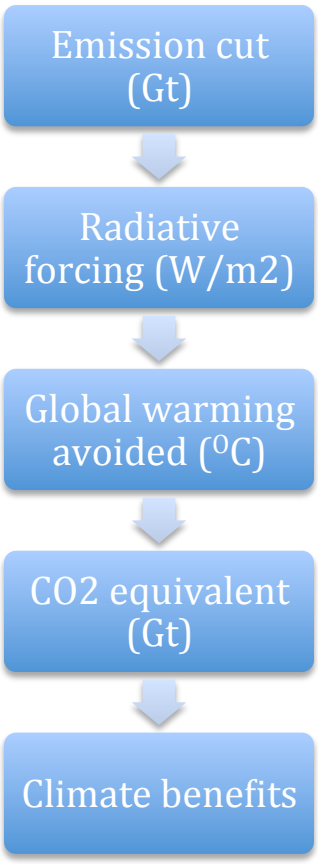

Figure 5.5 Schematics showing the approaches to estimate climate benefits of cook stove upgrade plan.

References

Allen, R. J., and S. C. Sherwood (2010), Aerosol-cloud semi-direct effect and land-sea temperature contrast in a GCM, Geophys. Res. Lett., 37, L07702, doi:10.1029/2010GL042759.

Amann, M., et al. (2008). GAINS ASIA: Scenarios for Cost-effective Control of Air Pollution and Greenhouse Gases in China. IIASA Policy Report. IIASA, Laxenburg, Austria.

Anenberg, S.C., et al. 2012: Global air quality and health co-benefits of mitigating near-term climate change through methane and black carbon emission controls. Environ. Health Perspect., in press.

Bollasina, M., and S. Nigam (2009), Absorbing aerosols and pre-summer monsoon hydroclimate variability over the Indian subcontinent: The challenge in investigating links, Atmos. Res., 94, 338–344.

Bollasina, M., S. Nigam, and K.-M. Lau (2008), Absorbing aerosols and summer monsoon evolution over South Asia: An observational portrayal, J. Clim., 21, 3221–3239

Bond, T. C., D. G. Streets, K. F. Yarber, S. M. Nelson, J.-H. Woo, and Z. Klimont (2004), A technology-based global inventory of black and organic carbon emissions from combustion, J. Geophys. Res.,109, D14203.

Bond, T.C. et al. (2007) Historical emissions of black and organic carbon aerosol from energy-related combustion, 1850–2000. Global Biogeochemical Cycles 21, 1-16

Cao, G., Zhang, X., & Zheng, F. (2006). Inventory of black carbon and organic carbon emissions from China. Atmospheric Environment, 40(34), 6516-6527.

Carmichael, et al. (2009). Asian aerosols: current and year 2030 distributions and implications to human health and regional climate change. Environmental science & technology, 43(15), 5811-7.

Chen, W.T., Y.H. Lee, P.J. Adams, A. Nenes, and J.H. Seinfeld, Will BC mitigation dampen aerosol indirect forcing?, Geophys. Res. Lett., 37 (L09801), doi:10.1029/2010GL042886, 2010.

Collier, J. C., and G. J. Zhang (2009), Aerosol direct forcing of the sum- mer Indian monsoon as simulated by the NCAR CAM3, Clim. Dyn., 32, 313–332, doi:10.1007/s00382-008-0464-9.

Gautam, R., N. C. Hsu, K.-M. Lau, S.-C. Tsay, and M. Kafatos (2009), Enhanced pre-

monsoon warming over the Himalayan-Gangetic region from 1979 to 2007, Geophys. Res. Lett., 36, L07704, doi:10.1029/ 2009GL037641.

Jacobson, M.Z.: Short-term effects of controlling fossil-fuel soot, biofuel soot and gases, and methane on climate, Arctic ice, and air pollution health, J. Geophys.Res.,115, D14209, doi:10.1029/2009JD013795, 2010.

Joos F, et al. (1996) An efficient and accurate representation of complex oceanic and biospheric models of anthropogenic carbon uptake. Tellus Series B: Chemical and Physical Meteorology 48:397–417

Kloster S, Dentener F, Feichter J, Raes F, Lohmann U, Roeckner E, et al. 2009. A GCM study of future climate response to aerosol pollution reductions. Clim Dyn 10.1007/s00382-009-0573-0.

Koch D, Menon S, Del Genio A, Ruedy R, Aleinov I, Schmidt GA. 2009. Distinguishing aerosol impacts on climate over the past century. J Climate 22: 2659-2677.

Koch, D., and A. Del Genio (2010), BC semi-direct effects on cloud cover: review and synthesis, Atmos. Chem. Phys., 10, 7685-7696.

Lau, K. M., et al., 2010: Enhanced surface warming and accelerated snow melt in the Himalayas and Tibetan Plateau induced by absorbing aerosols, Environ. Res. Lett., 5, 025204.

Lau, W. K. M., and K.-M. Kim, 2010: Fingerprinting the impacts of aerosols on long-term trends of the Indian summer monsoon regional rainfall, Geophys. Res. Lett., 37, L16705, doi:10.1029/2010GL043255.

Lau, W. K.M., M. K., Kim, K. M. Kim, and W.S. Lee, 2010: Enhanced surface warming and accelerated snowmelt in the Himalayas and Tibetan Plateau induced by absorbing aerosols. Environ. Res. Lett., 5, doi: 10.1088/1748-9326/5/2/025204.

Levy H, Schwarzkopf MD, Horowitz L, Ramaswamy V, Findell KL. 2008. Strong sensitivity of late 21st century climate to projected changes in short-lived air pollutants. J Geophys Res 113, D06102: doi:10.1029/2007JD009176.

Liu Y, Sun JR, Yang B (2009a). The effects of BC and sulphate aerosols in China regions on East Asia monsoons. TELLUS SERIES B-CHEMICAL AND PHYSICAL METEOROLOGY Volume: 61, Issue: 4 Pages: 642-656.

Manoj, M.G., Devera, P.C.S., Safai, P.D. (2010) Absorbing aerosols facilitate transition of Indian monsoon breaks to active spells. Climate Dynamics. DOI 10.1007/s00382-010-0971-3

Nigam, S., and M. Bollasina (2010), “Elevated heat pump” hypothesis for the aerosol-monsoon hydroclimate link: “Grounded” in observations?, J. Geophys. Res., 115,

D16201, doi:10.1029/2009JD013800.

Ramanathan, V. and G. Carmichael (2008). Global and regional climate changes due to black carbon. Nature Geoscience, 1, 221-227.

Ramanathan, V., Xu, Y (2010). The Copenhagen Accord for limiting global warming: Criteria, constraints, and available avenues. Proceedings of the National Academy of Sciences of the United States of America, 107(18), 1-8.

Randles, C. A., and V. Ramaswamy (2008), Absorbing aerosols over Asia: A Geophysical Fluid Dynamics Laboratory general circulation model sensitivity study of model response to aerosol optical depth and aerosol absorption, J. Geophys. Res.,

Shindell, D., and G. Faluvegi, 2009: Climate response to regional radiative forcing during the twentieth century. Nature Geosci., 2, 294-300, doi:10.1038/ngeo473.

T. C. Bond and H. Sun (2005) Can Reducing Black Carbon Emissions Counteract Global Warming? Environmental Science and Technology, 39, 5921-5926.

Tebaldi, C., & Friedlingstein, P. (2013). Delayed detection of climate mitigation benefits due to climate inertia and variability. Proceedings of the National Academy of Sciences, 110(43), 17229-17234.

Tol, R. S. J. (2008). The Social Cost of Carbon: Trends , Outliers and Catastrophes, 2, 0-23.

United Nation Environment Program. (2011). Integrated Assessment of BC and Tropospheric Ozone. http://www.unep.org/dewa/Portals/67/pdf/Black_Carbon.pdf

USEPA, "The Benefits and Costs of the Clean Air Act: 1990 - 2010. EPA Report to Congress" (Office of Air and Radiation, Office of Policy, Washington, DC, 1999).

Wang C, Kim D, Ekman AML, Barth MC, Rasch PJ. 2009. Impact of anthropogenic aerosols on Indian summer monsoon. Geophys Res Lett 36, L21704: doi:10.1029/2009GL040114.

Wang, B., Q. Bao, B. Hoskins, G. Wu, and Y. Liu (2008), Tibetan Plateau warming and precipitation changes in East Asia, Geophysical research letters, 35 (14), L14,702.

World_Bank, http://databank.worldbank.org/ddp. (2010).

Chapter 6

Conclusions

6.1 Summary

The observed climate change during the 20th century is, very likely, due to human activities and the emerging impact of anthropogenic climate change on ecosystems and human society has generated great concern. In addition to the increasing CO_2 concentration, human activities have caused other external forcing to the climate system, including land use change, emissions of aerosols (tiny solid or liquid particles suspended in the atmosphere), ozone, methane, etc. (Myhre and Shindell, 2013).

For near-term climate change projections at a regional level, a better understanding of BC aerosol impacts on the climate system is becoming particularly crucial because of the following two complexities: (1) the residence time of aerosols in the atmosphere is shorter than that of greenhouse gases. Thus, aerosol atmospheric loading is much more closely tied to the emission sources and therefore the economic activities and pollution control measures, which are not well predicted for the coming decades; (2) the geographical distribution of aerosols is largely determined by the source regions of industrial activities, unlike the globally well-mixed greenhouse gases. Vertically, the aerosol effect is mostly concentrated in the boundary layer or on the land surface (e.g., snow pack and glacier melting due to enhanced sunlight absorption and heating induced by black carbon and other light-absorbing impurities).

Carbonaceous aerosols, including black carbon (BC) and organic carbon (OC),

are significant contributors to anthropogenic climate change. BC is considered as the second only largest warming agent after CO_2. However, the direct radiative forcing of carbonaceous aerosols is still quite uncertain, in particular over the Asia region.

To better quantify the present-day Asian carbonaceous aerosol forcing, in Chapter 2 we utilized both a top-down approach that is constrained by ground-based and satellite observations over the first decade of the 21st century, as well as a bottom-up approach that is based on a latest global climate model coupled with an interactive chemistry and aerosol module (CESM1/CAM5/MAM3). (1) By making the comparisons of top-down observational estimates with bottom-up model simulations, we found that the model underestimates atmospheric heating of BC by factors ranging from 2 to 3. The major source of discrepancy between observations and models is shown by our studies to be the published emission inventory, which is developed using limited economic activity data provided by developing countries. A series of sensitivity tests of model simulations are conducted, in which BC anthropogenic emissions are increased by different factors. These tests suggested that BC emission sources are underestimated by a factor of two to four over Asia. (2) By applying a new partitioning scheme to the observed aerosol optical properties, we show that the brown carbon in OC can contribute up to 20% of atmospheric heating by BC. Thus, the overall TOA cooling of OC has been overestimated by earlier studies due to the neglect of brown carbon. The biases of OC forcing, simulated by the model, can be attributed to the adoption of refractive indexes estimated from laboratory measurements, rather than from ambient environment observations. In particular, the model currently does not account for brown carbon absorption, leading to a factor-of-two underestimation of its atmospheric heating and

consequently an overestimation of TOA cooling. The adjustment of the OC refractive index to match the empirically derived single scattering albedo improved the observation-model agreement.

In Chapter 3, we studied the large-scale pattern of temperature change in the last century, with the objective to better understand the relationship between external forcing and generated climate response. The focus of this study is the south-to-north warming asymmetry and a similar Latitudinal Asymmetry of Temperature Change (LATC) for the two warming sub-periods and the cooling sub-period. We hypothesized that the LATC is a fundamental characteristic of the planet's transient response to global forcing. We tested this hypothesis using climate model simulations of CO_2 and aerosol forcing, and the simulations revealed very similar LATC as seen in the observations. In the simulations, the LATC did not depend on the asymmetry of the forcing and furthermore weakened significantly in equilibrium simulations, leading to the deduction that the LATC was caused by a corresponding asymmetry in the land-ocean fraction, i.e., the analyses of model simulations supported the hypothesis of LATC being a fundamental characteristic of the planet's transient response.

In order to quantitatively assess the role of BC in climate system, in Chapter 4, we showed with the improved CESM that BC aerosols emitted from both sides of the Himalayan Mountains play a vital role in causing the observed snow cover reduction. The surface warming at high elevation (around 1 to 1.5 °C at 5000 m) associated with the direct heating effect of BC and the BC deposition on the snow surface are both important physical processes in causing the snow reduction. In our idealized simulations that mimic the contribution from the pre-industrial to present-day increase in BC emissions, the

yearly averaged snow cover area over Tibet is reduced by more than 2% and the snow depth is reduced by at least 5% (0.2 cm). Surprisingly, compared to the response to BC, the reduction of Tibet snow in response to pre-industrial to present-day increase CO_2 concentration is only 1.5 times larger for snow cover fraction and only 60% for snow depth, despite that the global mean temperature response is 5 times larger. Because of snow reduction, the surface albedo under all-sky conditions decreases by more than 5% along the Himalaya mountain range and nearly 1% over entire Tibet, therefore providing a positive local feedback mechanism to the warming. The effect on the hydrological cycle is the shifts of the river runoff to the beginning of the year, due to the largest reduction of snow observed during springtime.

Since the climate impact of BC over Tibet is significant and the Asia region is also currently the largest emitter of BC aerosols, in Chapter 5, we discussed the benefits of cutting BC pollutants from Asia regions. We used a comprehensive global climate model to evaluate the climate mitigation benefits associated with a rapid reduction of BC aerosols. The regional temperature and snow cover over Tibet is shown to be very sensitive to BC emission control measures. We show that the aggressive BC reduction leads to a significant amount of avoided warming and recovery of snow loss due to ongoing global warming. We further discussed the major sources of BC emissions from China and the potential practical measures to cut BC emissions. As an example, the costs of a specific mitigation measure, cook stove improvement, is calculated and compared against the valuation of climate change mitigations benefits, which are in terms of (1) the delaying of global mean warming and (2) the reduced mortality of local population.

6.2 Future research avenues

My previous research and many other GCM studies indicate that short-lived pollutants can be a dominant factor for climate forcing over specific regions and, therefore, the evolution of aerosol forcing may have played and will continue to play a substantial role in the decadal climate change. Previously, we mainly focused on the equilibrium response of the climate system to a particular type of aerosol (black carbon). In the future, we plan to expand the research scope by using coupled chemistry and climate model simulations to understand the transient climate response driven by multiple sets of aerosols and gaseous pollutants.

6.2.1 To identify the regions and climate phenomena where near-term climate change is most sensitive to various short-lived emissions

A better prediction of near-term climate change requires a better understanding of which part of the climate system is more likely to be influenced by short-lived species. Thus, the question of how short-lived species affect climate change can be converted into the question of climate predictability. The predictability associated with long-lived greenhouse gases is strong at large spatial scale (e.g., zonal average). As a strong regional forcing agent, aerosols could potentially provide additional decadal climate predictability and the aerosol driven circulation change could have a profound effect over particular regions. The main goal of Task 1 is to identify such geographical regions and climate phenomena for which a better predictability can be expected.

(1.a) In terms of geographical locations, the predictability of the South Asia monsoon system, in response to aerosol forcing, has been extensively documented (e.g.

Ganguly et al., 2012). We can build upon previous work in South Asia and expand it into other regions, such as the Southwestern US, Sahara desert, South America regions, etc. We are just beginning to understand the climate impacts in various regions. The open questions may include: Are the massive biomass burning aerosols, with both natural and anthropogenic sources from the Amazon and Southern Africa regions, important for the South Atlantic climate? Are the dust plumes transported from the Sahara desert, because of the land cover change, playing a role in shaping regional climate variability?

For such a purpose, we can diagnose GCM output from various future Representative Concentration Pathway (RCP) scenario runs (2015-2050), including single forcing experiments of CMIP5 (greenhouse-gases only, aerosol only, volcanic eruption only, etc.). Since the response signal due to aerosol forcing is smaller than that due to greenhouse gases, at least at global scale, we can conduct a large ensemble (>50) of model simulations and apply advanced statistical approaches, such as pattern recognition and machine learning.

(1.b) In terms of climate phenomenon, the aerosol effects have recently been connected to sea surface temperature pattern, cloud types and amounts, extreme precipitation and tropical cyclones. In addition, to better understand these effects, we can expand the analysis into other climate phenomena including stratospheric temperature, ocean intermediate water heat content and soil moisture. It is possible that these climate variables that have received less attention might contain fingerprints of short-lived pollutants and also serve as linkages in determining the overall response of the global hydrological cycle.

Fortunately, multiple-sensor satellites (A-train constellation measurement for

aerosols, clouds, precipitation and radiation fluxes) and float measurements of seawater properties (ARGO observations for ocean heat content and salinity), over the last decade, have provided unprecedented information (Reid et al., 2011) to conduct such detection studies. A careful retrospective look at the observational datasets can provide empirical evidence of the role of short-lived pollutants in the observed climate change at regional level. Long-term measurements provided by the DOE Atmospheric Radiation Measurement (ARM) facilities can be used to add confidence to the information provided in satellite retrievals, and provide additional information useful in interpreting the observational estimates of surface fluxes and ocean heat content.

(1.c) After using the hybrid approach of GCM simulation and observation diagnosis (1.a and 1.b), we will identify the climate phenomena and climate regions for which maximal predictability is expected. We will take a further step, with theoretical approaches, to identify the governing principle in determining the predictability. We will build on my previous simple modeling to develop a simple conceptual framework and then use it to provide fundamental insights into the question of how the regional forcing, due to anthropogenic pollutants, is distributed into the climate system and how the generated climate response interacts with the natural variability. Existing hypotheses, such as the role of the ocean circulation and tropical tropospheric temperature adjustment in regulating the overall climate response pattern, can also be examined with carefully designed GCM experiments and/or observational data diagnostics.

6.2.2 To identify the sensitivity of near-term climate predictions to two factors: physical treatment in GCM and future emission scenarios

After identifying the geographical locations and climate phenomena in which strong predictability can be expected in Task 1 (e.g., drought in the Southwestern US), the GCM-based climate prediction is still limited by at least two factors: physical treatment of short-lived pollutants in the model and the future emission scenarios.

(2.a) We can work with the model development team to conduct a large ensemble of experiments with perturbed physics, in which the model parameterizations (e.g., cloud microphysics, convection, aerosol optics and ocean diffusion schemes) will be modified and the model output sensitivity to such perturbations will be examined using the uncertainty quantification (UQ) techniques (e.g., Yang et al., 2013; Zhao et al., 2013). The sensitivity of specific climate phenomena, in specific regions to the selected-parameters and different parameterization schemes, can provide guidance for future model development efforts.

(2.b) Aerosol emission uncertainty is another limiting factor in the near-term climate prediction. Aerosol emissions are expected to decline sharply in the next few decades, in contrast to the increasing trend during the last few decades. The projections of future aerosols in the various Representative Concentration Pathways (RCP; Moss et al., 2010) adopted by the Intergovernmental Panel on Climate Change (IPCC), for its Fifth Assessment, differ and may not fully capture the possible emission pathways. Whether the model response to such an emission range exceeds the inherent model uncertainty due to physical parameterization (2.a) (and if yes, at what time and in which regions) remains

to be determined by conducting model experiments.

The next generation of RCP scenarios will include a much more complicated scenario "matrix" from multiple integrated assessment modeling groups and multiple mitigation policies, which could create too great a burden for modeling centers to conduct simulations under all scenarios. To deal with this challenge, we will also test whether the model response scales linearly with the assumed emission inventories used in the simulation and provide insights to the model simulation design. To assess the impact of regional emission uncertainties and future change, we will use the source region/sector tagging technique implemented to the CESM model (Wang et al., 2013), which can provide global aerosol source-receptor relationships for any specified emission scenarios.

6.2.3 To investigate the role of SLCPs in climate-chemistry interaction

In addition to being climate change forcers, short-lived species are also a major source of air pollution (Shindell et al., 2012), thus having a negative impact on public health and agriculture. Multi-decadal climate model simulation, with an online chemistry module, will be utilized with particular focus on the methane life cycle and tropospheric ozone formation.

We will first use satellite constellation measurement of aerosols and gaseous pollutants, since the year 2000, as a benchmark to evaluate model performance of simulating major pollutants. We have carried out similar studies for carbonaceous aerosols over California and concluded that the emission factor in the model needs to be adjusted for a better model-observation agreement (Xu et al., 2013b). More advanced techniques, which assimilate observations with model simulation, will be applied in the proposed study. With such an assimilation data product, we will then quantify the

abundance of air pollutants under various mitigation policies. It is also of great interest to understand how the future change of extreme weather events (heat waves, high pressure systems, etc.), as a consequence of short-lived species studied in Task 1, will affect the transport and distribution of the PM2.5 pollutions. We will calculate the frequency of occurrences of such extreme pollution events using high-resolution models and co-locate those events with population exposure to quantify human health impact.

6.3 Significance of future research

The future research directions discussed in section 6.2 is driven by the goal of understanding climate variability and change. The study on the aerosol's role in the climate system will improve future climate projections and, particularly, it will allow more accurate projections of temperature and precipitation fields, which will certainly help to enhance society's ability to plan and respond to climate change.

Moreover, through the study of the climate system response to the perturbation of aerosols, we can gain fundamental insights into how the coupled ocean-atmosphere climate system works and provide suggestions as to what future modeling and observational capacity (ground networks and operational satellites) are needed.

In summary, the work on linking climate change to air quality research is transformative and will deepen our understanding of the entire earth system. Success of the proposed project will enable a research team to act as a significant player in the emerging field of improving near-term climate predictions, which are projected as major research areas of climate science in the next decade. The outcome of this research will provide interdisciplinary engineers and scientists with the sophisticated tools necessary to

make reliable regional and global decadal climate projections, with reduced uncertainty that is useful for policy and decision-making.

References

Bahadur, R., P. S. Praveen, Y. Xu, and V. Ramanathan (2012), Solar absorption by elemental and brown carbon determined from spectral observations, Proceedings of the National Academy of Sciences of the United States of America, 109(43), 17366–71, doi:10.1073/pnas.1205910109.

Ganguly D, PJ Rasch, H Wang, and JH Yoon. 2012. "Climate response of the South Asian monsoon system to anthropogenic aerosols." Journal of Geophysical Research. D. (Atmospheres) 117:Article No. D13209. doi:10.1029/2012JD017508

Hu, A., Y. Xu, C. Tebaldi, W. M. Washington, and V. Ramanathan (2013), Mitigation of short-lived climate pollutants slows sea-level rise, Nature Climate Change, 3(5), 1–5, doi:10.1038/nclimate1869.

Moss, R. H. et al. (2010), The next generation of scenarios for climate change research and assessment., Nature, 463(7282), 747–56, doi:10.1038/nature08823.

Myhre and Shindell (2013), Chapter 8: Anthropogenic and Natural Radiative Forcing. WORKING GROUP I CONTRIBUTION TO THE IPCC FIFTH ASSESSMENT REPORT CLIMATE CHANGE 2013: THE PHYSICAL SCIENCE BASIS.

Ramanathan, V., and Y. Xu (2010), The Copenhagen Accord for limiting global warming: criteria, constraints, and available avenues, Proceedings of the National Academy of Sciences of the United States of America, 107(18), 8055–62, doi:10.1073/pnas.1002293107.

Reid, J. S., A. Benedetti, P. R. Colarco, and J. A. Hansen (2011), International Operational Aerosol Observability Workshop, Bull. Am. Meteorol. Soc., 92(6), ES21–ES24, doi:10.1175/2010BAMS3183.1.

Shindell, D. et al. (2012), Simultaneously mitigating near-term climate change and improving human health and food security., Science, 335(6065), 183–9, doi:10.1126/science.1210026.

Wang, H., and co-authors, 2013: CAM5/CESM estimates of global source-receptor relationships for black carbon under present-day emission scenario. To be submitted.

Xu, Y., D. Zaelke, G. J. M. Velders, and V. Ramanathan (2013a), The role of HFCs in mitigating 21st century climate change, Atmospheric Chemistry and Physics, 13(12), 6083–6089, doi:10.5194/acp-13-6083-2013.

Xu, Y., R. Bahadur, C. Zhao, and L. Ruby Leung (2013b), Estimating the radiative

forcing of carbonaceous aerosols over California based on satellite and ground observations, Journal of Geophysical Research: Atmospheres, 2013JD020654, doi:10.1002/jgrd.50835.

Xu, Y., W. M. Washington, and V. Ramanathan, Climate effects of black carbon over East Asia. In preparation.

Yang B, Y Qian, G Lin, LR Leung, PJ Rasch, GJ Zhang, SA McFarlane, C Zhao, Y Zhang, H Wang, M Wang, and X Liu, 2013: Uncertainty quantification and parameter tuning in the CAM5 Zhang-McFarlane convection scheme and impact of improved convection on the global circulation and climate, J. Geophys. Res. Atmos., 118, 395–415, doi:10.1029/2012JD018213.

Zhao, C., Liu, X., Qian, Y., Yoon, J., Hou, Z., Lin, G., McFarlane, S., Wang, H., Yang, B., Ma, P.-L., Yan, H., and Bao, J. (2013), A sensitivity study of radiative fluxes at the top of atmosphere to cloud-microphysics and aerosol parameters in the Community Atmosphere Model CAM5, Atmos. Chem. Phys., 13, 10969-10987, doi:10.5194/acp-13-10969-2013.